Building a Combined Brightfield and Confocal Quantum Diamond Microscope for Imaging of Magnetic Samples

Olve Sti

Master Thesis in Nano Science

Supervisors: Associate Professor Dr. Martin Greve
Dr. Justas Zalieckas

Department of Chemistry
University of Bergen, Norway

August 1, 2021

Year: 2021
Title: Building a Combined Brightfield and Confocal Quantum Diamond Microscope for Imaging of Magnetic Samples
Author: Olve Sti

Acknowledgements

I would like to thank my supervisors Associate Professor Martin Møller Greve and Dr. Justas Zalieckas for showing me this project and giving me support and feedback through this entire Master Thesis. They have been invaluable in helping me understand the theory of the QDM and how to optimize the QDM. I would like to thank my friends and my family for supporting me through this Master Thesis and showing interest throughout. Lastly, I would like to thank the nanophysics group for their support and insight in this project.

Abstract

The imaging of weak magnetic fields has been an important area of both research and technology. It continues to be an area that requires further research due to its potential wealth of applications. One magnetic field imaging technique that has risen in popularity these last few years is called a Quantum Diamond Microscope (QDM). The QDM uses the fluorescence from negatively charged Nitrogen Vacancy defect centers (NV) in diamond to image magnetic fields due to their usability at room temperature and pressure and high sensitivity to magnetic fields. NV^-s are fluoresced with a low-power $\sim$ 594 nm laser, the NV^-s can also change into a dark, non-fluorescing, state, where they can remain on a timescale of several seconds. The change of state can be exploited to switch the fluorescence of NV^-s off, in a stochastic manner, and it will look as if they are blinking. Combining the NV^-s' blinking together with their sensitivity to magnetic fields allow them to be used as sensors capable of imaging magnetic fields with super resolution. The objective of this Master Thesis is to build a microscope capable of performing Optically Detected Magnetic Resonance (ODMR) on NV^- centers. Furthermore, the microscope will be used to carry out Stochastic Optical Reconstruction Microscopy (STORM) to obtain super resolution by exploiting the switching of NV^- to its dark state. The final goal is to combine the two and attempt to do super resolution magnetic field imaging.

The main part of this thesis work involve the building of a combined bright-field and confocal microscope. To carry out STORM, a very sensitive photodetector must be implemented. For this purpose, both a Photomultiplier Tube (PMT) and a Si amplified photodetector was tested. Furthermore, the confocal pinhole must be optimized and aligned and a XYZ-piezo stage was installed for doing Confocal Laser Scanning Microscopy (CLSM). A LabVIEW program was developed to perform CLSM, and other programs in both LabVIEW and MATLAB were modified and implemented for the setup. For the confocal imaging, the focused laser spot on the sample was calculated to be 1460 ± 30 nm and the number of NV^-s in the focused volumes of the two diamond samples used in this work were estimated to be 2400 NV^-s and 12 NV^-s. Confocal imaging has been demonstrated and the $\boldsymbol{B}$ field has been measured for 6 different ODMR measurements. Unfortunately it was not possible to demonstrate the blinking of NV^-s and further carry out STORM. It was found the PMT and Si amplified photodetector used had too much inherent noise to observe the NV^- blinking. It is suggested that a more sensitive detector like a photon counter detector is necessary to observe this.

Contents

Acknowledgements iii

Abstract v

1 Introduction 1
- 1.1 Background . . . 1
- 1.2 Quantum diamond microscope . . . 2
  - 1.2.1 Optically detected magnetic resonance . . . 2
  - 1.2.2 Nitrogen vacancy defect centers . . . 2
  - 1.2.3 State of the art of NV ODMR . . . 3
- 1.3 Sub-diffraction-limited optical imaging with fluorescence . . . 3
- 1.4 Thesis Objective and Workflow . . . 4
- 1.5 Thesis Outline . . . 5

2 Theory 7
- 2.1 The nitrogen vacancy defect center in diamond . . . 7
  - 2.1.1 Nitrogen vacancy structure . . . 8
  - 2.1.2 Nitrogen vacancy density . . . 9
  - 2.1.3 Nitrogen vacancy electronic structure . . . 10
  - 2.1.4 The ground state Hamiltonian of NVs . . . 11
  - 2.1.5 Nitrogen Vacancy blinking . . . 12
  - 2.1.6 Stochastic optical reconstruction microscopy . . . 14
- 2.2 Microscopy . . . 15
  - 2.2.1 Diffraction and resolution . . . 15
  - 2.2.2 Confocal imaging . . . 16
  - 2.2.3 Fluorescence . . . 17
- 2.3 Optics . . . 17
  - 2.3.1 Lens theory . . . 18
- 2.4 Instrumental background . . . 19
  - 2.4.1 Camera . . . 19
  - 2.4.2 Photomultiplier tube . . . 19
  - 2.4.3 Laser . . . 20
  - 2.4.4 The laser spot . . . 21
  - 2.4.5 Pinhole image . . . 22
- 2.5 Statistics . . . 23
  - 2.5.1 Standard deviation . . . 23
  - 2.5.2 Other statistics equations . . . 24

3 Experimental setup **25**
3.1 Diamonds . . . 25
3.1.1 Fluorescent samples . . . 26
3.2 Microscope setup . . . 27
3.2.1 Imaging and sensing . . . 30
3.2.2 Laser . . . 32
3.2.3 Mirrors . . . 32
3.2.4 Lenses . . . 32
3.2.5 Optical filters . . . 33
3.2.6 Pinhole . . . 34
3.2.7 Piezo stages . . . 34
3.2.8 Optically detected magnetic resonance setup . . . 35

4 Description of protocols **37**
4.1 MATLAB . . . 37
4.1.1 Laser spot script . . . 37
4.2 LabVIEW . . . 38
4.2.1 Single input program . . . 38
4.2.2 Confocal imaging program . . . 39
4.3 Smaller scripts and programs . . . 41
4.3.1 FWHM and $1/e^2$-width script . . . 41
4.3.2 Double input . . . 41
4.3.3 Camera code . . . 42

5 Experimental results **43**
5.1 Camera image size . . . 43
5.2 Laser spot size and NVs in spot . . . 44
5.3 Detecting NV fluorescence and blinking . . . 48
5.3.1 Camera . . . 48
5.3.2 Photomultiplier tube . . . 48
5.3.3 Si amplified photodetector . . . 49
5.4 Confocal imaging . . . 54
5.5 Optically detected magnetic resonance of NVs . . . 56

6 Discussion of results **57**
6.1 Diamond samples . . . 57
6.2 Analysis of camera . . . 58
6.2.1 The Gaussian fit . . . 58
6.2.2 Camera code . . . 58
6.3 Analysis of the photodetectors . . . 59
6.4 Additional challenges for observing NV blinking . . . 60
6.5 Confocal imaging discussion . . . 61
6.6 Analysis of the ODMR measurements . . . 62

7 Conclusion **63**
7.1 Conclusion . . . 63
7.2 Further work . . . 63

A MATLAB script **65**

B LabVIEW programs **71**
B.1 Single input panels 72
B.2 Confocal imaging panels 74

Bibliography **77**

List of Figures

2.1 Nitrogen vacancy unit cell. . . . 8
2.2 The four possible orientations an NV can have . . . 8
2.3 NV^- states and transitions. . . . 9
2.4 The emission spectrum of NV^- and NV^0 . . . 9
2.5 The photon and radiant flux of an NV from a 532 nm laser . . . 13
2.6 Simulated Airy Disk with its Airy Unit drawn in . . . 16
2.7 Light through a thin lens, with image being half of object size. . . . 19
2.8 The standard Gaussian distribution. . . . 21
2.9 Illustrated width of a beam at 4σ width. . . . 21

3.1 The structure of Rhodamine 640 Perchlorate. . . . 26
3.2 The fluorescence spectrum of Rhodamine 640 Perchlorate. . . . 26
3.3 A schematic of the setup used in this Master Thesis. . . . 28
3.4 Setup shown from the side. . . . 28
3.5 Setup from the sample side. . . . 29
3.6 Setup inside box shown from above. . . . 29

4.1 Block diagram of the script, ”Laser Spot Script”, for calculating the size of the spot from an image. . . . 38
4.2 Block diagram for ”Single Input”, the program for continuously measuring samples from the detector using LabVIEW. . . . 39
4.3 Block diagram of the ”Confocal Imaging” program. . . . 40

5.1 Camera image of the microscope micrometer. . . . 44
5.2 A camera image of the spot with the dim sample with aluminium coating. . . . 45
5.3 A heat image of the spot. . . . 45
5.4 Image of the spot from the Laser Spot Script. . . . 46
5.5 A 3D surface image of the spot and the Gaussian fit. . . . 47
5.6 16-bit camera code of NVs with the first 40 measurements. . . . 48
5.7 Background camera measurement without the first 40 measurements. . . . 48
5.8 Measurement of the background noise from the PMT at night with the lights off. . . . 49
5.9 Measurement of the background noise from the Si photodetector, where the Y-axis is in mV and the X-axis is in seconds. . . . 50
5.10 Two voltage measurements from the bright sample with the Si photodetector. 51
5.11 Two voltage measurements from the dim sample with the Si photodetector. . 51

5.12 Two voltage measurements from the dim sample with the aluminium coating with the Si photodetector. . . . 51
5.13 Two voltage measurements from the dim sample with the silver coating with 2 s on-time with the Si photodetector. . . . 52
5.14 Confocal heat and surface images of a 2.5x2.5 μm^2 area on the nanodiamond sample. . . . 54
5.15 Confocal heat and surf images of a 1x1 μm^2 area on the nanodiamond sample. 54
5.16 Confocal heat and surface images of a 5x5 μm^2 area of the Rhodamine sample. 55
5.17 Reverse Confocal heat and surface images of a 5x5 μm^2 area of the Rhodamine sample. . . . 55
5.18 6 measurements of our ODMR setup with different $\boldsymbol{B}$ field strength. . . . 56

6.1 A 3D surface image of the bright spot together with the Gaussian fit. . . . 58
6.2 A 3D surface image of the dim spot without the coating together with the Gaussian fit. . . . 58

B.1 The front panel of the Single Input LabVIEW code. . . . 72
B.2 The back panel of the Single Input LabVIEW code. . . . 73
B.3 The front panel of the Confocal Imaging LabVIEW code. . . . 74
B.4 The back panel of the Confocal Imaging LabVIEW code. . . . 75

List of Tables

2.1 C_{3v} point group table with the reducible representation for NV centers, Γ_{NV}. . 10

3.1 The properties of the two single crystal diamonds. 26
3.2 Short explanation of the microscope equipment. 27
3.3 The properties of the XIMEA camera. 30
3.4 The calculated lowest detectable power of the photodetectors 32

5.1 Four calculated spot sizes. 45
5.2 Spot size comparisons between beam expansion methods. 47
5.3 Voltage mean, SD and variance of the Si photodetector measurements. . . . 52
5.4 Resonant frequencies and calculated $\boldsymbol{B}$ field from 6 ODMR measurements. . 56

Glossary

irrep irreducible representation. 10

AEG Auto Exposure and Gain. 42

AI Analog Input. 39, 40

AU Airy Unit. 17, 22, 23, 34

CLSM Confocal Laser Scanning Microscopy. v, 16

CMOS Complementary Metal Oxide Semiconductor. 4, 19, 27, 30

CVD Chemical Vapor Deposition. 7, 25

FOV Field of View. 43, 44, 57

FWHM Full-Width at Half Maximum. viii, 21, 22, 34, 37, 41

GMR Giant Magnetoresistance. 1

GSD Ground-State Depletion. 3

HDD Hard Disk Drive. 1

HPHT High-Pressure High-Temperature. 7

ISC Intersystem Crossing. 11

LCAO Linear Combination of Atomic Orbitals. 10

MFM Magnetic Force Microscopy. 1

MOKE Magneto-Optical Kerr Effect. 1

MRI Magnetic Resonance Imaging. 1

MW Microwave. 2, 3, 9–11, 14, 28, 35, 62

NA Numerical Aperture. 16, 22, 32–34

ND Neutral Density. 4, 25, 29, 34, 49–53, 60, 61

NEP Noise-Equivalent Power. 31

NI National Instruments. 30, 38, 39

NTP Normal Temperature and Pressure. 2, 3

NV Nitrogen Vacancy. v, vii, viii, 2–5, 7–14, 21, 25–27, 30, 32–34, 37, 43–57, 59–64

OD Optical Density. 34, 49–53, 60, 61

ODMR Optically Detected Magnetic Resonance. v, vii, viii, 2–4, 7, 11, 12, 14, 25, 35, 37, 53, 56, 62

PMSM Permanentmagnet Synchronousmotor. 1

PMT Photomultiplier Tube. v, 4, 7, 19, 20, 25, 30–33, 43, 48, 49, 57, 59, 60, 63

QDM Quantum Diamond Microscope. v, 2–5, 63

RMS Root Mean Square. 24, 31, 39, 49, 59

SD Standard Deviation. 7, 22–24, 30–32, 37–39, 46, 52, 53

SE Stimulated Emission. 3

SQUID Superconducting Quantum Interference Device. 1

SSD Solid State Drive. 1

STED Stimulated Emission Depletion. 3

STORM Stochastic Optical Reconstruction Microscopy. v, 2, 4, 5, 7, 14, 25, 46, 53, 63

VI Virtual Instrument. 38, 71

ZPL Zero Phonon Line. 8–11

Chapter 1

Introduction

1.1 Background

Research on magnetic fields and their applications has paved the way for today's technology; Hard Disk Drives (HDD) use magnetic sectors as 1s and 0s to store information [1] and have been invaluable for technological progress [2], even as newer forms of information storage, like Solid State Drives (SSD) are designed. Electrical motors, like the Permanent-magnet Synchronousmotor (PMSM) have furthered the research on electric vehicles [3] that are being used today, and there is research being done on electric aircrafts [4] as a result of this. Magnetic Resonance Imaging (MRI) , is being used to map the blood oxygenation in the brain [5] and has been an important part of research on the brain within the medical field. The discovery of Giant Magnetoresistance (GMR), a material's resistivity was decreased due to a magnetic field [6], in 1988 paved way for new research within magnetic fields, like spintronics [7]. Spintronics is a field of technology where the spin of the electron carries the information, and not the charge. The discovery of GMR showed its importance by being awarded the Nobel Price in Physics in 2007.

The research and implementation of magnetic imaging have been able to advance several areas of research and remain an important field of science. Imaging of weak magnetic fields at the nanoscale is an important area of research due to its potential wealth of applications in science and technology [8]. Several prominent techniques are available for imaging magnetic fields; Magnetic Force Microscopy (MFM), Superconducting Quantum Interference Device (SQUID) microscopy and Magneto-Optical Kerr Effect (MOKE) imaging [9]. MFMs are widely used due to their extremely high spatial resolution for imaging, but they suffer from a small field of view, < 100 µm , limited resolution of the magnetic field, > 10 µT, and the fact that they provide the absolute value of the field [10]. SQUID microscopes, on the other hand, have excellent magnetic field resolution, > 500 fT$/\sqrt{\text{Hz}}$, but the spatial resolution in room temperature is quite poor, > 150 µm [11]. MOKE imaging is not suitable for reconstructing the magnetic vector field reliably [12].

1.2 Quantum diamond microscope

1.2.1 Optically detected magnetic resonance

Recently, another method of imaging weak magnetic fields has gained popularity in usage called Quantum Diamond Microscopy (QDM) [9]. The QDM takes advantage of the properties of Nitrogen Vacancies NV in diamond to detect magnetic fields. An NV refers to a part of the structure in a diamond lattice, where a carbon atom has been substituted with a nitrogen atom and one of the neighboring carbon atoms has been replaced with a vacancy. A QDM uses a negatively charged nitrogen atom in its NVs, written as a NV^-, as this gives the NVs fluorescent properties that is highly sensitive to strain and thermal, electronical, and magnetical changes. Unless specified otherwise, the NV^- is the defect center referred to when using simply ”NV” for the rest of this Master Thesis.

Due to this sensitivity to magnetical changes, the QDM can perform Optically Detected Magnetic Resonance (ODMR) on the NVs to image magnetic fields. NVs will be explained more in-depth in Subsection 1.2.2 and Chapter 2. Optically detected implies that the magnetic resonance is detected optically by the light emitted from the fluorescence of the NV. Magnetic resonance refers to a a phenomenon where magnetism causes an excitation, or a resonance, in the sample [13]. This resonance can cause a change in the fluorescence of the NV. Thus, using ODMR, the magnetic field of the sample can be imaged.

ODMR for NVs is performed using radiation of Microwaves (MW). Radiating NVs with a MW resonant to the magnetic field on the NV, causes a decrease in fluorescence intensity. While performing ODMR with the QDM, there is an interest in obtaining sub-diffraction limited resolution with the magnetic field imaging. This can be done through combined ODMR with Stochastic Optical Reconstruction Microscopy (STORM), which will be explained in Section 1.3.

1.2.2 Nitrogen vacancy defect centers

At the ground level, NVs have three states important for their magnetic imaging properties. These states will be referred to as ”0”, ”+1” and ”-1”, where the latter two can be considered degenerate at Normal Temperature and Pressure (NTP). NTP means a temperature of 20 °C and a pressure of 1 atm. Radiating the NVs with MWs of a characteristic frequency, the NVs can go from the 0 state to the ± 1 states. The fluorescence is of a different wavelength when the NVs are in the ± 1 states, and can therefore be filtered away, causing the fluorescence intensity measured to decrease. The NVs' sensitivity to magnetic fields comes from the fact that the ± 1 states will split in proximity to a magnetic field. The MW frequencies will therefore also split. The distance between the two MW frequencies is proportional to the magnetic field. This is how NVs can be used to image magnetic fields.

1.2.3 State of the art of NV ODMR

QDM has risen in popularity in the last few years as a technique for mapping out weak magnetic fields [9]. One of the simplest ways of measuring magnetic fields with a QDM is by doing broadband imaging. Broadband imaging uses a wide range of the MWs for the ODMR. It goes through these frequencies, radiating the sample, from the lowest to the highest frequency with a given spacing. This enables broadband imaging to investigate several values of the magnetic field strength at once, imaging the entire magnetic field from the sample. Narrowband imaging, on the other hand, only uses a single frequency of the microwave to radiate the sample and is therefore not as important as broadband imaging for QDMs.

This paragraph will list some of the important results that have come from QDM broadband imaging. Using a QDM, the magnetic field from a small wire has been imaged. From these measurements, they measured the projection of the magnetic field along the four crystallographic directions, and from there reconstructed the magnetic field and obtained the vectorial representation of the field [14]. The QDM's magnetic field imaging has been taken advantage of to reconstruct the current density distribution. This revealed the current flow features of sub-µm defects in graphene, and supports that this technique can be used for other 2D materials as well [15]. The QDM can also be used on living cells, due to it working under NTP. It has been used to reconstruct images of the vector component of the magnetic field generated from chains of magnetic nanoparticles produced in the bacteria MTB. Supporting that QDMs can be used to map magnetic signals within cells and cellular networks [16].

The results explained in these papers, and the results obtained by imaging with QDMs, support the importance of research on QDMs and imaging of magnetic fields. Many of the current QDMs are resolution limited optically due to diffraction. We hope to further both research and technology by designing a QDM with high spatial resolution optically.

1.3 Sub-diffraction-limited optical imaging with fluorescence

By itself, the spatial resolution of the bright-field imaging of the QDM is limited by diffraction, on par with an optical microscope. Optical bright-field imaging is the simplest microscopy technique where the sample is illuminated, and the light transmitted through the sample is used to create an image of the sample.

Obtaining sub-diffraction limited resolution, or "super-resolution", in narrow-field, or confocal, imaging has been something researchers have accomplished and been improving for years. Imaging through fluorescence, like for example Stimulated Emission Depletion (STED), capable of resolving 35 nm in the far-field, [17], and Ground-State Depletion (GSD) [18], capable of resolving 15 nm in far-field, has been an important part of this research and has helped push optical imaging below the diffraction limit. Both approaches achieve super-resolution by limiting the spatial area within the laser focus. STED does this by using Stimulated Emission (SE) to reduce the fluorescence in the outer areas of the focus. Meanwhile GSD achieves this by depleting the ground state emission of the molecules on the edge of the focus.

Another fluorescent optical imaging technique that can provide super-resolution and has led to a wealth of applications is called Stochastic Optical Reconstruction Microscopy (STORM) [19]. STORM takes advantage of the stochastic properties of fluorescence to obtain sub-diffraction resolution in confocal imaging. For a given fluorophore, STORM functions like this: The stochasticity of fluorescence ensures that only some of the fluorophores will fluoresce at the same time. A camera will then image these fluorophores and for each image, the optically resolvable fluorophores will be pin-pointed and saved. Optically resolvable means that the fluorescence from the fluorophore does not overlap with that of any other NV centers. By imaging the same area several times, new fluorophores will be pinpointed for each image and by repeating this process enough times, an image of the fluorophores can be recreated with spatial super-resolution [19].

The STORM technique can be implemented to other microscopes that image fluorescence. It has therefore been proposed that the STORM technique can be implemented in a QDM to obtain super-resolution for the magnetic field measurements from ODMR [20]. The approach to obtain STORM with a QDM wil be explained in detail in Section 2.1.6.

1.4 Thesis Objective and Workflow

The objective of this Master Thesis is to implement STORM in a QDM to obtain optical super-resolution imaging of NVs while performing ODMR. To accomplish this, we will first perform ODMR with a QDM to measure magnetic fields. This will be carried out using a bright field QDM setup with a Complementary Metal Oxide Semiconductor (CMOS) camera for imaging and signal detection. Then we will add another optical path for the microscope, implementing a more light sensitive detector, with also a higher readout speed compared to the camera. We will then try to accomplish STORM with this new optical path specifically optimized for STORM.

Lining up the optical path was the first step of this Master Thesis. After that, the camera was used to image the fluorescence from the NVs, and from this image minimize the laser spot on the surface of the diamond. Afterwards, the more light sensitive detector, the PMT, was added in a different light path, which could be swapped to using a flip-up mirror. A pinhole was added in front of the PMT, and the signal detected by the PMT was maximized using a lens in front and behind the pinhole. Lastly, for the microscope setup, an XYZ-piezo stage setup was added to the sample holder, and ND filters were added to reduce the laser power. Codes were also written or modified. The script used to calculate the laser spot size and the LabVIEW program for measuring the detector's output were modified for our setup. Lastly a code was written to perform confocal imaging using the XYZ-piezo stage setup.

1.5 Thesis Outline

Chapter 2 goes in-depth on the theoretical background behind the QDM by going through the physics of NVs to explain their sensitivity to magnetic fields and their ”blinking” property used for the STORM. Lastly, microscopy and the theory behind the microscope will be explained. Chapter 3 explains the experimental setup of the QDM, what parts, like the objective, the camera and laser, are used in the microscope and the justification to use them. Chapter 4 describes the protocols, data collection methods and how the data was analyzed. The software, programs and scripts used will be explained and motivated. Chapter 5 will go through the experimental results found and the calculations of the results. Chapter 6 discusses and analyses the results and the work done. Finally Chapter 7 gives the conclusion of this Master Thesis and suggestions for further work.

Chapter 2

Theory

This chapter presents the physics of the Nitrogen Vacancy (NV) in diamonds. The physical and energy structure of the NVs will be the focus and how to use NVs as a sensor. The chapter will therefore start by explaining the physics of NVs, where the structure of an NV in the diamond lattice together with its energy diagram will be used to explain how NVs can be used as a sensor for magnetic fields, using Optically Detected Magnetic Resonance (ODMR). In this section, Stochastic Optical Reconstruction Microscopy (STORM) together with ODMR with NVs will be explained through the physics of fluorescence and the NVs, enabling sub-diffraction limited imaging of the spin of the NVs. Microscopy will be briefly explained next, with focus on resolution and confocal imaging. The chapter will continue with going through some optical physics, specifically regarding lenses and fluorescence. Theory on Photomultiplier Tube (PMT) will be explained afterwards. Then the theory related to lasers, including how to calculate the size of a laser spot and physics regarding pinholes for the confocal setup, will be explained. The chapter will end by showing the equations for some simple statistics necessary for the instruments and coding: the Standard Deviation (SD) and variance.

2.1 The nitrogen vacancy defect center in diamond

The diamonds used in this project were all synthetic diamonds. Diamonds made in a laboratory with low levels of impurities, compared to natural diamonds made by geological processes [21, 22]. The main reason for using synthetic diamonds is to have customizable single crystals with low purity and low cost [22, 23]. For the purpose of NVs, especially the amount of nitrogen, or lack thereof, used in the manufacturing of the diamond is important. There are two different types of synthetic diamonds, divided into the process used to make them: High-Pressure High-Temperature (HPHT) [21] and Chemical Vapor Deposition (CVD) diamonds [24, 23]. The diamonds used in our project were all CVD diamonds. HPHT diamonds are formed by applying high pressure and high temperature to change the equilibrium between diamond and graphite so diamond is the most stable [23]. CVD diamonds are made by having the template for diamond as a substrate and then adding carbon onto the substrate to create a synthetic diamond.

2.1.1 Nitrogen vacancy structure

The atomic structure of the NV in diamond is shown in Figure 2.1. In simple terms, with the structure of diamond, replace one atom in its unit cell with a nitrogen atom. Then replace either of the four adjacent atoms with a vacancy [25]. For the diamond structure, the NVs only have four different orientations in the unit cell, as shown in Figure 2.2. The atoms that are a part of this center is then: The vacancy, its 3 adjacent carbon atom and the adjacent nitrogen atom. The 3 C atoms contribute with one electron to the NV center each while the N atom contributes with an electron pair [8].

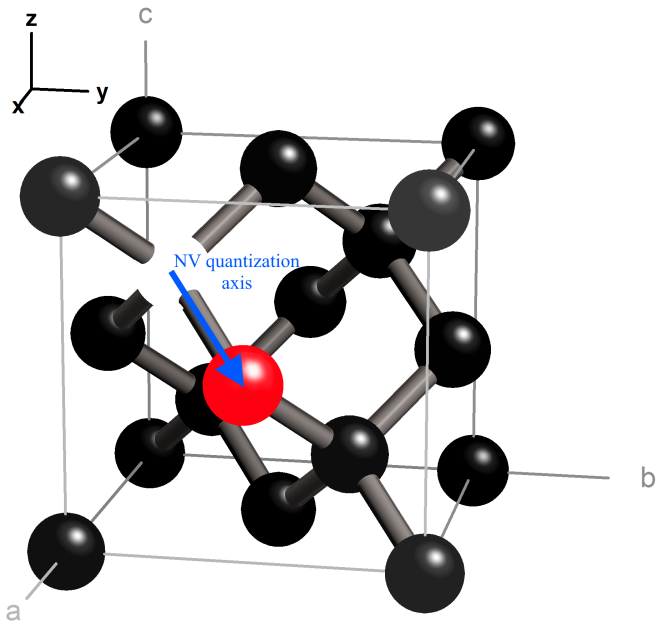

Figure 2.1: The diamond unit cell with an NV shown in the top left. Carbons are shown in black, the Nitrogen in red and the vacancy is shown as the missing carbon atom. The blue arrow shows the direction of the NV quantization axis, from the vacancy to the Nitrogen atom.

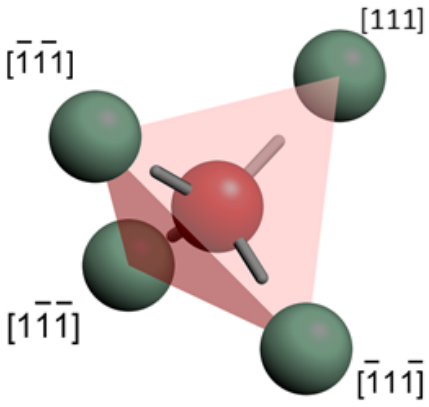

Figure 2.2: The four possible orientations an NV can have. This direction is equal to the NV quantization axis.

A neutral NV defect center will therefore have 5 electrons to place into orbitals, while a negatively charged NV will have 6 electrons. A neutral NV is referred to as an NV^0 and a negatively charged is referred to as an NV^-, or simply "NV" in this Master Thesis. Both of these NVs are fluorescent, but the fluorescence of the NV^0 has less intensity and is blue-shifted from the fluorescence of the NV^-, as shown in Figure 2.4 [26]. The Zero Phonon Line (ZPL) for these two defect centers is 575 nm and 637 nm for the NV^0 and the NV^- respectively. The ZPL is the wavelength where an excitation occurs without the assist of a phonon [27].

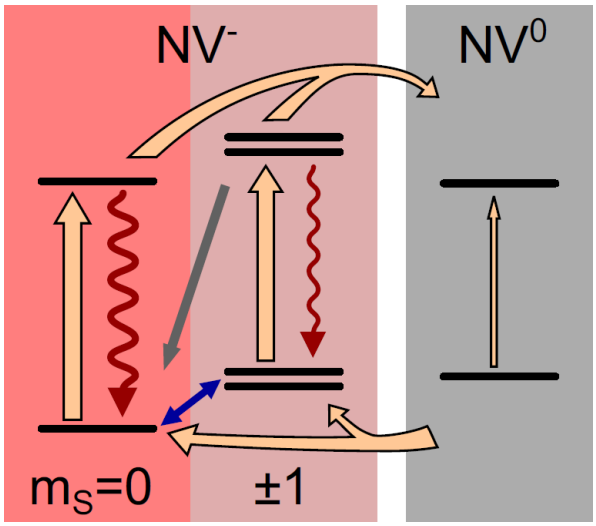

Figure 2.3: The different states the NV can switch between. Starting in m_s=0, it can be excited through MW radiation, shown with the blue arrow, to the $m_s = \pm 1$ state. From both of these states, the NV can be excited through light, shown in the yellow arrows. Both of these states decay back to their ground state by emitting light, shown by the red arrows. Finally the NV^- can be changed to the NV^0 when its electron gets excited into the conduction band. From the NV^0, light can again excite it back to the NV^- state. Figure taken from [20].

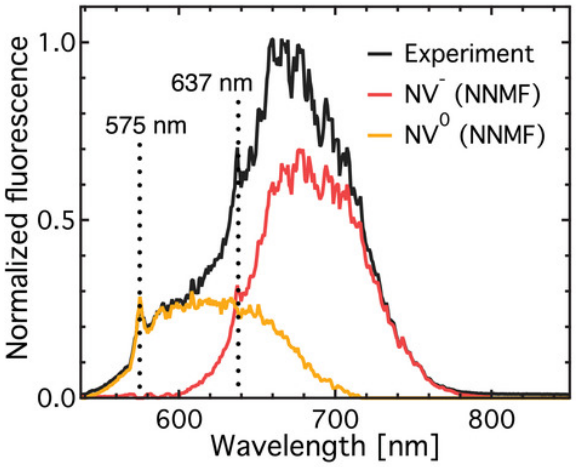

Figure 2.4: The emission spectrum of NV centers, with NV^- in red, NV^0 in orange and experimental measurement with both in black. The spectrum shows a clear ZPL at 575 nm for NV^0 and 637 nm for NV^-. Figure taken from [26].

2.1.2 Nitrogen vacancy density

To calculate the NV concentration per volume when the amount of Nitrogen used in the manufacturing is known, previous measurements are used as basis to make an Equation. The previous measurement is based off measurements and calculations done by A. M. Edmonds et al. [28]. They had a Nitrogen value of ≈ 0.1 ppb used in the CVD manufacturing of the diamond. From their own results, they estimated that 0.5% of the Nitrogen present during the manufacturing of the diamond became NVs [28]. The NV concentration of the diamond will therefore be $\leqslant (0.2 - 0.5) \cdot 10^{-3}$ ppb. From their results, this will then correspond to an average of $\leqslant 10 - 30$ NVs in a $10 \times 10 \times 4$ μm^3 volume. With these values a simple equation can be made to estimate the NVs in a volume:

$$\frac{N_{NV}}{V \cdot \text{ppb}} \approx \frac{30 \text{ NVs}}{400 \ \mu m^3 \cdot (5 \cdot 10^{-5}) \text{ppb}} = 150(\text{ NVs}/\mu m^3) \cdot \text{ppb}. \tag{2.1}$$

2.1.3 Nitrogen vacancy electronic structure

From Figure 2.1 of the NV defect center, the structure is not a linear structure. It has a C_3 rotational axis, but only one through the nitrogen and vacancy, and no other rotational axes. It has no horizontal mirror planes, but has three vertical mirror planes. This shows that the NV defect center in diamond has a C_{3v} point group [29, 30].

With the point group of the NV now known, Linear Combination of Atomic Orbitals (LCAO) can be performed to find the reducible representation of the NVs [31, 30]. A reducible representation is a matrix that can, in some way, be further reduced, or shortened. The reducible representation of the NV s is used to find the irreducible representation (*irrep*) of the system. The *irrep* is used in LCAO to find the energy order of the orbitals to the system.

To find the *irrep*, the symmetry operations for C_{3v} need to be found, which can be found in the C_{3v} character table shown in Table 2.1 [29]. From the character table, these operations can be found: E, the identity, $2C_{3v}$, the rotation along its main axis, and $3\sigma_v$, the mirror plane through the vertical axis [29]. To find out how much each of the operations contributes to the reducible representation, the number of bonds that are unmoved for each operation is found, shown in the final line of Table 2.1. From the reducible representation, the values next to the *irrep*s of the C_{3v} character table, A_1, A_2, E, shown in Table 2.1, need to be used to find the *irrep* of the NVs. From Table 2.1, showing the NV's reducible representation, their *irrep* becomes: $\Gamma_{NV} = 2A_1 + 2E$. This is because of the values to the right of A_1 and E from Table 2.1: $[1,\ 1,\ 1]$ and $[2,\ -1,\ 0]$ respectively. If 2 of A_1 and 2 of E are summed up by column: 1st: $2 \cdot 1 + 2 \cdot 2 = 6$, 2nd: $2 \cdot 1 - 2 \cdot 1 = 0$ and 3rd: $2 \cdot 1 + 2 \cdot 0 = 2$, the reducible representation, $[6,\ 0,\ 2]$ is recreated.

Table 2.1: C_{3v} point group table with the reducible representation for NV centers, Γ_{NV}, at the end.

C_{3v}	E	$2C_3$	$3\sigma_v$	Basis components	
A_1	1	1	1	z	$x^2 + y^2, z^2$
A_2	1	1	-1	R_z	
E	2	-1	0	$(x, y)(R_x, R_y)$	$(x^2 - y^2, xy)(yz, xz)$
Γ_{NV}	6	0	2		

With the *irrep* now known, the orbitals for the system can be found, written from lowest to highest energy: A_1', A_1 and $E_{x,y}$, where the E orbitals are degenerate [8]. Filling in electrons from the bottom, with a negatively charged NV center, fills up the A_1' and A_1 orbitals, and places an electron in each of the two $E_{x,y}$ orbitals. This is the ground state for the system and is the ${}^3A_2$ state, a triplet. This triplet ${}^3A_2$ state is shown in Figure 2.3 as the lowest energy state to the left. The system's excited state is then the ${}^3E$ state [8]. The transition between these two states is the 637 nm ZPL for NVs, which is what makes NVs fluorescing. The energy levels are even further separated within these two states, due to the spin interaction. They both have a lower-level $m_s = 0$ state and two higher-level $m_s = \pm 1$ states [8], shown in Figure 2.3 as the states above "± 1". The energy required to excite the state from $m_s = 0$ to $m_s = \pm 1$ is MWs with frequency: $D = 2.87$ GHz. The importance of this splitting will be discussed more below.

Transitions between energy levels can only occur if the spin is conserved. The transition ${}^3A_2 \rightarrow {}^3E$ is spin-conserved as both states are triplets. Transitions that change the spin are forbidden. There is another state that lies between the ${}^3A_2$ and ${}^3E$ states, but it is a singlet, ${}^1A_1$. Therefore the transition ${}^3E \rightarrow {}^1A_1$ is also a forbidden transition, under normal circumstances. However, research has shown, both theoretical predictions and empirical tests, that the transition from a triplet to a singlet can occur due to Intersystem Crossing (ISC), if the system is in one of the higher spin levels, $m_s = \pm 1$ [8]. The ISC is shown in Figure 2.3 as the grey arrow. There is still research being done on the transitions that occur after this ISC [8, 32]. The currently most likely theory shows the transitions ${}^3E_2 \rightarrow {}^1A_1 \rightarrow {}^1E_{1,2} \rightarrow {}^3A_2$. The transition in the middle of this chain, ${}^1A_1 \rightarrow {}^1E_{1,2}$ emits light with a ZPL at 1042 nm.

The two states with spin quantum number $m_s = \pm 1$ are almost degenerate at standard conditions [8]. The difference in energy is negligible. The introduction of a magnetic field, on the other hand, will split the two states further apart, bringing one of them lower and the other higher. The splitting of these states is shown in the Ground-state Hamiltonian to the system, which will be explained further in Subsection 2.1.4 [8], where the splitting of the states is shown to be dependent on the direction of the magnetic field. Why the direction of the $\boldsymbol{B}$ field matters to the system is due to the ”NV defect quantization axis”. The blue arrow shown in Figure 2.1, the vector pointing from the vacancy to the N-atom, is the NV defect quantization axis. The magnitude of the $\boldsymbol{B}$ field affecting the NV is dependent on the projection of the $\boldsymbol{B}$ field onto the NV defect quantization axis [8].

When in proximity to a $\boldsymbol{B}$ field, these $m_s = \pm 1$ states will split, as mentioned above. When they split, their resonant frequencies will also split from being degenerate to being one lower and one higher energy. They will split symmetrically around their original resonant frequency, 2.87 GHz. The distance between these two resonant frequencies can be used to calculate the strength of the **B** field [8], which will be explained in Subsection 2.1.4. MWs can be used excite the NV into $m_s = \pm 1$, then light can be used to excite the states from the ${}^3A_2$ state to the ${}^3E$ state. As the system is in the $m_s = \pm 1$ state, ISC can occur that changes the fluorescing light from 637 nm to 1042 nm. By filtering out the 1042 nm light using a cut-off filter, and measuring at which frequencies the intensity of the 637 nm light decreases, Optically Detected Magnetic Resonance (ODMR) can be performed [8, 9]. The next section will explain how through this ODMR, the magnitude of the $\boldsymbol{B}$ field can be calculated.

2.1.4 The ground state Hamiltonian of NVs

The Hamiltonian of a system is an operator equal to the total energy of the system. As the Hamiltonian is the sum of both the potential and the kinetic energy of all the parts of the system, the operator can be used to calculate changes in the system. For the NV defect center, the ground state spin Hamiltonian for the system is shown in Equation 2.2 [8], if hyperfine interaction with nearby nuclear spins in the diamond is ignored.

$$\mathcal{H} = hDS_z^2 + hE(S_x^2 - S_y^2) + g\mu_B \boldsymbol{B} \cdot \boldsymbol{S}, \tag{2.2}$$

where: z is the NV quantization axis, explained above, h is Planck’s Constant, D and E are the zero-field splitting parameters, S_x, S_y and S_z are the Pauli matrices, $g \simeq 2.0$ is the Landé

g-factor, μ_B is the Bohr magneton and $\boldsymbol{B}$ is the magnetic field.

The important part of Equation 2.2 for this Master Thesis is that the ground state Hamilton shows that the NV's energy has a change when in proximity to magnetic $\boldsymbol{B}$ fields. Equation 2.2 also gives the change in frequency for the magnetic resonance of the NVs through: $\pm g\mu_B \boldsymbol{B}$. By assuming that $(\nu_\pm - D)^2 >> E^2$ from Equation 2.2, and choosing to measure the magnetic field along the NV quantization axis, as that is the axis important for NV fluorescence, we obtain that the change in resonant frequency is equal to Equation 2.3:

$$\nu_\pm \approx \pm g\mu_B \boldsymbol{B}_{NV}/h. \tag{2.3}$$

The plus-minus notation comes from the fact that one m_s state decreases in energy and the other increases. As the two frequencies are found through ODMR, the only unknown in Equation 2.3 is the strength of the magnetic field, and this is how the strength of the magnetic field can be reconstructed through NVs:

$$\boldsymbol{B}_{NV} \approx \frac{(\nu_+ - \nu_-)h}{2g\mu_B}. \tag{2.4}$$

Equation 2.4 shows that the NV fluorescence is dependent on the projection of the $\boldsymbol{B}$ field onto the NV defect quantization axis. As NVs can have four orientations, shown in Figure 2.2, this means that the four orientations will split with a different magnitude, and four different resonant frequencies, $\nu_\pm$, can be obtained. These correspond to the four crystallographic directions in the crystal, which can be transformed to a full vectorial representation of the magnetic field [14].

2.1.5 Nitrogen Vacancy blinking

The NVs can not only be switched between their m_s states and their excited and ground state, but an NV can also be swapped to its neutral NV^0state, and back into NV^- [20]. This is illustrated in Figure 2.3 [20] on the right side, where the grey background visualizes the NV^0 as the "dark" state. The NV states are swapped by illuminating the NVs with light within the spectral range, $\approx 500...637$nm. This is because the electron from the excited NV^- gets excited into the conduction band. Similarly, NV^0 can be recombined to NV^- by capturing an electron from the valence band, while the NV^0 is in its excited state [33]. By switching between these two states, the system can go from the higher intensity NV^- fluorescence to blue-shifted, lower intensity NV^0 fluorescence, as shown in the emission spectrum in Figure 2.4 [26]. By filtering away as much of the NV^0 emission as possible, the NV^- will become the on-state of the system, with high intensity fluorescence, and the NV^0 will become the dark state of the system, with low intensity fluorescence.

The charge state swapping is dependent on the laser wavelength. Therefore the choice of wavelength of the laser used to illuminate the NVs decide the ratio of the on-time versus off-time, where on-time is when the NVs are in the NV^- state and off-time when they are in the NV^0 state [20]. The equation for the ratio is shown in Equation 2.5. In the region of interest, this ratio is inversely proportional to the wavelength of the laser to the power of a constant 'A', which is an unknown variable [20]:

$$r = \frac{\tau_{on}}{(\tau_{on} + \tau_{off})} \propto \lambda_L^{-A}, \tag{2.5}$$

where: r is the ratio between the on-time (τ_{on}) and the off-time (τ_{off}), τ_{on} is the on-time in seconds, τ_{off} is the off-time in seconds, and λ_L is the wavelength of the laser. At $\lambda_L = 580$ nm the ratio is $r \approx 0.3$, at $\lambda_L = 594$ nm, the ratio is $r \approx 0.1$, and at $\lambda_L = 610$ the ratio is $r < 0.05$ [20] .

The wavelength only changes the ratio between the on- and off-times. The on- and off-times themselves depend upon the laser intensity. In this too the on- and off-times are inversely dependent upon the laser intensity: $\tau_{on}, \tau_{off} \propto I_L^{-2}$ [20]. At laser intensities around $I_L \approx 1$ kW/cm^2, an approximate equation for calculating the on-time can be found, as shown in Equation 2.6 [20] .

$$\tau_{on} \approx \frac{2}{I_L^2}, \tag{2.6}$$

where: I_L is the laser intensity in kW/cm^2. Equation 2.6 shows that a laser intensity of $I_L = 1$ kW/cm^2 gives an on-time of $\tau_{on} \approx 2$ s.

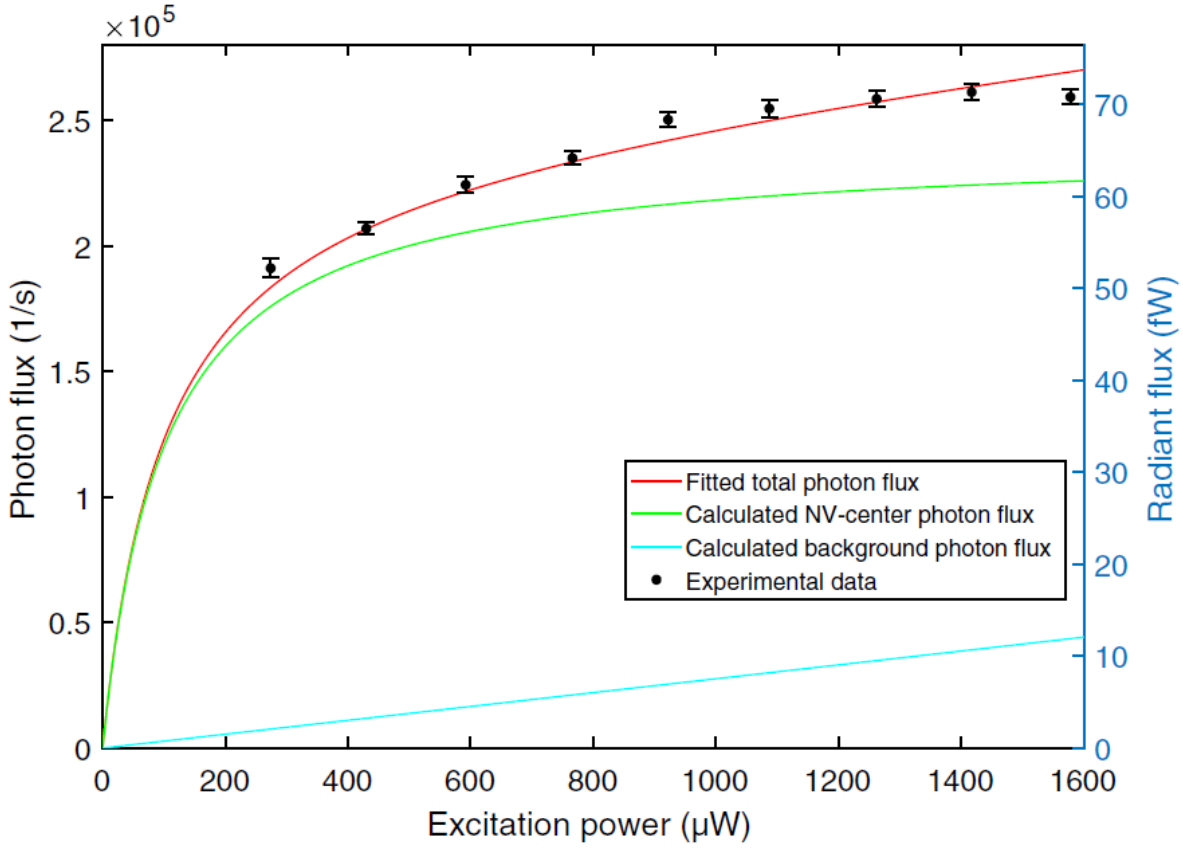

Figure 2.5: The photon flux (1/s) and radiant flux (fW) of an NV dependent on the excitation power from a laser with 532 nm. At ~34 μW excitation power, the radiant flux is ~ 18±3 fW. Figure taken from [34].

The photon and radiant flux of an NV excited by a laser with 532 nm is shown in Figure 2.5. This figure shows expected fluorescent power from a single NV dependent on the excitation power. The easiest settings and setup to use to see NV blinking is to have an on-time ratio of $r = 0.1$ and an on-time of $\tau_{on} = 2$ s [20]. This corresponds to a wavelength of $\lambda_L = 594$ nm and a laser intensity of $I_L = 1$ kW/cm^2. This causes the NVs to be on for roughly 2

s, and then stay off for another 20 s. This makes the NVs look like they are blinking, and changing parameters to obtain the optimal setup for observing the blinking of these NVs is the majority of the work in this Master Thesis.

2.1.6 Stochastic optical reconstruction microscopy

The blinking of NVs is a stochastic process, as it has a chance to go over to NV^0 from NV^-. Stochastic Optical Reconstruction Microscopy (STORM) is a microscopy technique that uses the stochastic properties of fluorescence to obtain sub-diffraction optical imaging [19]. STORM functions by first recording an image with several fluorophores, like NVs. Through the illumination of the laser, with an intensity below the saturation level, only some of these fluorophores will activate and the camera will register their fluorescence. STORM requires that only a single fluorophore is fluorescing in each image [19]. To make sure of this, the intensity of each image is measured, and the amount of fluorophores in the image is calculated. From there, only the images with one fluorophore is saved. By continuously illuminating the fluorophores with the laser, over time different fluorophores will be active and images of each one will be saved. To obtain super resolution from these images, the fluorescence center of each of these images is calculated. This is done by using all the photons from the image to calculate the center of the fluorescence. By doing this for every image taken, i centers with position $[x_i, y_i]$ will be found, where i is the amount of fluorophores in the focus. The new locations for the fluorophores in the image will have a resolution higher than the diffraction-limited resolution [19].

The position of the NVs can be decided with sub-diffraction-limited position, through STORM explained above, and their spin spectral information can be found through the ODMR [20]. STORM will be performed as mentioned in the previous paragraph, but ODMR will be performed at the same time. This is done by finding the resonance frequencies of the NVs in the focus first, using conventional ODMR, briefly explained at the end of Subsection 2.1.3. After the resonance frequencies have been found, the camera will continuously take images with exposure time equal to the on-time of the NVs, while the MW emitter will cycle through the resonance frequencies, synced up with the cameras images. One image equals one resonance frequency. For two NVs in the focus, there will be four resonance frequencies: ν_1, ν_2, ν_3, ν_4. The resonance frequency belonging to each of the NVs will be mirrored, so one NV has the lowest ν_1 and the highest ν_4 frequency, and the other has the two frequencies in the middle: ν_2 and ν_3. The fluorescence centers of the NVs will be calculated for each of these resonant frequencies, obtaining four in total. Then, within the same image, add the location distributions for the first NV, ν_1 and ν_4, and subtract the location distributions for the second NV, ν_2 and ν_3, and an image will be obtained showing both sub-diffraction-limited position of both of the NVs together with the NVs' spin spectral information [20].

2.2 Microscopy

Microscopy is the area of research about magnifying objects that are too small to be visible to the naked eye. Microscopy has been an invaluable part of several research areas, especially within biology [35]. Three of the biggest types of microscopy are optical, electron and scanning probe microscopy. Optical microscopy uses light and lenses to enhance the size of the image of the object, which will be detailed in Subsection 2.3.1 [36]. Electron microscopes use magnetic fields to focus an electron beam, similar to lenses and a beam of light for optical microscopes, to investigate a sample [36]. Both the auger and the secondary electrons can then be used to obtain information about the sample. Scanning probe microscopy uses a probe with a tiny tip, sometimes as small as a single atom in diameter, to scan over the surface of a sample and obtain information about the sample through the interaction between the probe and the sample [36].

Optical microscopy is the focus of this Master Thesis, and within optical microscopy we have two main types: far-field and confocal microscopy. Far-field microscopy images the entire sample at once, meanwhile confocal microscopy images a tiny part of the sample, a pixel, at a time until the entire sample has been imaged [36]. The most common type of far-field microscopy is bright-field microscopy. Bright-field microscopy is imaging a sample by shining a light on the sample, often from below, and then looking at the resulting image from the transmitted image [36]. Dark-field microscopy is another common far-field microscopy technique, though not as common as bright-field. Dark-field is the same as bright-field, but the 0th order of the diffracted light, so the light going straight through, is removed and the 1st order and higher diffracted light is imaged instead. Diffraction will be explained in the next section. Dark-field microscopy is especially useful because of how it increases the contrast in the image [36].

2.2.1 Diffraction and resolution

Diffraction is the phenomena that occurs when light bends around another object [37]. From Huygen's Principle, this occurs due to every single point of the wavefront, the propagating wave, can be considered to be its own point source for the wave [37]. Therefore, when the light wave comes into contact with a small slit, every part of the wave passing through the slit can be considered its own point source. The diffraction pattern after this slit is dependent on the phase difference between these point sources, when they reach a screen, or a camera, afterwards. This phase difference is caused by different length travelled by each point source, and maxima will occur where all of these point sources are in phase. The distance between these maxima is therefore dependent on the wavelength of the light, causing diffraction to be dependent on the wavelength of the light used. As diffraction is the main limiter to resolution, this causes resolution to be dependent on the wavelength as well, which will be seen in Equation 2.7. Microscopy is all about magnifying small objects, as explained at the start of this section, and therefore diffraction becomes important as the objects to magnify get smaller.

Because of diffraction, there is a size for far-field microscopy where two objects will become indistinguishable. This is called the diffraction limit [38]. The diffraction limit decides what

is the theoretical highest resolution a microscope can have. There are several equations for calculating the lateral resolution of a microscope, the distance two objects can have between each other and still be distinguishable. The Rayleigh diffraction limit is shown in Equation 2.7 [36, 39, 40].

$$d = 0.61\frac{\lambda}{2n\sin\theta} = 0.61\frac{\lambda}{NA}, \tag{2.7}$$

where: d is the distance between the two objects, λ is the wavelength of the light, n is the refractive index of the medium, and θ is the half-angle of the spot where the light is converging. The angle and refractive index have been combined into a single variable called the Numerical Aperture (NA), and is specific for each microscope. The term ”super-resolution” is used to refer to setups that manage to go beyond the diffraction limit and obtain sub-diffraction-limited resolution [41].

2.2.2 Confocal imaging

When imaging fluorescent samples with optical imaging, confocal microscopy is widely used as a way to increase the resolution, compared to far-field microscopy [42]. Confocal imaging is done by focusing a laser to a small point on a sample. The laser causes the sample to fluoresce [43] and this fluorescence signal is then focused onto a pinhole so only the fluorescence in focus is kept [44]. For Confocal Laser Scanning Microscopy (CLSM) the focused laser will illuminate and excite the sample point by point, in a rasting scanning matter. A sensor will measure the intensity of the fluorescence at each of these positions [36]. The intensity of each position becomes a single pixel in the finished image from CLSM. The size of each of these pixels compared to the sample is dependent on the size of the focused laser spot on the sample [36]. The distance moved between each pixel should be ~ 3 times smaller than the objective lens's resolution. This is to satisfy Nyquist's sampling frequency [45], explaining that sampling needs to be at least twice the sampling frequency to accurately recreate the signal. Confocal imaging is a great tool for imaging fluorescent samples due to how simple the setup is, how high the resolution is and how customizable the setup can be. The drawback of confocal imaging is that it requires a fluorescent sample, there is a huge loss of the fluorescence signal [46] and the imaging is time consuming [36].

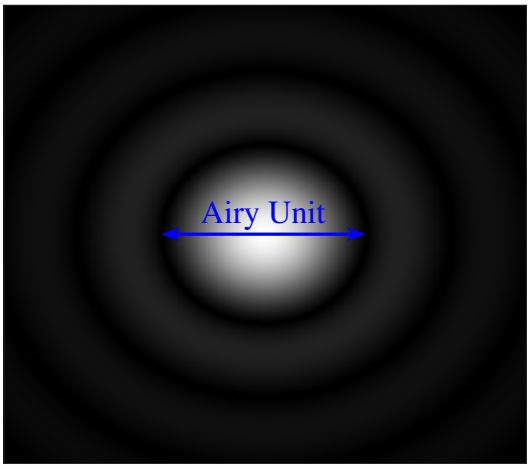

Figure 2.6: The Airy disk simulated from the squared Sombrero function using MATLAB. The Airy Unit is drawn in with the blue arrow.

When the confocal spot is as small as it can be, diffraction limited, it will take the shape of an Airy Disk, due to diffraction [47]. An Airy Disk can be seen in Figure 2.6, a spot with a maximum in the middle with waves of minima and maxima alternating around it. The size of the central maximum, the width between the first two minima, of the Airy Disk can be defined with the Airy Unit (AU), as shown in Figure 2.6 with the blue arrow.

Only the central maximum is desired to be used for confocal imaging, to improve the resolution from brightfield microscopy. The spot is therefore focused onto a pinhole to remove all the signal apart from the central maximum. How much of the spot, both axially and laterally, passes through the pinhole is dependent on the size of the pinhole compared to the AU [48]. In general, the smaller the pinhole, the less of the spot both axially and laterally get through the pinhole. Ideally, a pinhole will be between 1 and 0.5 times the size of a spot's AU in the pinhole plane. Pinholes and their effect on the resulting image is discussed further in Subsection 2.4.4.

2.2.3 Fluorescence

Fluorescence is a material's property to absorb light or other electromagnetic waves, and then to release that absorbed energy by emitting light of a different wavelength [41, 44]. Fluorescence occurs because the energy of the radiating light is of an appropriate energy order to excite the electronic state to its excited state. Fluorescence is the property when this excitation and relaxation do not include a change in the spin multiplicity of the electron [44]. When the spin multiplicity changes, it is called phosphorescence [49]. In fluorescence, the wavelength of the emitted light is usually of a longer wavelength than the excitation light. This is due to the excitation light often has an energy slightly higher than the exact distance between the energy levels, to excite as many of the fluorescent atoms, or parts, as possible. The emitted light will therefore be of a lower energy, meaning a lower frequency from $E = hv$ [50], where E is the energy, h is Planck's constant and v is the frequency. The lower frequency therefore means a longer wavelength due to $\lambda = \frac{c}{v}$

2.3 Optics

Optics is the part of physics about visible light, ultraviolet light and infrared light [37]. Light is both a particle, photon, and an electromagnetic wave. An electromagnetic wave is a wave that moves in a direction, Z, and has an electric field and a magnetic field that oscillate perpendicular to each other and the Z-direction [37]. Light's properties as a wave is the focus of optics.

The theory in this Master Thesis will use the geometrical optics assumption. The geometrical optics assumption assumes that light travels in straight lines [37] and ignores the wave nature of light. Therefore interactions such as diffraction, explained in Section 2.2.1, will be ignored. The interaction between light and other materials, especially lenses, is the focus in this section.

2.3.1 Lens theory

Lenses are transparent materials, usually made of glass, that either converges or diverges a beam of light [37]. For focusing light, converging the light, a convex lens is used. When light passes through a medium, the light gets bent slightly inside of the medium. This change in direction for the light is determined by Snell's law, shown in Equation 2.8 [37]:

$$\frac{\sin\theta_2}{\sin\theta_1} = \frac{n_1}{n_2}, \tag{2.8}$$

where: θ_1 and θ_2 are the angles of incidence for material 1 and 2 respectively, and n_1 and n_2 are the refractive indices of material 1 and 2 respectively. Angles of incidence is the angle between the beam of light and the normal from the material, where the light hits. The refractive index is a number for the speed of which light passes through a material and is calculated as $n = c/v$, where c is the speed of of light in vacuum and v is the speed of light in the material. Vacuum has a refractive index of 1 and air has a refractive index of $\sim$1.0003, and will therefore assumed to be $\sim$1 [37].

A lens can be used to change the perceived size of an object [37]. For a convex lens, if the object's position is further away than the lens's focal length, $u > f$, where u is the distance between the object and the lens, and f is the focal length of the lens, then a real image will be created. A real image is an actual image that can both be seen by a person and be projected onto a screen. A real image is upside down, as shown in Figure 2.7. A virtual image occurs when the object's position is closer than the lens's focal length, $u < f$. A virtual image is an image that does not in fact exist in that position, but has been refocused again either by a lens or your retina to create a real image afterwards. Magnifying glass, for example, use virtual images to magnify the size of the object it is focusing on.

To calculate the magnification of the image of an object, several equations will be shown first. First, to calculate the effect a lens has on a beam of light, in air, the lens equation is used, as shown in Equation 2.9. This equation is used to find the focal length of a lens. The focal length of a lens is important as it can be used to calculate the magnification of a lens and to calculate if an image is virtual or real.

$$\frac{1}{f} = (n-1)\left[\frac{1}{R_1} - \frac{1}{R_2} + \frac{(n-1)d}{nR_1R_2}\right], \tag{2.9}$$

where: f is the focal length of the lens, n is the refractive index of the lens material, R_1 is the radius of curvature closest to the light source, R_2 is the radius of curvature furthest from the light source and d is the thickness of the lens. If a lens is significantly thin compared to the radii of curvature of the lens, meaning $d << R_1R_2$, Equation 2.9 can be simplified to the thin lens equation [37]:

$$\frac{1}{f} \approx (n-1)\left[\frac{1}{R_1} - \frac{1}{R_2}\right]. \tag{2.10}$$

Equation 2.10 can further be used to prove Equation 2.11 [37, 51], if the lens is in the air and $n_{air} \approx 1$:

$$\frac{1}{v} + \frac{1}{u} = \frac{1}{f}, \tag{2.11}$$

where: v is the distance from the object to the lens, and u is the distance from the lens to the image. u uses positive sign for real images and negative sign for virtual images. Lastly we get to Equation 2.12, the equation to calculate the magnification of the image. Equation 2.12 can be derived through trigonometry together with: $M = \frac{\text{Height of image}}{\text{Height of object}}$ [37].

$$M = -\frac{u}{v} = \frac{v - f}{f}, \tag{2.12}$$

where M will be negative for real, or inverted images, and positive for virtual, or non-inverted ,images.

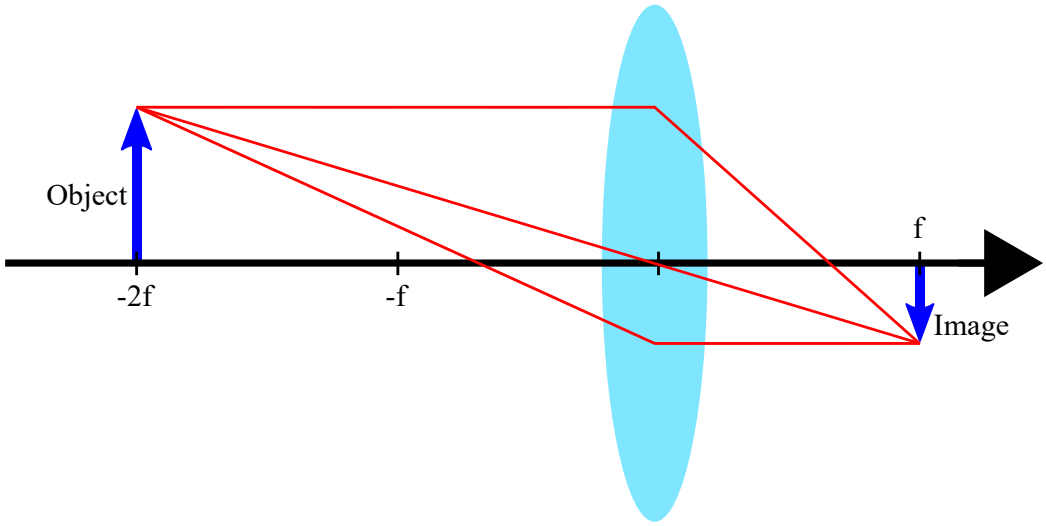

Figure 2.7: Example of how a real image can be formed with a thin lens. The length of the blue ”Object” and ”Image” arrows indicate the heights of the object and the real image respectively.

2.4 Instrumental background

2.4.1 Camera

A camera can be used as the screen to visually show a real image created through optics, as explained in Subsection 2.3.1. The main type of camera used for imaging today is the Complementary Metal Oxide Semiconductor (CMOS) camera [52]. When light hits the CMOS, the CMOS converts the charges to voltage per pixel [53], instead of all of them at once as a package.

2.4.2 Photomultiplier tube

A Photomultiplier Tube (PMT) is a category of highly sensitive photon detectors [54, 55]. PMTs are known for their high gain, low noise and high frequency. However this also makes them sensitive to background noise and stray light. PMTs also have a relatively low threshold of incident light power which can saturate the PMT. If exposed to light power above this saturation threshold, the PMT’s performance can be worsened or ruined.

PMTs work by letting the incident photons strike a photocathode. The photocathode will emit primary electrons due to the photoelectric effect [54]. The photoelectric effect occurs when an electron absorbs a photon with more energy than its binding energy. This can cause the electron to be ejected from the material. The primary electrons are then directed to dynodes using electrodes. The primary electron will hit the dynode, causing it to emit several lower energy, secondary electrons, multiplying the amount of electrons. The dynodes are designed so the secondary electrons will hit the next dynode. Each subsequent dynode is held at a more positive potential than the previous, causing each electron to hit the next dynode with the energy of a few hundred eV [56]. This causes each secondary electron to multiply to several secondary electrons with each dynode. By having several dynodes in the PMT, the amount of electrons can be multiplied by factors upwards to $2 \cdot 10^7$ [54]. When all the electrons hit the anode at the end, a large current pulse will be generated, that's easily detectable by equipment such as an oscilloscope.

2.4.3 Laser

A "laser" originally rose from the term "Light Amplification by Stimulated Emission of Radiation" [57]. The simplest form of a laser consists of 3 parts: A pump, to apply energy to the laser, a gain medium, to amplify the photons and a pair of mirrors, one highly reflective and one partially reflective [58, 59]. The light will travel back and forth between the two mirrors, passing through the gain medium with each pass and generating more photons. In this medium stimulated emission occurs, creating the laser light. The pump will keep applying energy to the system to allow the system to keep going, even as some of the light escapes the laser through the partially reflective mirror.

Stimulated emission is a different type of light emission from electrons, compared to normal, or spontaneous, emission [60]. Stimulated emission occurs when a photon interacts with an already excited electron and causes the electron to relax to its ground state by emitting a photon of the same phase, frequency, polarization and direction of travel as the incident photon [37, 60]. As there are more electrons in the ground state compared to electrons in the excited state, at equilibrium, to obtain stimulated emission this needs to be swapped. By having more electrons in the excited state, stimulated emission will become favourable compared to absorption of the photon and spontaneous emission.

The light from a laser is useful due to the high coherence of the light [37, 60]. Coherence of light is a term used to measure how much the beam changes over time, temporal coherence, and over distance, spatial coherence. Temporal coherence is a measure of how much the beam changes throughout its propagation direction: How much the phase of the laser shifts over time travelled. Spatial coherence is a measure of how much the beam profile changes at a given location: If the intensity of the beam is similar for every location with a given radius, r. The high temporal coherence of lasers cause them to have a narrow band, narrow enough for lasers to be considered to be of a single wavelength. The high spatial coherence of lasers cause them to widen slowly, they stay a narrow beam for a long distance. Both the temporal and spatial coherence are important, the temporal to choose the specific wavelength of the light we need, and the spatial coherence so the intensity of the beam is predictable.

2.4.4 The laser spot

A laser beam is usually assumed to have a Gaussian distribution [61]. A Gaussian distribution is shown in Figure 2.8. A laser can be assumed to be Gaussian due to its high spatial coherence, meaning that the intensity of the laser perpendicular to its propagation direction follows a Gaussian distribution.

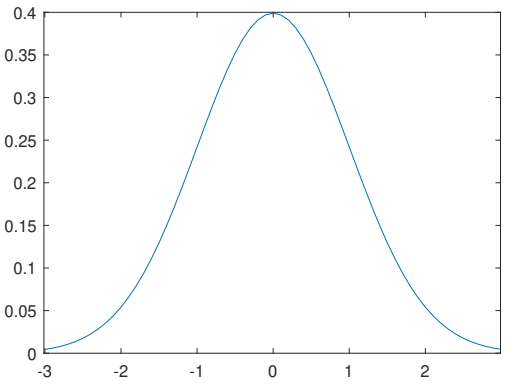

Figure 2.8: The standard Gaussian distribution with μ = 0 and σ^2 = 1.0. The Y-axis is the probability density and X-axis is μ - xσ^2.

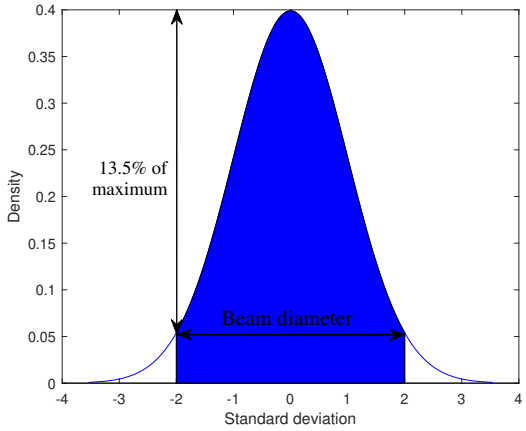

Figure 2.9: The standard Gaussian distribution shown in Figure 2.8, but with the width at 4 times the standard deviation drawn in.

When a laser is focused into a spot, the size of the spot, its diameter, can be calculated, and calculating this spot size is an important part of this Master Thesis. The size of the spot is a measure of how small, and how well focused, the laser beam is. The spot size can further be used to calculate when the spot is diffraction-limited, and to know how many NVs there are in the spot [20]. The intensity of a Gaussian beam in the spot dependent on the radius from the center of the beam is given by Equation 2.13 [62, 63]:

$$I(r) = I_0 exp\left(-\frac{2r^2}{w^2}\right), \tag{2.13}$$

where: $I(r)$ is the intensity dependent on the radius, I_0 is the maximum intensity of the spot, r is the radius out of the center of the spot, and w is the width of the spot. Equation 2.13 is what enables lasers to be assumed to be Gaussian, as it gives a similar plot shown in Figure 2.8. By choosing $r = w$ in Equation 2.13, this is where the radius equals the width of the spot, a representation of the intensity of the beam width can be acquired:

$$I(r = w) = I_0 exp(-2) = I_0 \frac{1}{e^2}. \tag{2.14}$$

Equation 2.14 shows that the intensity of the beam width is $\frac{1}{e^2}$ times the total intensity of the spot. Since $\frac{1}{e^2} \approx 0.13534 \approx 13.5\%$ means that the beam diameter is approximately equal to the width of the spot at 13.5% of the spot's maximum intensity.

As it is a Gaussian distribution, a representation for the width of the beam depending on the Full-Width at Half Maximum (FWHM) of the beam can be acquired. By choosing $I(r) = \frac{I_0}{2}$

for Equation 2.13, the intensity of the beam at 50% of the max, $2r$ will be the FWHM of the beam and the equation can be simplified, showing that the width of a Gaussian beam is approximately equal to $1.7\cdot$ FWHM:

$$2w = \sqrt{\frac{2}{ln(2)}}\text{FWHM} \approx 1.7 \cdot \text{FWHM}. \tag{2.15}$$

For a perfect Gaussian beam, the $\frac{1}{e^2}$ width is the same width as 4 times the Standard Deviation (SD) of the Gaussian distribution. This comes from the nature of the Gaussian distribution. This can therefore be used to also calculate the width of the beam and takes the 2-dimensions of the beam into consideration, and not just a single dimension, causing the calculations to be more accurate. The beam width drawn in for 4 times the SD of a Gaussian distribution slice is shown in Figure 2.9. This is therefore the ISO standard for calculating the with of a Gaussian laser [64]. To calculate the spot when knowing the SD in the X- and Y-directions, in pixels, Equation 2.16 is used:

$$d_{spot} = 2(\sigma_X + \sigma_Y) \cdot p_{nm/pixel}, \tag{2.16}$$

where: d_{spot} is the width of the spot in nm, σ_X and σ_Y are the SDs in pixels of the Gaussian fit in X- and Y-directions respectively, and $p_{nm/pixel}$ is the size of the image projected onto the camera for each pixel nm/pixel.

2.4.5 Pinhole image

With an equation for the width of the beam, and having an Equation to calculate between FWHM and the width at $1/e^2$ of the maximum, Equation 2.15, the full 3D image after the pinhole can be calculated [48].

To calculate the Airy Unit (AU) [65], shown in Figure 2.6, from an objective lens, The Rayleigh Criteria, Equation 2.7, can be used, with the introduction of the magnification of the objective lens. Equation 2.17 shows how the AU is calculated [66]:

$$\text{AU} = \frac{0.61 \cdot \lambda_{em} \cdot \text{ M}}{\text{NA}}, \tag{2.17}$$

where: AU is the Airy Unit in nm, λ_{em} is the emission wavelength from the fluorescent sample, M is the magnification of the objective lens, and NA is the Numerical Aperture of the objective lens, in the case there is only one lens.

The FWHM of the axial-resolution of a diffraction limited spot is equal to the depth of an image that passes through a pinhole. The FWHM of the axial-resolution from an objective lens through a pinhole can also be calculated, as shown in Equation 2.18 [48, 46, 42, 38]:

$$\text{FWHM}_{\text{axi}} = A(\text{PH})\frac{\lambda_{ex}}{n - \sqrt{n^2 - NA^2}}, \tag{2.18}$$

where: λ_{ex} is the wavelength of the excitation light, n is the refractive index, and $A(\text{PH}) = (0.64{-}0.88)$ is a factor that's multiplied to the equation depending on the pinhole size [38]. At

pinhole sizes PH < 0.25 AU, where PH is the pinhole size and AU is the Airy Unit, $A = 0.64$. At pinhole sizes, 1 < PH < ∞, $A = 0.88$. At pinhole sizes between this, the appropriate value between these two is chosen.

To calculate the full volume of the signal that gets passed through the pinhole, calculated through the width of the beam and the depth of the image after the pinhole, a simplification is made. The beam focus is assumed to be cylindrical rather than diverging out above and below the focus. This is to make the calculations easier and is an acceptable assumption as the beam diverges slowly at these short lengths, and the depth after a pinhole follows a Gaussian curve as well, decreasing the intensity at top and bottom [38]. The volume of a cylinder is calculated through Equation 2.19:

$$V = 2\pi r^2 h = 2\pi \left(\frac{4\sigma_{lat}}{2}\right)^2 \cdot 4\sigma_{axi}, \tag{2.19}$$

where: $4\sigma_{lat}$ is the width (w) of the beam at 4σ, and $4\sigma_{axi}$ is the depth of the image calculated through Equation 2.18 and Equation 2.15.

2.5 Statistics

In Subsection 2.4.4 the SD is used to calculate the width of the spot, as shown in Equation 2.16. The statistics regarding SD and variance will therefore be detailed mathematically in this Section. Gaussian fits were also explained in Subsection 2.4.4, and so Subsection 2.5.2 starts by showing a statistical example of comparing a fitted value to the real value through the least squares method. This comparison can further be used to compare fits to mathematically find the best fit.

2.5.1 Standard deviation

The Standard Deviation (SD, or σ) is a common tool used in statistics to calculate the spread of a set of values compared to their mean [67]. It is relatively easy to calculate the SD of a set of values, as shown in Equation 2.20. Therefore SD is a simple tool to compare the spread of values between measurements.

$$\sigma = \sqrt{\frac{1}{N-1}\sum_{i=1}^{N} |A_i - \mu|^2}, \tag{2.20}$$

where: σ is the standard deviation, N is the number of data points, A_i is data point i and μ is the mean of A_i calculated as [67]:

$$\mu = \frac{1}{N}\sum_{i=1}^{N} A_i. \tag{2.21}$$

The variation of a set of values compared to their mean can also be calculated, and is a measure of the squared deviation between the value and its mean. The equation for variation is simply the square of the SD [67], as shown in Equation 2.22:

$$\sigma^2 = \frac{1}{N-1}\sum_{i=1}^{N}|A_i - \mu|^2, \tag{2.22}$$

where: σ^2 is the variance.

2.5.2 Other statistics equations

When making a fit to a group of data, one way to calculate the best fit is to use the least squares method. The least squares method calculates the sum of of the square of the difference between the actual data point and the fitted data point, as shown in Equation 2.23 [67]. The least squares method then compares this fit to another fit to see which fit had the smallest value of S. Another code needs to be used to generate the different fits.

$$S = \sum_{i=1}^{N} r_i^2 = \sum_{i=1}^{N}(y_i - \hat{y}_i)^2, \tag{2.23}$$

where: S is the sum of squares estimate, y_i is data point i, and $\hat{y}_i$ is the data point fit for y_i.

A method called the Root Mean Square (RMS) can be used to calculate a value similar to the mean in Equation 2.21. The convenient part about the RMS is that it calculates how much a current is varying, as negative values will also be included [37], and is calculated as shown in Equation 2.24:

$$x_{RMS} = \sqrt{\frac{1}{N}\sum_{n=1}^{N}|x_n|^2}, \tag{2.24}$$

where: x_{RMS} is the RMS, and x_n is data point n.

Chapter 3

Experimental setup

This chapter lists and explains all of the equipment used in our setup to image the fluorescence from NVs, focus the fluorescence onto a pinhole and detect the signal behind the pinhole with a sensitive detector to detect the blinking of a single NV, to later perform STORM. It will also explain the equipment necessary to perform ODMR on the NVs, which can be performed at the same time as STORM. It explains our reasoning for using each of the parts, how they function in our microscope and their relevant properties. The chapter starts by listing the properties of the ultra-pure Chemical Vapor Deposition (CVD) diamond samples used as our NV samples. After that, a schematic of our setup and a list of all of our equipment are shown. The properties of the camera, PMT and the Si amplified photodetector in our setup are explained afterwards. Then our choice of laser, followed by the mirrors and lenses used to route the optical path, will be explained. The reasoning for our optical filters, both the shortpass and longpass filters and the Neutral Density (ND) filters, will be explained. The chapter ends with our choice of pinhole size and piezo stages.

3.1 Diamonds

The two ultra-pure diamonds used in this Master Thesis were both Chemical Vapor Deposition (CVD) diamonds bought from Element Six. The first diamond was a ”bright” diamond named ”SC Plate CVD 3.0x3.0mm, 0.25mm thick, <100>, PL”, while the second diamond was a dimmer diamond named ”EL SC Plate 2.0x2.0mm, 0.50mm thick”. The properties of the two diamond samples are listed in Table 3.1. The bright sample was bright due to a higher Nitrogen content and hence a higher density of NVs. The bright sample had a Nitrogen concentration of < 1 ppm while the dim sample had a concentration of < 5 ppb used in the manufacturing. As previously stated in Subsection 2.1.2, typically only $< 0.5\%$ of the N used in the CVD process gets incorporated into the diamond as NVs [28]. This means that the bright sample had an NV concentration of < 5 ppb and the dim sample had a concentration of < 0.03 ppb, yielding a nearly 2000 times larger NV concentration in the bright sample over the dim.

To increase the amount of fluorescence from the NVs that is measured by our camera and sensor, the two single-crystal diamonds were coated in a reflective layer of aluminium. This was done so the NV fluorescence that would not be captured by our objective lens would instead be reflected back to the objective lens by the reflective layer. We did this in the hopes

Table 3.1: The properties of the two diamonds.

	Bright sample SC Plate CVD	Dim sample EL SC Plate
Nitrogen conc. [ppb]	< 1,000	< 5
NV conc. [ppb]	< 5	< 0.03
Dimensions [mm]	3.00 x 3.00 x 0.25	2.0 x 2.0 x 0.50
Edge orientation	<100>	<110>
Face orientation	{100}	{100}
Side 1, Roughness	Polished, Ra < 30 nm	Polished, Ra < 5 nm on {100} face
Side 2, Roughness	Lapped, Ra < 250 nm	Polished, Ra < 5 nm on {100} face

that more of the fluorescence from the diamonds would reach the sensor and cause a NV^- and the NV^0. The dim diamond was only coated across half of its surface to compare the fluorescence with and without the coating.

3.1.1 Fluorescent samples

In addition, we used two other fluorescent samples apart from the single-crystal diamonds: A sample of nanodiamonds originally dispersed in water, but dried on a coverslip, and a sample of Rhodamine 640 Perchlorate. Both of the samples were wedged between to coverslips with ProLong Gold [48]. This was done so the samples would have the same refractive index throughout the entire sample. The nanodiamond sample was from Carbodeon and did not have any extra Nitrogen implemented into them, so the NV centers that could be detected from them had to be created naturally in the diamonds. The nanodiamonds had a crystal size of 4.0 - 6.0 nm, and the solids in the dispersion were ≥97 wt.%. When we prepared the nanodiamonds sample, we added a few drops of distilled water to dilute the sample, before letting the sample air dry.

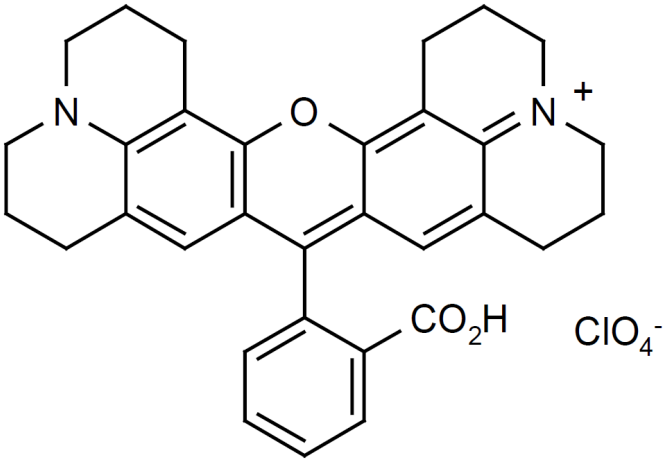

Figure 3.1: The structure of Rhodamine 640 Perchlorate. Figure taken from Exciton's sheet on the compound [68].

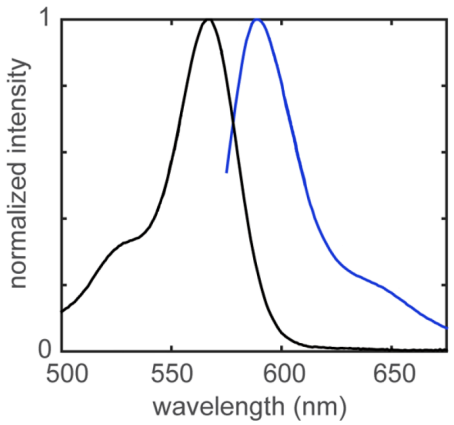

Figure 3.2: The fluorescence spectrum of Rhodamine 640 Perchlorate. Black graph shows absorption and blue shows emission spectrum. Figure adapted from [69].

For the Rhodamine sample, the structure of the fluorescent molecule is shown in Figure 3.1 [68], while spectra is shown in Figure 3.2 [69]. The Rhodamine fluorescence's intensity is several orders of magnitude higher than the NV's. Therefore, even though most of the fluorescence was filtered away, the signal was still extremely high compared to the NVs'. The Rhodamine samples were used to test the confocal setup.

3.2 Microscope setup

The microscope equipment used in this Master Thesis is listed and motivated in this Section. This is to give the properties of our equipment, justify our choice of equipment and to make our experiments reproducible. The main equipment of the microscope setup is listed in Table 3.2, to give a quick overview of the equipment. A schematic of the setup used in this Master Thesis can be seen in Figure 3.3. Photos of the setup are also provided and are shown in Figures 3.4 - 3.6.

Table 3.2: Short explanation of the microscope equipment.

Equipment name	Description
Laser	A laser with wavelength 594 nm and maximum power 5 mW.
Beam expander	Used to widen the laser-beam, to allow it to cover the entire back-aperture of the objective lens, to obtain as high resolution as possible.
CMOS camera	A camera to image the image plane.
PMT (Photomultiplier tube)	A photomultiplier tube to measure photons, a highly sensitive instrument used to measure the small changes in fluorescence from the NVs' blinking.
4 metallic mirrors	Silver mirrors with high % of reflection designed to steer the optical path.
Flip-up mirror	A metallic mirror like the previous ones, but able to be lifted up or down to let the light-path travel to the CMOS camera or the PMT as needed.
Dichroic mirror	A mirror that allows both transmission and reflection. Used to guide the laser to the objective lens, then to guide the fluorescence to the CMOS camera and the PMT.
Objective lens	Used to focus the laser to a point on the sample. Then used to make the fluorescence parallel.
2 Focusing lenses	Used to focus the fluorescence on the CMOS camera and PMT.
Shortpass filter	Shortpass filter with cut-off wavelength 750 nm.
Longpass filter	Longpass filter with cut-on wavelength 650 nm.
Neutral Density (ND) filters	Filters used to reduce the power of the laser.

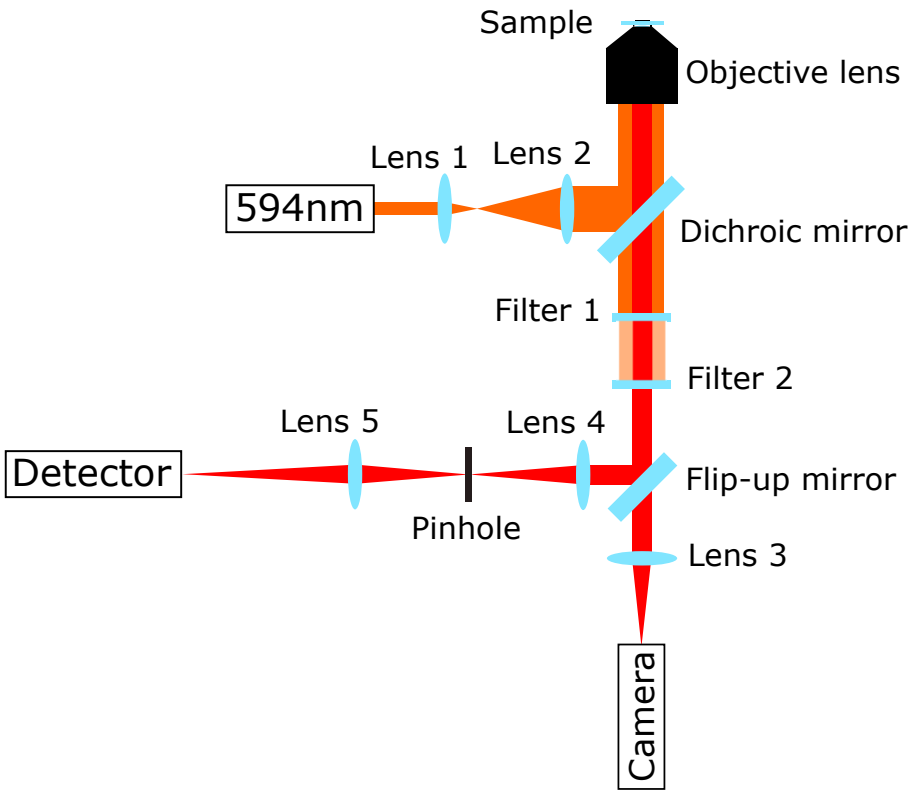

Figure 3.3: A schematic of the setup used in this Master Thesis.

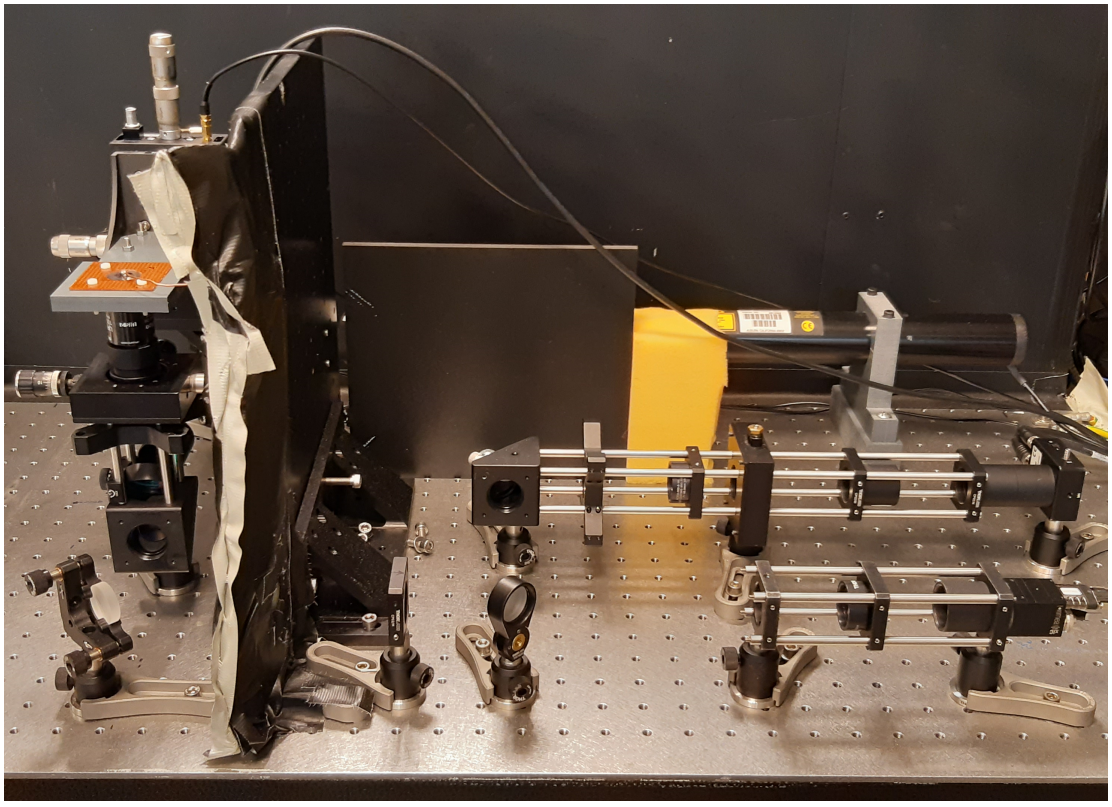

Figure 3.4: Setup shown from the side. The filters, ”Filter 1” and ”Filter 2” are shown in the front together with the flip-up mirror and the camera on the right. The optical beam-path for the photodetector is shown in the middle. The MW antenna can be seen over the diamond on the left.

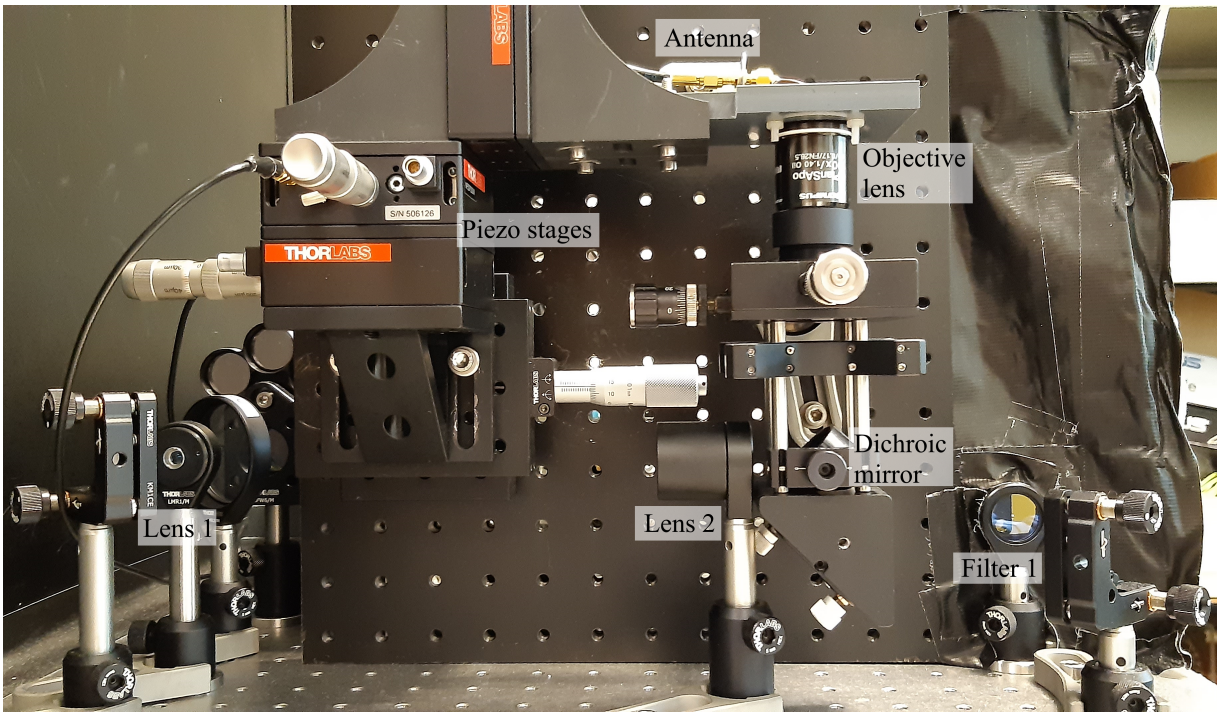

Figure 3.5: Setup from the sample side showing the beam-path, the ND filter, the beamsplitter and the expander lens, ”Lens 1” on the left. The piezo stages, the objective lens, with the dichroic mirror underneath and the leans to make the beam parallel, ”Lens 2”, in the middle. The first filter, ”Filter 1”, on the right.

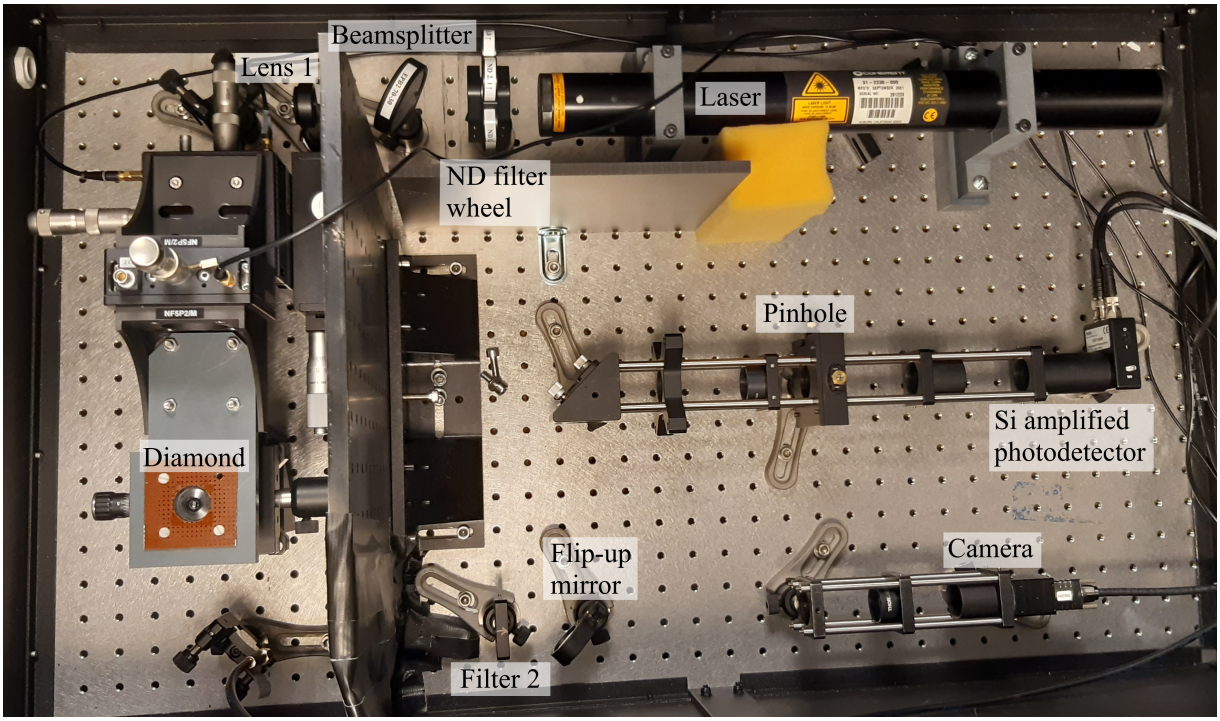

Figure 3.6: Setup inside box shown from above. The laser with the ND filter and beamsplitter on the top. The sample, piezo stage and the photodetector beam-path in the middle. The two optical filters, ”Filter 1” and ”Filter 2”, and the camera beam-path on the bottom.

3.2.1 Imaging and sensing

A CMOS camera, MC050MG-SY, from XIMEA was used for optically imaging both the sample and the NV fluorescence. The camera can be seen in Figure 3.3 as ”Camera”. The properties of the camera is listed in Table 3.3. The camera had an important role in allowing us to do brightfield imaging, to see the sample plane, and giving a visual of the fluorescence and it was critical in the work of minimizing the laser spot size.

Table 3.3: The properties of the XIMEA camera.

Properties	Resolution	Pixel size [µm]	Max Frames per second [fps]
Values	5 MP (2464 x 2056 pixels)	3.45	76

As we needed a more light sensitive detector than the camera to detect the NV blinking, explained in Subsection 2.1.5, a new optical path was introduced. This path can be seen in Figure 3.3 as the path to the left after the ”Flip-up mirror”, ending at the ”Detector”. The ”Detector” was two different photodetectors, first a Photomultiplier Tube (PMT), then later changed to a Si amplified photodetector from Thorlabs. The theory of PMTs was explained in Subsection 2.4.2. The PMT outputs a current, relative to the incident light power, which is measured by the PC through a National Instruments (NI) card, a ”NI PCI-MIO-16E-4 (NI 6040E)”

The PMT used in this Master Thesis was a Hamamatsu H7827-012 PMT. Its spectral response range was from 300 - 850 nm and its frequency bandwidth was from DC - 200 kHz. The frequency bandwidth is the range of frequencies that a device can operate at. The current-to-voltage conversion factor was 0.1 V/µA and its max output was 10 V. At 700 ± 50 nm and 10^5 gain, the PMT had an anode radiant sensitivity of $\sim 0.14 \pm 0.05$ V/nW. 700 ± 50 nm was our spectral range, as we used a 650 nm longpass filter and a 750 nm shortpass filter, and the NVs emit fluorescence in that entire region, as shown in Figure 2.4 [26]. The gain of the PMT could be controlled by a ”control voltage”, a voltage applied to the gain control of the PMT. The recommended control voltage range of the PMT was 0.5 - 1.1 V, which corresponded to a gain of $\sim 1.5 \cdot 10^3 - 4.5 \cdot 10^5$. At the highest control voltage, 1.1V, the anode radiant sensitivity for our fluorescence of 700 ± 50 nm became: 0.6 ± 0.2 V/nW

The lowest detectable power of this PMT was found by measuring the background of the PMT with the lights off at night, over 40 s. The mean, SD and the variance from the measurement was then calculated, shown in Table 3.4. The lowest detectable power was then calculated as when the input power was equal to the SD of the background, 0.0177 mV:

$$P = \frac{0.0177 \text{ mV}}{0.6 \pm 0.2 \text{ V/nW}} = 30 \pm 10 \text{ fW}, \tag{3.1}$$

giving a lowest detectable power of 30 ± 10 fW. The high uncertainty comes from the uncertainty in the responsivity, as the PMT has a logarithmic scale for its responsivity.

The second detector used in this Master Thesis was a photodetector from Thorlabs, a ”PDF10A” Si amplified photodetector with fixed gain. This detector had a much lower frequency bandwidth, DC - 20 Hz, but a much higher gain: $1.0 \cdot 10^{12}$ V/A. The responsivity of the photodetector at 700 ± 50 nm was $\sim 0.48 \pm 0.03$ A/W. To calculate the detector’s output voltage at

specific wavelengths depending on the incident light power, the Equation 3.2 was used.

$$V_{OUT} = P_{OPT} \cdot \Re(\lambda) \cdot G, \tag{3.2}$$

where: V_{OUT} is the output voltage, P_{OPT} is the incident light power, $\Re(\lambda)$ is the responsivity of the detector at wavelength λ, and $G = 1.0 \cdot 10^{12}$ V/A is the gain. For our setup we used $\lambda = 700 \pm 50$, so responsivity became: $\Re(700 \pm 50 \text{ nm}) \approx 0.48 \pm 0.03$ A/W.

The theoretical lowest measurable power of this detector at its most sensitive wavelength, $\sim$ 950 nm, was found through its Noise-Equivalent Power (NEP). The NEP indicates the incoming power, dependent on the frequency, that will have a magnitude in volts equal to the detector's noise, which we will use as this detector's lowest detectable power [70]. The NEP listed by the manufacturer was 1.4 fW/$\sqrt{\text{Hz}}$. This NEP has to be multiplied by the square root of the frequency from the the frequency bandwidth, that is the closest to the frequency used in the measurement. So if 15 Hz was used, the NEP would be multiplied by $\sqrt{15 \text{ Hz}}$, but for any frequency > 20 Hz, the NEP is multiplied by $\sqrt{20 \text{ Hz}}$ instead [70]. So for our measurements, we get:

$$P = 1.4 \text{ fW}/\sqrt{\text{Hz}} \cdot \sqrt{20 \text{ Hz}} = 6.3 \text{ fW}. \tag{3.3}$$

The responsivity of the detector at $\sim$ 950 nm was $\sim$ 0.58 A/W. Comparing this to our responsivity of $\sim 0.48 \pm 0.03$ A/W, increases the lowest detectable power to:

$$P_{Lowest} \approx 6.3 \text{ fW} \frac{0.58 \text{ A/W}}{0.48 \pm 0.03 \text{ A/W}} = 7.6 \pm 0.2 \text{ fW}. \tag{3.4}$$

This is still not the final NEP, unfortunately, as the overall output voltage noise for the detector was higher than listed as well. By the manufacturer the output voltage noise was specified as $\sim$6.5 mV_{RMS}, but from our measurements, the detector used in this Master Thesis was shown to have an overall output voltage noise of $\sim$26 mV_{RMS} instead, $\sim$4 times higher than the specified one. This causes the lowest detectable power of this detector to be $\sim$4 times higher as well: $\sim$ 30.5 $\pm$0.9 fW.

The lowest detectable signal and information of the background of the two sensors are listed in Table 3.4. Both of the detectors end up having almost the same lowest detectable power, but the Si photodetector had a much lower uncertainty in the value. The Si photodetector was also vastly easier to work with and detected a lot less background from the laser than the PMT, which increases the lowest detectable power of the PMT. The SD and variance of the noise from the PMT was, on the other hand, much lower than the SD and the variance of the noise from the Si-Photodetector. As mentioned in Subsection 3.2.1, the PMT also had high incident saturation power, meaning that high power light would ruin the detector, causing it to be harder to work with. Because of this, the Si-Photodetector was used as our main sensor.

Table 3.4: The voltge mean, SD and variance of the background together with the lowest detectable signal of the PMT and the Si amplified photodetector. The lowest detectable signal is calculated as the input power where the voltage will equal the noise.

	PMT	Si amplified photodetector
Background mean [mV]	∼0.19	∼13.2
Background SD [mV]	0.0177	7.47
Background variance [mV]	0.000312	55.7
Lowest detectable power	30±10 fW	30.5±0.9 fW

3.2.2 Laser

The laser used to excite the NVs to generate fluorescence was a 5 mW, 594.0 nm laser. The laser is shown in Figure 3.3 as ”594nm”. It was a laser from Coherent, with the code 31-2230-000. A diffraction limited spot from a 594 nm laser can be calculated from the Rayleigh criteria, Equation 2.7. The diffraction limited spot was therefore calculated to be 259 nm for our laser, meaning that our laser spot should have ideally been as close to 259 nm as possible.

A laser with low power was chosen because the optimal laser intensity in the spot needed to be ∼1 kW/cm^2, as discussed in Subsection 2.1.5. The choice of a wavelength of 594 nm was because this gave an NV^- to NV^0 on-time ratio, r, of $r \approx 0.1$. The laser intensity set to ∼ 1 kW/cm^2 gives an on-time of ∼2 s. These settings give the best settings for detecting NV charge state switching [20].

3.2.3 Mirrors

A dichroic mirror was used to reflect the laser to the objective lens and to let only the NV fluorescence transmit back through the mirror. The dichroic mirror is shown in Figure 3.3 as ”Dichroic mirror”. The mirror was a ”DMLP550” longpass dichroic mirror with a 550 nm cut-on wavelength. According to the mirror’s specifications $> 95\%$ of the fluorescence should be transmitted through the mirror at a 45° angle.

A flip up mirror of polished silver, shown in Figure 3.3 as ”Flip-up mirror”, was placed in the optical path after the optical filters to choose whether to direct the signal to the camera or the detector.

4 silver mirrors were used to route the optical path. These mirrors were not illustrated in Figure 3.3 for simplicity. All 4 mirrors had a reflectance of $\sim 95\%$. One was used to route the laser to the objective lens, before the dichroic mirror, two to route the NV fluorescence to the camera, and a final mirror after the flip-up mirror to route the NV fluorescence to the detector.

3.2.4 Lenses

As getting a small as possible spot was important, an oil immersion objective lens with 100x magnification and highest NA, 1.40, from Olyumpus was used. The object lens is shown

in Figure 3.3 as ”Object lens”. It was an oil immersion lens where the oil had a refractive index of 1.52. The lens fully compensated for both spherical and chromatic aberrations in our region of interest. It had a back aperture diameter of 7 mm.

To obtain the smallest spot size possible, the back aperture of the objective lens needs to be fully illuminated with a parallel beam. Because of this, the beam of our laser had to be expanded, and made as parallel as possible. One way to expand the beam is with a beam expander, which expands the beam through optics inside of it. The other way is to use two lenses, one to focus the beam right in front of it, causing it to diverge quickly afterwards, and then use a second lens afterwards, at the wanted beam-width, to make the beam parallel. This can be seen in the setup diagram shown in Figure 3.3 as ”Lens 1” and ”Lens 2”. ”Lens 1” was a ”C560TME-B” lens from Thorlabs, and had a NA of 0.18 and a focal length of 13.86 mm. ”Lens 2” had a long focal length, $\sim$ 250 mm. A beam expander from Thorlabs, BE02-05-A, was used in place of Lens 1 and Lens 2 at first. The beam expander we used had a magnification of 2x - 5x, where the 5x zoom, gave the smallest laser spot size.

Three lenses were used to focus the NV fluorescence, one to focus the image from the objective lens onto the camera, shown as ”Lens 3”, one to focus the same image onto the pinhole, ”Lens 4”, and one after the pinhole to focus the remaining signal onto the sensor, ”Lens 5” in Figure 3.3. The focusing lens for the camera, ”Lens 3”, was positioned so the top to the bottom of the camera image was 59$\pm$1 µm. The lenses focusing on the pinhole and sensor, ”Lens 4 and 5” were positioned to maximize the NV fluorescence detected by the sensor.

3.2.5 Optical filters

The laser-light reflected from the diamond and the fluorescence from the NVs got filtered by a shortpass and a longpass filter. A shortpass filter reflects back all light above a certain wavelength, the cut-off wavelength, and allows transmission of light below the wavelength. A longpass filter reflects back all light up to a certain wavelength, the cut-on wavelength, and allows transmission of light above the wavelength.

The setup used a shortpass filter with cut-off wavelength 750 nm, ”FEL0750 Longpass Filter” from Thorlabs. The shortpass filter can be seen in Figure 3.3 as ”Filter 1”. The choice of this filter was to cut off as much light as possible after the main fluorescence spectrum of the NV centers, shown in Figure 2.4 [26]. Thereby giving the microscope as much of the light from the NV centers as possible while removing as much background as possible. The longpass filter was of a premium type, where the transmission was more uniform and closer to 100%. The longpass filter can be seen in Figure 3.3 as ”Filter 2”. The initial filter used was a longpass filter with cut-on wavelength of 600 nm, ”FELH0600 Hard-Coated Shortpass Filter” from Thorlabs. This filter was chosen so as much of the NV^0 and NV^- fluorescence spectra would pass through to the PMT and camera. This was so seeing the NVs go from the NV^- state to the NV^0 state was as easy as possible. Further discussion concluded that it would be easier to see the blinking of the NV^-s going to NV^0 if as much of the NV^0 fluorescence spectrum as possible was filtered out. The state change to NV^0 would then cause the signal to go closer to 0, compared to not filtering away the NV^0 spectrum. The longpass filter was then changed to one with a cut-on wavelength of 650 nm, ”FELH0650 Hard-Coated

Shortpass Filter" from Thorlabs.

The Neutral Density (ND) filters were needed in the setup to reduce the power of the laser before the light was focused on the diamond. The ND filters were not shown in Figure 3.3 due to simplicity, but as shown in Figures 3.5 and 3.6, the ND filters were placed between the laser and "Lens 1". ND filters are filters that will reduce the intensity of the transmitted light be reflecting a certain % of it back, dependent on the strength of the filter. The ND filters were used to reduce the power per square centimeter of the focused spot of the laser, which decides the NV^-s' on-time, explained in Subsection 2.1.5. The optimal value for this project was 1 kW/cm^2, which gives an average on-time of 2 s, as explained in Subsection 3.2.2 [20]. To obtain 1 kW/cm^2, we used an ND filter with Optical Density (OD) 0.5, an ND filter with OD 0.2 and a Beamsplitter from Thorlabs, "EPB2 70-30", slightly tilted. This reduced the power of our laser, in the spot, from 440 ± 10 µW to 34 ± 1 µW.

3.2.6 Pinhole

The pinhole can be seen in Figure 3.3 as "Pinhole". To decide on the size of the pinhole to be used in this Master Thesis for the confocal setup, the Airy Unit (AU) of the setup first had to be calculated. By using Equation 2.17 with $\lambda_{em} = 700 \pm 50$, M = 100 and NA = 1.4, AU could be calculated:

$$\text{AU} = \frac{0.61 \cdot 700 \pm 50 \text{ nm} \cdot 100}{1.4} = 30 \pm 2 \text{ µm}. \tag{3.5}$$

With an AU of 30 ± 2 µm, we decided upon using a PH of d = 30 µm. This put us approximately in the 1AU < PH < ∞ range, meaning we could use $A \approx 0.88$ for Equation 2.18 to calculate the FWHM of the axial resolution, and therefore depth, as explained in 2.4.5. Combining Equation 2.15 with Equation 2.18, the width at $1/e^2$ maximum can be calculated, which is approximately equal to the $4\sigma_{axi}$, $2w_{axi} \approx 4\sigma_{axi}$:

$$4\sigma_{axi} \approx 1.7 \text{ FWHM}_{axi} = 1.7 \cdot 0.88 \frac{594 \text{ nm}}{1.52 - \sqrt{1.52^2 - 1.4^2}} = 957 \text{ nm}, \tag{3.6}$$

showing that in our setup we had a depth resolution of approximately 957 nm.

3.2.7 Piezo stages

Three piezo stages, connected to be able to move in the X-, Y- and the Z-direction, were used as the sample-holder. The piezo stages were not shown in Figure 3.3 for simplicity, but is seen in Figure 3.5. The X-, and Y-stages were connected to the PC through a three stage piezo controller, allowing them to be moved for the confocal setup. The instrument used to connect the sensors to the PC only had two analog outputs, so the Z-stage was only operated manually. The stages could move 20 µm with a voltage of 75V applied to them. Using the piezo stages, the sample could move in all three dimensions with sub micrometer precision. An open-loop piezo controller from Thorlabs was used to amplify the voltage from the PC to the piezo stages, with 75 V as its max voltage. 1 V applied to the piezo controller would therefore result in the stages moving 2 µm.

3.2.8 Optically detected magnetic resonance setup

The ODMR setup was not included in Figure 3.3, but the antenna used for the MW radiation can be seen in Figure 3.4. The microwave generator used to perform ODMR was a SynthHD: 10 MHz - 15 GHz Dual Channel Microwave Generator, from Windfreak Technologies. With frequency it had a resolution of 0.1 Hz, and a range of -50 dBm to +20 dBm with a steplength of 0.01 dB. An amplifier from Mini-Circuits, a ”ZRL-3500+” low noise amplifier, was used to boost the MW radiation. It had a range of 700 - 3,500 MHz, with a typical noise figure of 3.2 db and a typical gain of 17 dB at around 2,870 MHz. A small coaxial wire was used as the antenna to direct the MWs right on top of the diamond.

Chapter 4

Description of protocols

This chapter describes the codes used to read out the various signals, and to perform ODMR on NVs. The chapter starts with a MATLAB script, used to calculate the size of the laser spot. Then the two main LabVIEW codes will be explained, the continuous voltage single input code based off of the example LabVIEW code used to measure the signal from the detectors on demand, and the more complex confocal imaging code used to perform confocal imaging on the NVs in our diamond samples. The chapter ends with a short description of the various smaller, less important, but frequently used scrips and codes used in this Master Thesis.

4.1 MATLAB

4.1.1 Laser spot script

The script used to calculate the size of the laser spot was modified from ”Fit 1D and 2D gaussian to noisy data” made by Manuel A. Diaz [71]. The code was modified to calculate the first SD of the spot instead of the FWHM and how it imported the image, sectioning the image to the spot and normalizing it. We used the camera’s software to take the image of the spot needed for this code. A block diagram of the code is shown in Figure 4.1 highlighting what the user needs to input, what the code does and what the code outputs.

The code starts by importing the .png image into an array and then reducing its size by cutting out only the area around the spot. This area needs to be found manually, done the easiest way by simply turning a small area of the array back into an image and see if it is the spot. The code then normalizes the array, subtracting the min-value of the array from the entire array and then dividing the array by its new max value. The code then attempts to make a Gaussian fit of the spot using the initial parameters input.

The code will check if the fit is good using the least squares method shown in Equation 2.23. If the fit is not good: It will change the parameters and make another fit. If the fit is good: It will keep this Gaussian fit and it will create a 3D surface, ”surf”, image of the Gaussian fit together with the spot image in one window. In another window it will show the spot image with a line going through the spot’s center in two perpendicular directions. Above the image, the value of each pixel in the first line is plotted and the same is done for the perpendicular line, shown on the right. This window also shows the calculated σ_X and

σ_Y of the spot, the SD values used to calculate the spot size using Equation 2.16.

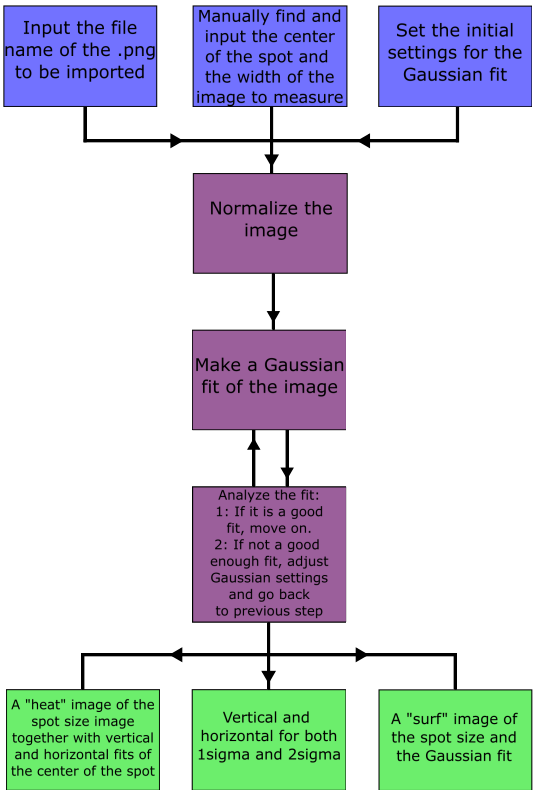

Figure 4.1: Block diagram of the script, ”Laser Spot Script”, for calculating the size of the spot from an image. Blue squares show what the user needs to input, purple squares are the code running and green squares are the outputs of the code shown on the two windows when the code is finished. This code was modified from MATLAB Central File Exchange: ”Fit 1D and 2D gaussian to noisy data” made by Manuel A. Diaz [71].

4.2 LabVIEW

Laboratory Virtual Instrument Engineering Workbench (LabVIEW), is a graphical programming tool focused on data acquisition and processing [72]. Instead of standard programming of writing the code, in LabVIEW, the coding is done by drawing wires between the functions or routines, called a Virtual Instrument (VI). LabVIEW can be split between the front and the back panels, the front panel is what the user sees and interacts with, while all the programming is at the back panel.

4.2.1 Single input program

A LabVIEW program was used to read the signal from the sensor using a National Instruments (NI) card, PCI-MIO-16E-4 (PCI-6040), mounted in the PC. The LabVIEW example program ”Voltage - Continuous Input” and NI-DAQmx were used as the baseline for the data acquisition program. A block diagram of the program is shown in Figure 4.2, highlighting what the user needs to input, what the program does and what the program outputs.

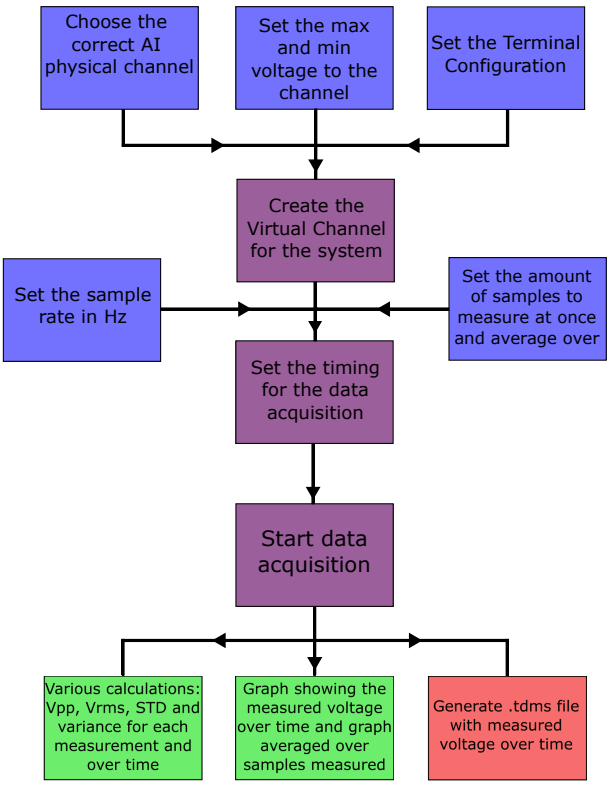

Figure 4.2: Block diagram of the program, ”Single Input”, for continuously measuring samples from the detector using LabVIEW. Blue squares show what the user needs to input, purple squares are the program running, green squares are outputs to the front panel of LabVIEW and red squares are file outputs.

A channel is first created using the *Create Virtual Channel VI*. The max and min voltage is chosen here by the user. The smaller the voltage interval, the higher the resolution. The channel chosen is the channel for the Analog Input (AI) of the NI card that the detector is connected to. This task is next moved to the *Timer VI*, where the mode ”continuous samples” is set, and the frequency and the amount of samples is set from the user’s input. This task is then wired to the *Logging VI* that logs the measured voltages in a .tdms file.

The task is then wired to the *Start VI*. The task is wired into a ”While” loop that will only stop if the ’Stop’ button, on the LabVIEW front panel, is clicked or if an error has occurred. While this loop is running the program will continuously measure samples from the detector and graph them onto the front panel. The program will also do a running calculation of the $V_{P\text{-}P}$, the V_{RMS} , the SD and the variance of the samples until the program stops. After the loop the task is stopped and cleared. Lastly the program will check if any errors occurred.

4.2.2 Confocal imaging program

A LabVIEW program was used for the confocal imaging done in this Master Thesis. The measurements were carried out using the continuous measurement described in Subsection 4.2.1. This section will focus on the analog output section of this code and explain the difference in the input section of this program, compared to the previous program. A block diagram of this program is shown in Figure 4.3, highlighting what the user needs to input,

what the program does and what the program outputs.

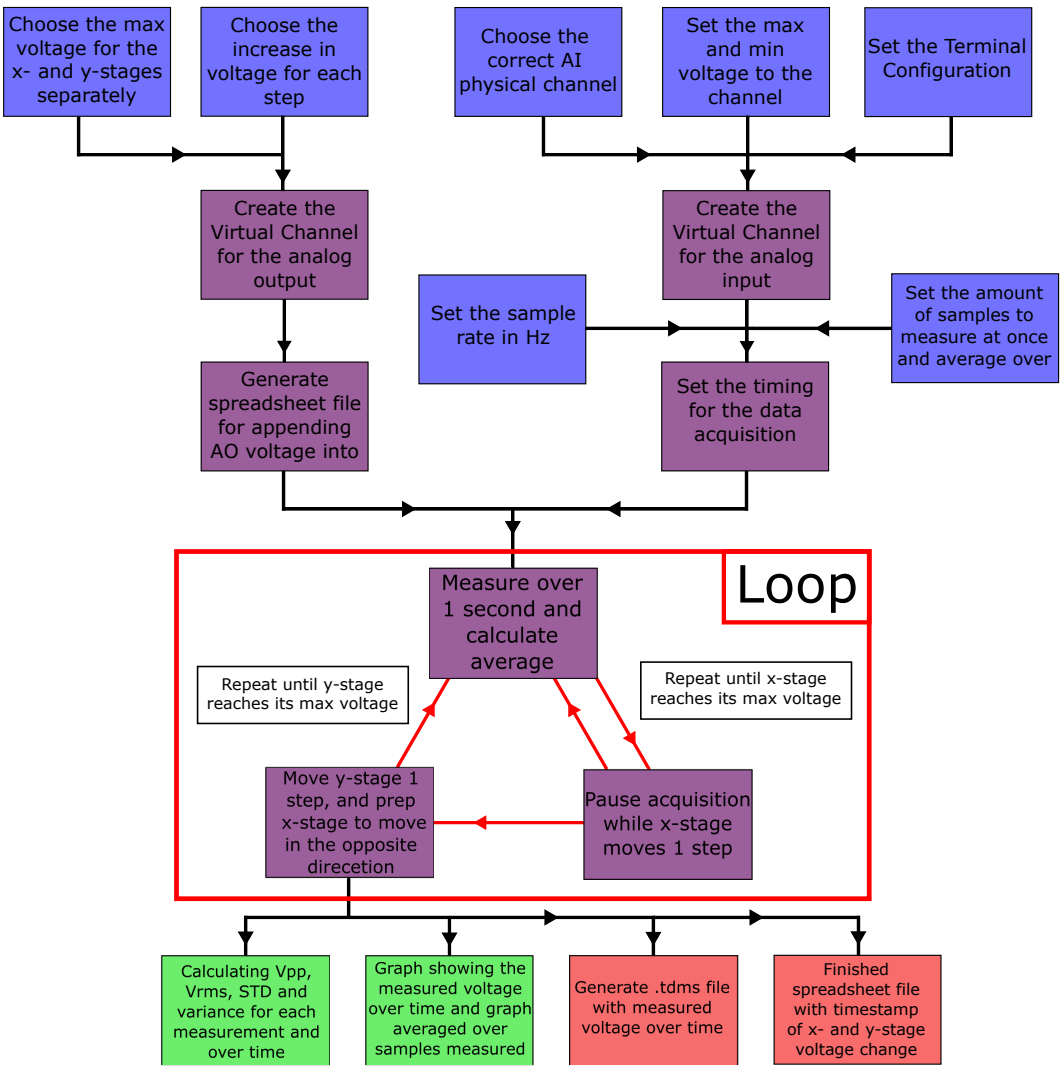

Figure 4.3: Block diagram of the ”Confocal Imaging” program used in this master thesis. Blue squares show what the user needs to input, purple squares are the code running, green squares are outputs to the front panel of LabVIEW and red squares are file outputs. The red arrows show a loop that will run until they are done.

The input and output codes are run parallel until they reach the data acquisition part, and the AI half of this section is identical as in Subsection 4.2.1. A channel is created for the output using the *Create Virtual Channel VI*. Two outputs are used for the X- and Y-stages. Parallel to this, a spreadsheet file is generated with four columns: X-stage voltage, Y-stage voltage, start time and end time. The analog output section is wired to the *Start Task VI* and the analog output, input and the previously generated file's path are all wired into three while loops.

The inner loop runs first, and its job is to measure the voltage of the input. It measures the voltage together with the timestamp of the measurement over a time-period chosen by the input of the user. Then this measured voltage is saved in a matrix indicating which pixel it is. After this while loop has run for its set time, the task is ended as that stops the

acquisition. The task, and the data acquisition, restarts every time the middle loop runs once.

The middle and outer while loops are used to change the voltage of the X- and Y-stages respectively. The X-stage is moved from 0 V to its max voltage in the middle loop before the Y-stage is moved one step in the outer loop. After the X-stage has moved from 0 V to its max voltage, the next iteration of the while loop has the X-stage go from its max voltage to 0 V. With each iteration of the middle while loop, the X-stage voltage, the Y-stage voltage, the loop's start time and the loop's end time are all appended to the previously generated spreadsheet file, to log the change in the stages' voltage. At the end the tasks are ended and cleared, and the matrix with the input voltage of each pixel is written to a spreadsheet. Lastly the code checks for any errors.

4.3 Smaller scripts and programs

Several extra smaller codes were used in this Master Thesis. A MATLAB script was used to calculate an estimate of the FWHM and the width at $1/e^2$ intensity, which will be explained in Subsection 4.3.1. A LabVIEW program building upon the Single Input program from Subsection 4.2.1, for having two inputs, one for the sensor and a laser reference, which will be explained in Subsection 4.3.2. Lastly there was a program for finding the intensity of the camera image over time, which will be explained in Subsection 4.3.3.

4.3.1 FWHM and 1/e^2-width script

The two programs for calculating the FWHM and the width at $1/e^2$ of the maximum intensity functioned identically, apart from at what intensity they calculated the width. The FWHM code will therefore be used as example.

As with the Laser Spot Script explained in Subsection 4.1.1, the first the script did was import the image and then normalizing the image in the same way as in the Laser Spot Script. Following that the script found the pixel, or pixels, in the spot that had the maximum value. Then the script looked at the first pixel in the same row as the pixel with the maximum value that had an intensity above 50% of this maximum value. It then did the same, but with the last pixel with an intensity above 50%. It did this for each pixel that had the maximum value, for both rows and columns and then listed all the calculated widths. The second script simple swapped 50% of the maximum intensity with $1/e^2$ of the maximum intensity. This script was short and simple, but also had a high uncertainty. Therefore it was only used to compare with the spot sizes from the Laser Spot Script, explained in Subsection 4.1.1.

4.3.2 Double input

The LabVIEW program for double input was written nearly identical to the Single Input program from 4.2.1. Because of this only the changes between the two programs will be explained.

Instead of creating a single virtual channel, a channel for both the sensor and the reference each were created. Both of the signals were averaged after a measurement, not only the signal. After a measurement, both the signal and the reference were divided by their first measurement. This was done as a form of normalization, so only the change of intensity was measured. Then the averaged signal was divided with the averaged reference. Lastly all three of these averaged values were plotted together: the signal, the reference and the signal divided by the reference. Because of the initial normalization, all three of these values were within a small distance of each other and could be plotted together.

4.3.3 Camera code

The camera code was used to measure the intensity of the entire image over time. This was done to test if the camera could be used to sense the NV blinking. This code was written in PYTHON and used XIMEA's own PYTHON API to control the camera through the code.

The start of the code opened the camera, so settings could be set. All settings were first set to default to turn off Auto Exposure and Gain (AEG). Then the exposure time and the gain were set to what the user wrote. The Look-Up Table of the camera was set to default, and then the how many pictures the code was to take was set. The camera was then set to ”Open” and then ”Start” to start the data acquisition. While the code was running the camera would save the images either as an array, where the values were the intensities, or as images on your computer. If the images were saved as an array the code would calculate the total intensity of all the pixels of each image and only save that value. If only the averages were saved, the code would graph the average intensities over time. Otherwise the images would have to be imported into MATLAB to calculate the intensities over time.

Chapter 5

Experimental results

This chapter presents the experimental results from this Master Thesis and some calculations of the results. This chapter showcases the various methods used to attempt to detect NV blinking, and shows how the spot needs to be smaller, and a photon counting detector is needed to detect this blinking, but everything else is working. The chapter starts by showing the results from measurements that were necessary to the experiments later on. The first is the FOV of the camera and the size of each picture in the sample plane. Afterwards the results start by showing how the laser spot size was calculated, how it was shown to be 1460±50 nm, and the laser intensities used to obtain a 2 s on-time of the NVs. The approximate NVs in the spot of the two diamonds were also calculated to be ∼2400 for the bright and ∼12 for the dim diamond. After that, this chapter will explain why both the camera and the PMT were both not sensitive enough and too difficult to use, to find NV blinking. Then measurements from the Si amplified photodetector will show why the dim sample with the aluminium coating was the sample used to attempt observing NV blinking, and then two measurements will show that NV blinking could also not be detected with the Si amplified photodetector in our setup. Then the results from the confocal imaging will be shown, where two measurements will show how the confocal code can detect areas of higher intensity fluorescence. Two measurements also show that the laser or detector cause the intensity to decrease over time. Lastly results are shown to prove ODMR can be performed on the setup.

5.1 Camera image size

To measure the final magnification of the camera image, to calculate the laser spot size later, a micrometer ruler for microscopes from Thorlabs, model ”R1L3S2P”, was used. This ruler consists of stripes with a spacing of 10 µm between each, with a full length of 1 mm. By imaging this micrometer in bright-field, the camera’s Field of View (FOV), the maximum height of the camera image, and the size of the image projected onto each pixel can be calculated. Through Figure 5.1, the height of the camera image, and its FOV, was found to be 59±1 µm. With a pixel height of 2056 pixels, the size of the image projected onto each pixel can be calculated:

$$\frac{59 \pm 1\ \mu\text{m}}{2056\ \text{pixels}} = 28.7 \pm 0.5\ \text{nm/pixel}. \tag{5.1}$$

The value calculated in Equation 5.1, 28.7 ± 0.5 nm/pixel, will be used to calculate the laser spot size later, shown in Figure 5.4.

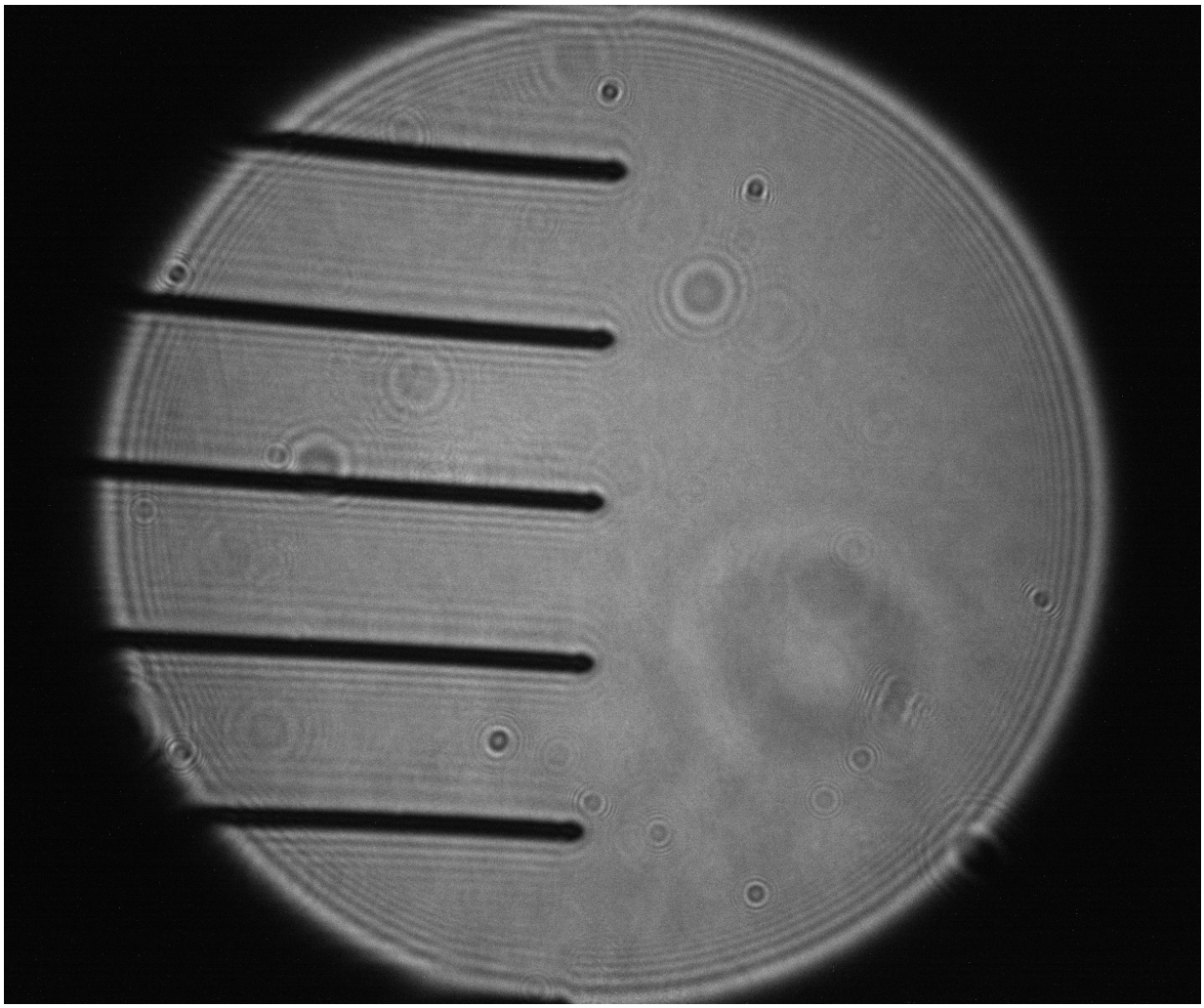

Figure 5.1: The image used to find the FOV of the optical microscope. Almost six 10 µm lines go from the bottom to the top of the image, giving the image a height of 59±1 µm.

5.2 Laser spot size and NVs in spot

An optical power meter from Thorlabs, ”PM100D”, with a photodiode power sensor of ”S121C”, was used to measure the intensity of the laser at the position of the sample. Through this power meter it was measured that the laser intensity fluctuated by ±4%. The power meter was also used to measure the power of the laser right after the objective lens, in the laser spot. This is the measured optical power that is listed for the laser in this Master Thesis, in Table 5.1 for example. The importance of knowing the intensity of the laser for NV blinking is explained in Subsection 2.1.5.

An image of the spot can be seen in Figure 5.2 and a heat image of the same spot in Figure 5.3. This is an image of the smallest spot obtained in this Master Thesis. A heat image showing how the σs in the X- and Y-directions, $\sigma_X = 12.5$ pixels and $\sigma_Y = 12.1$ pixels respectively, from this spot were calculated is shown in Figure 5.4. This figure, together with Figure 5.5, which is a 3D surface image of the spot together with its Gaussian fit, were generated by the Laser Spot Script explained in Section 4.1.1. Using Equation 2.16, this small spot was

calculated to be 1410±50 nm:

$$d_{spot} = 2(12.5 \text{ pixels} + 12.1 \text{ pixels}) \cdot 28.7 \pm 0.5 \text{ nm/pixel} = 1410 \pm 50 \text{ nm}. \tag{5.2}$$

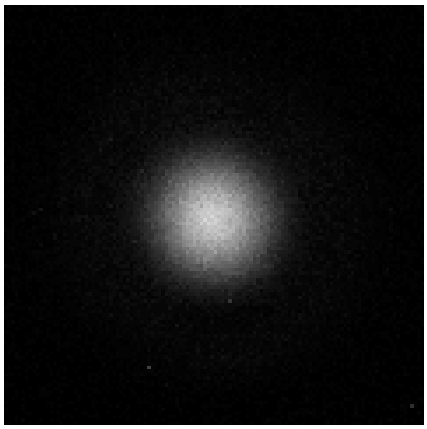

Figure 5.2: A camera image of the spot with the dim sample with aluminium coating.

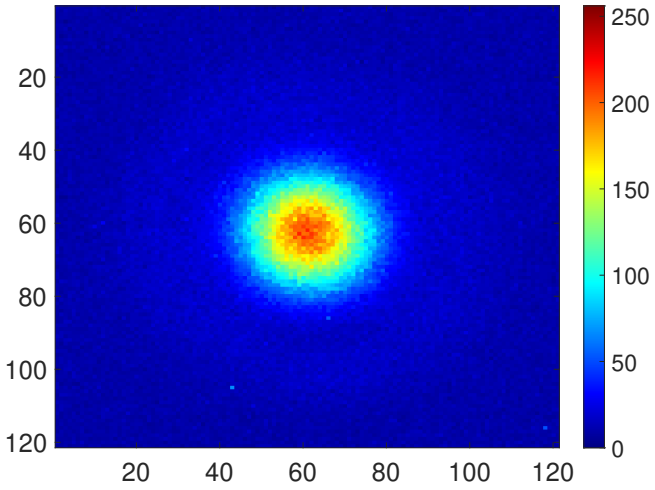

Figure 5.3: A heat image of the spot normalized to max 255 and min 0.

The calculated size of this spot and 3 other measurements are shown in Table 5.1. As the difference in focus between these images were so small, the average of these spots was used as the real spot size, calculated to be 1460±50 nm.

Table 5.1: The spot size calculated from four images of slightly different Z-positions, where all four were within 1 µm of each-other, with the average of the spot sizes at the end.

	σ_X [pixels]	σ_Y [pixels]	Spot size [nm]
1st image	12.7	12.5	1440±50
2nd image	13.3	13.2	1520±50
3rd image	12.9	12.6	1470±50
4th image	12.5	12.1	1410±50
Average	12.8	12.6	1460±50

With the size of the spot as 1460±50 nm and the depth calculation from Equation 3.6, we can calculate the full volume of our spot through Equation 2.19:

$$V = 2\left(\frac{1460 \text{ nm}}{2}\right)^2 957 \text{ nm} = 3.21 \text{ µm}^3. \tag{5.3}$$

The NVs in the spot for each of the samples can then be calculated through the volume calculated as 3.21 µm^3, from Equation 5.3, and Equation 2.1:

$$N_{Bright} \approx 150 \text{ NVs/(µm}^3 \text{ ppb)} \cdot 5 \text{ ppb} \cdot 3.21 \text{ µm}^3 = 2400 \text{ NVs}. \tag{5.4}$$

$$N_{Dim} \approx 150 \text{ NVs/(µm}^3 \text{ ppb)} \cdot 0.025 \text{ ppb} \cdot 3.21 \text{ µm}^3 = 12 \text{ NVs}. \tag{5.5}$$

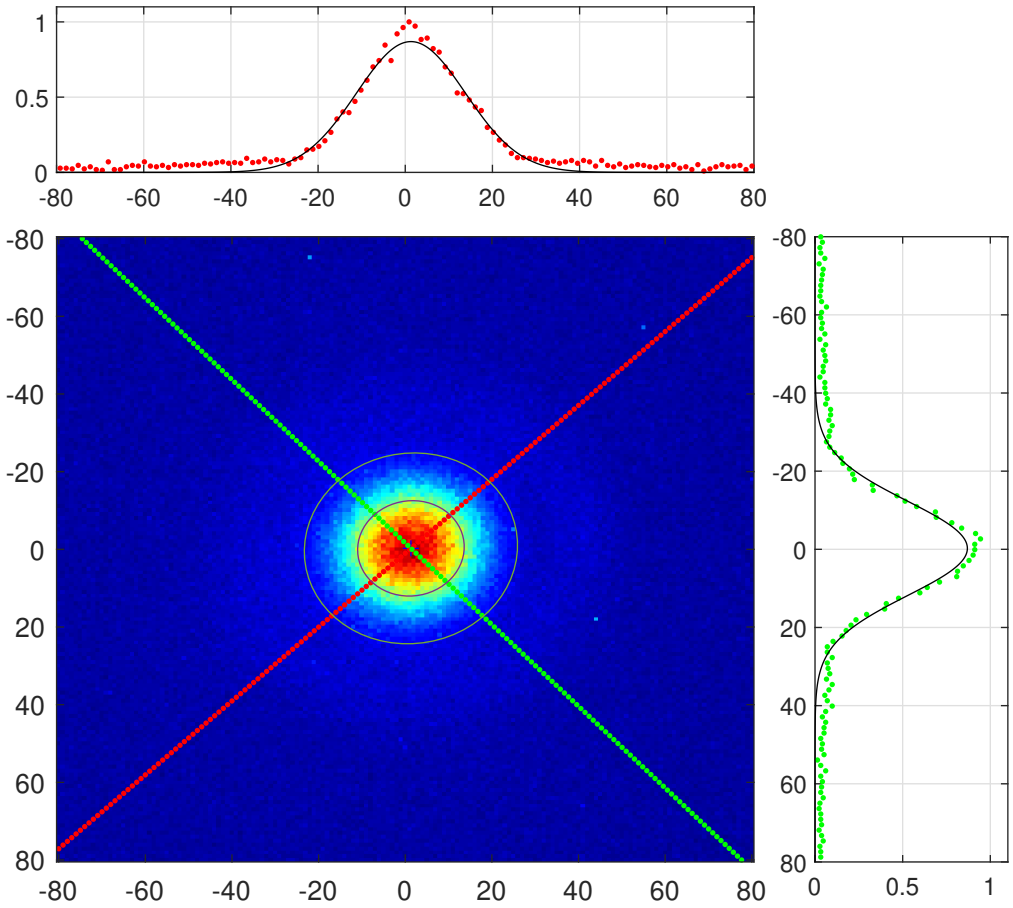

Figure 5.4: The result of the Laser Spot Script, from Subsection 4.1.1, showing the spot in the center together with two circles indicating 1σ and 2σ out from the center. The Gaussian fit in two perpendicular directions is shown, the first above and the second on the right. The SD in the X- and Y-directions were calculated to be: σ_X = 12.5 pixels and σ_Y = 12.1 respectively.

With the bright sample averaging approximately 2400 NVs in the spot, it is immediately obvious that this sample is unfit to detect a single NV blinking, which is necessary to perform STORM. The dim sample however, averages approximately 12 NVs in the spot, which unfortunately is still several NVs, but not too many to make it impossible to detect a single NV blinking. With a 2 s on-time, on average there will be at least one NV on at all times, indicating that detecting a single NV blinking would be easier if the spot was diffraction limited.

The size of the laser spots with the two different laser beam expansion methods, explained in Subsection 3.2.2, are shown in Table 5.2. The table clearly shows that using two lenses to expand the laser is significantly better than using a beam expander. The Table also shows the measured laser power in the spot and the calculated laser intensity in kW/cm^2 for both of the methods. The laser intensity is calculated simply by dividing the spot size the laser

power. The on-times in Table 5.2 were calculated from Equation 2.6, as shown for the 1970 nm spot:

$$\tau_{on}(1970\text{ nm}) \approx \frac{2}{I_L^2} = \frac{2}{(1.07 \pm 0.09\text{ kW/cm}^2)^2} = 1.8 \pm 0.6\text{ s}. \tag{5.6}$$

The uncertainty from the on-time calculations are in the range of ± 0.3 s. This means that the on-burst from the NV$^-$s are not set to a static 2 s, but can be at least from 1.7 - 2.3 s, which needs to be kept in mind when looking for the NV blinking.

Table 5.2: The spot sizes in nm and the laser power used for the two different methods used to expand the laser beam in this Thesis.

	Spot size [nm]	Laser power [µW]	Intensity [kW/cm^2]	On-time [s]
Beam expander	1950±70	65±3	1.07±0.09	1.8±0.3
Two mirrors	1460±50	34±1	1.00±0.07	2.0±0.3

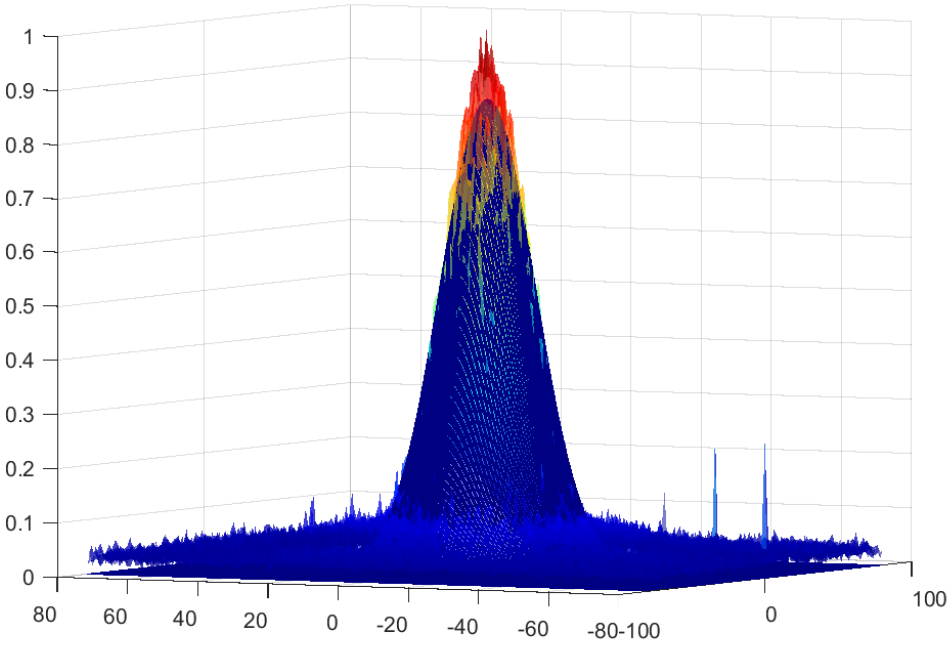

Figure 5.5: A 3D surface image of the spot from 5.4, normalized to Y-axis max 1 and min 0. This is the second figure generated by the Laser Spot Script from Subsection 4.1.1. The Gaussian fit, in blue, is plotted together with the spot, the heat image inside the Gaussian.

5.3 Detecting NV fluorescence and blinking

5.3.1 Camera

A measurement using the camera to try to observe NV blinking is shown in Figure 5.6 and a measurement of the background is shown in Figure 5.7. Figure 5.6 shows a clear decline in the signal from the camera during the first ∼40 measurements. Due to the consistent decrease, it would be impossible to notice the NV blinking in this area, due to their low power shown in Figure 2.5 and the first 40 measurements were therefore not shown in the results in the subsequent tests. This is shown in Figure 5.7, where the graph starts at measurement 40.

The straight lines in Figures 5.6 and 5.7 are measurements where the settings changed mid-measurements, causing them to either go far above or far below the max or min measurements respectively. The straight lines are averages of the entire measurement, excluding the measurements they replaced, to make the measurements at least usable. Unfortunately we did not find out how to fix this problem. Furthermore, the noise in the intensity measurements from the camera was too high to be able to detect the blinking of the NVs. Because of the unstable settings, the varying noise, as shown in the peak around measurement 60 of Figure 5.7, and how time-consuming the measurements with the camera were, work on attempting to measure NV blinking through the camera was discontinued in favour of the more sensitive detectors.

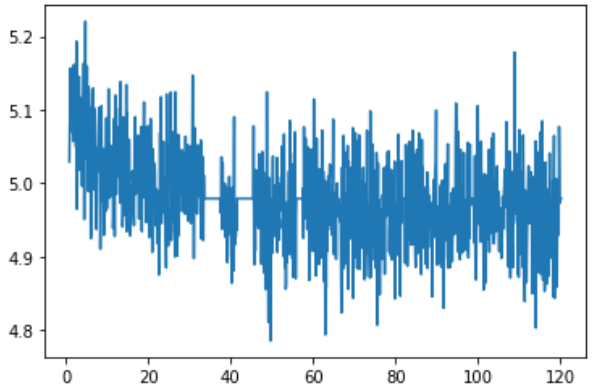

Figure 5.6: 16-bit camera code of NVs with the first 40 measurements. The X-axis is the measurement number and the Y-axis is the summed intensity of all of the pixels in the image in 10^4.

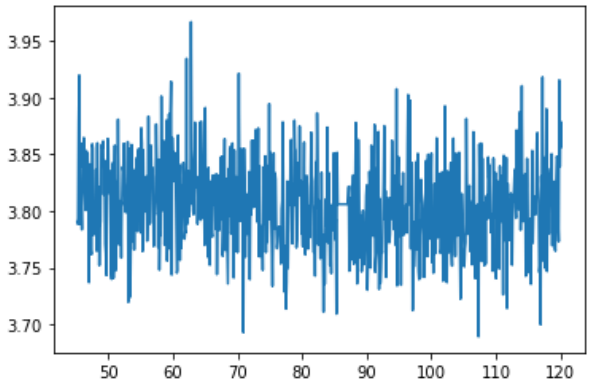

Figure 5.7: Background camera measurement without the first 40 measurements. The X-axis is the measurement number and the Y-axis is the summed intensity of all of the pixels in the image in 10^4.

5.3.2 Photomultiplier tube

The measured average background signal of the PMT was measured to be 0.19±0.02 mV, as shown in Table 3.4. The PMT was the first detector after the camera used to attempt detecting NV blinking. The background signal and noise measurement used to calculate this is shown in Figure 5.8.

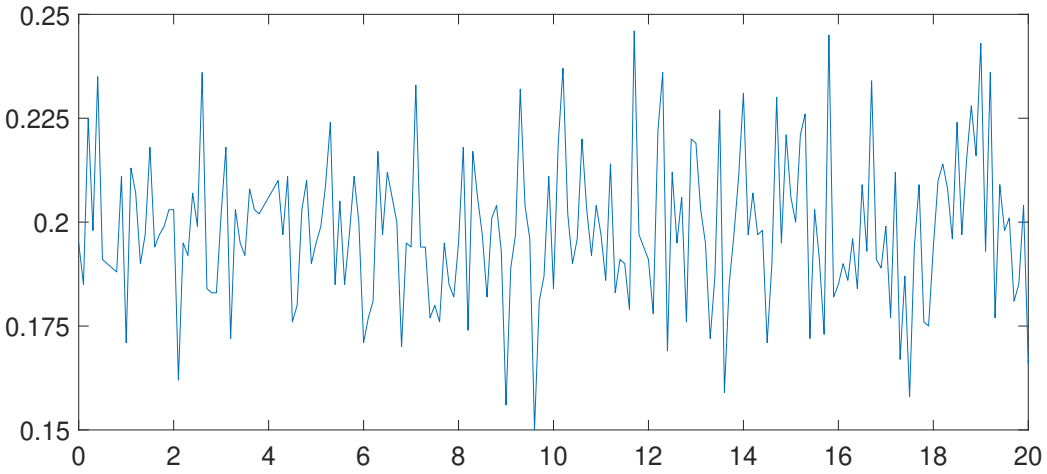

Figure 5.8: Measurement of the background noise from the PMT at night with the lights off.

The difference in signal from background to the signal from the diamond in focus was too small to observe it in the LabVIEW program. This signal could only be found by looking at the laser instead of the fluorescence. This was done by using high ND filters, > 3.0 OD filters, in front of the laser and by removing the shortpass filter, causing the PMT to measure the laser instead of the NV fluorescence. After finding the max value for the laser, the shortpass filter was re-inserted and the ND filters were removed. Any tiny change to the system would cause the signal to become so low that it was impossible to find again. Due to how much work was needed to find the signal from the NVs after every measurement, the Si amplified photodetector was preferred and used as the main detector instead. The PMT had a much bigger detecting area than the Si photodetector, which caused it to measure the background from the laser easily. Therefore the strength of the ND filters would change the measured laser background, and the PMT's noise, causing its noise to be higher than listed in Table 3.4 and be less reliable than the Si photodetector's noise.

5.3.3 Si amplified photodetector

The detector used after the PMT was a Si amplified photodetector listed as a "Femtowatt photoreceiver" from Thorlabs. This meant it had an extremely high sensitivity, being able to detect signals down into the femtowatt range, which is the same order of magnitude as the NV fluorescence, as shown in Figure 2.5 [34]. The noise of the Si photodetector was listed as $\sim$6.5 mV_{RMS} in the datasheet of the detector, as explained in Subsection 3.2.1 . Using an oscilloscope to measure the voltage from the Si photodetector with the detector covered and in darkness, the oscilloscope measured a voltage of $\sim$27 mV_{RMS}. An example of the measurement of the background noise of the Si photodetector used to calculate this mV_{RMS} is shown in Figure 5.9. This increased noise also decreased the sensor's sensitivity by increasing the lowest measurable power from 6.3 fW to 30.5$\pm$0.9 fW. This unfortunately drowned the NV blinking inside of the noise of the detector, as will be demonstrated.

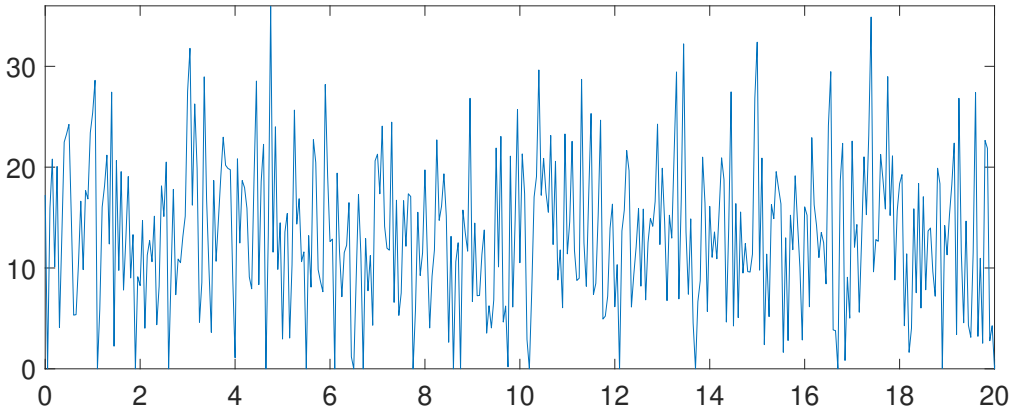

Figure 5.9: Measurement of the background noise from the Si photodetector, where the Y-axis is in mV and the X-axis is in seconds.

The signal from the fluorescence was quite high with the Si photodetector, compared to the background, as can be seen in Table 5.3. The mean background being 13.2 mV and the signal about 886.9 mV without any ND filters. With appropriate filters to have a 2 s on-time, the mean signal was ∼120 mV. The high signal compared to the background most likely came from having a spot with several NV centers in it.

In Figures 5.9 - 5.12 a selection of measurements for the Si photodetector are presented. Figure 5.9 shows a measurement of the background of the photodetector when the laser is on, but with the flip-up mirror down, so the signal goes to the camera, but the background from the laser is still there. The range was set to 0 - 1 V, the rate set to 20 Hz and averaging was turned off. Figure 5.10 shows a measurement of the bright sample with aluminium coating and a second measurement with a 0.5 OD ND filter in front of the laser. Figure 5.11 shows two similar measurements, but with the dim sample and of the area not covered by the aluminium coating. Figure 5.12 also shows two similar measurements, but of the area covered by the aluminium coating. This figure also shows that the sample with the best signal was the dim diamond with the aluminum coating, reaching 800 mV with no ND filters, several times higher than any other measurement.

To attempt detecting NV blinking with the Si photodetector, the dim diamond coated with aluminium was chosen, as explained in the previous paragraph. Two ND filters, a 0.5 OD and a 0.2 OD, and a beamsplitting mirror were placed in front of the laser. The beamsplitting mirror was used as its reflectance was dependent on its angle, and it could therefore be used to finetune to laser intensity after the ND filter. We obtained an on-time of 2 s through this, and the resulting measurement is shown in Figure 5.13. The blue signal from the figure was done as the previous measurements, while the red signal had the sample rate set to 20,000 Hz and the number of samples averaged set to 1,000 samples. Unfortunately, in both of these measurements the noise of the sensor was too high to detect any NVs going from NV^0 to NV^-.

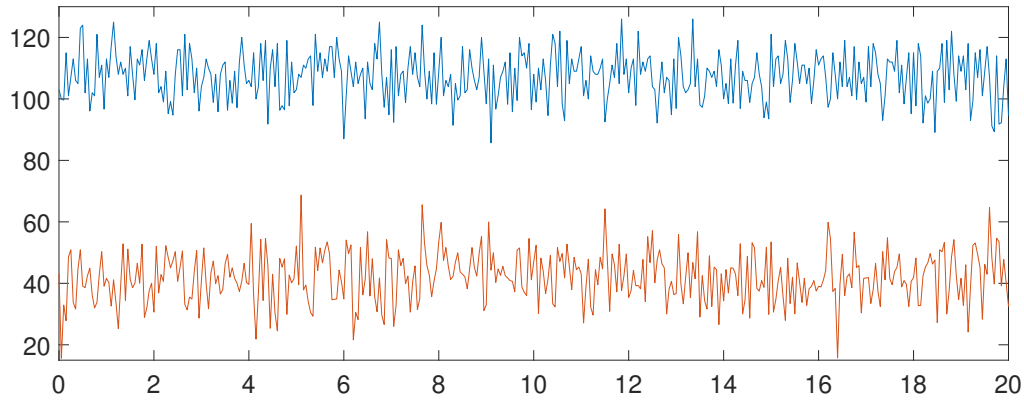

Figure 5.10: Voltage measurements from the bright sample with the photodetector, where the Y-axis is in mV and the X-axis is in seconds. (a) Measurement of the bright sample with the aluminium coating. (b) Added 0.5 OD ND filter after the laser.

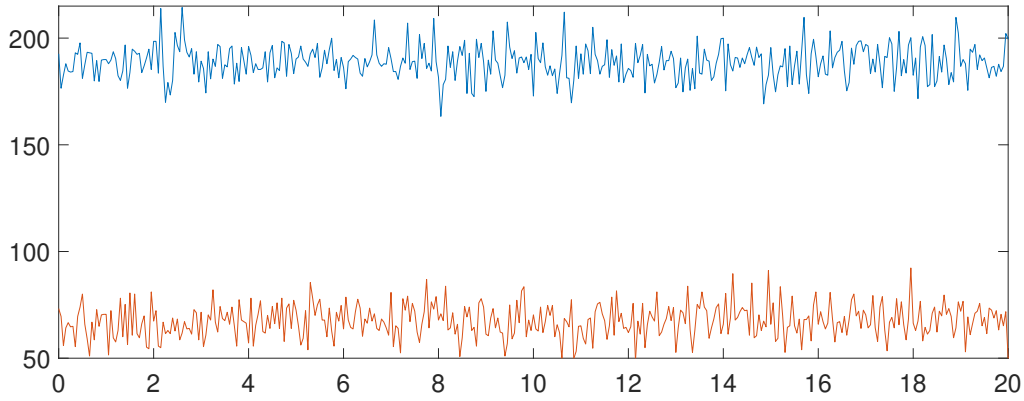

Figure 5.11: Voltage measurements from the dim sample with the photodetector, where the Y-axis is in mV and the X-axis is in seconds. (a) Measurement of the dim sample without the aluminium coating. (b) Added 0.5 OD ND filter after the laser.

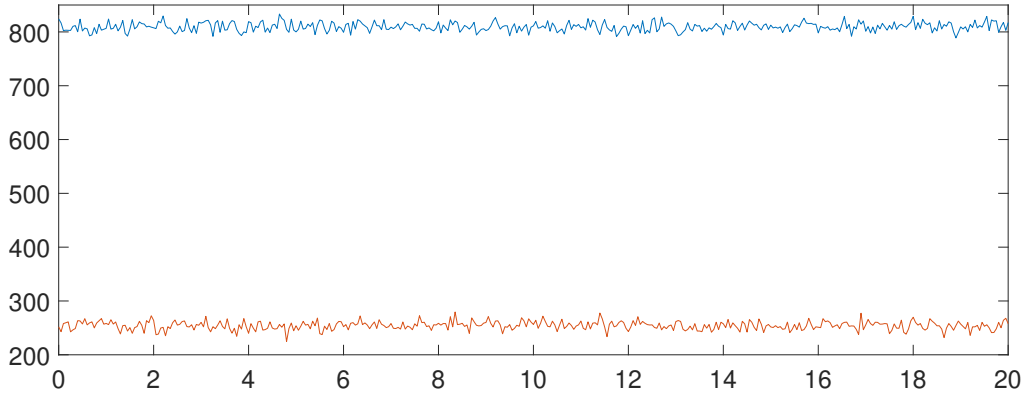

Figure 5.12: Voltage measurements from the dim sample with the photodetector, where the Y-axis is in mV and the X-axis is in seconds. (a) Measurement of the dim sample with the aluminium coating. (b) Added 0.5 OD ND filter after the laser.

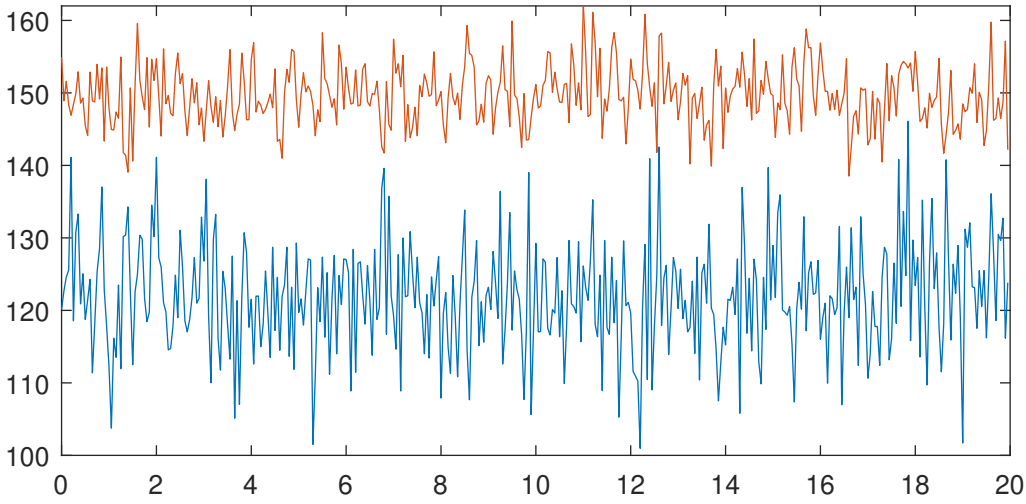

Figure 5.13: Voltage measurements from the dim sample with the photodetector, where the y-axis is in mV and the x-axis is in seconds. The dim sample with the silver coating was used. A 0.5 OD ND filter, a 0.2 OD ND filter and a beamsplitting mirror was used to obtain ∼2s on-time for the NVs. (a) Measurement setting same as previous ones, 20Hz and no averaging. (b) Sample rate set to 20,000 Hz while averaging every 1,000 samples.

Table 5.3: The mean voltage, the SD and the variance of the Si amplified photodetector measurements from Figures 5.9-5.13. All the means are including the background in this table.

Measurement	Mean [mV]	SD [mV]	Variance [mV]
Figure 5.9, Background measurement	13.2	7.47	55.7
Figure 5.10 blue signal, Bright sample with silver coating	107.5	7.80	60.9
Figure 5.10 orange signal, Same as previous, but added 0.5 ND filter	42.5	7.98	63.6
Figure 5.11 blue signal Dim sample without the silver coating	187.6	8.00	64.0
Figure 5.11 orange signal, Same as previous, but added 0.5 ND filter	67.2	7.80	60.9
Figure 5.12 blue signal, Dim sample with the silver coating	810.1	8.25	68.1
Figure 5.12 orange signal, Same as previous, but added 0.5 ND filter	254.4	8.10	65.9
Figure 5.13 blue signal, Measurement with 2 s on time with: dim sample, silver coating, 20 Hz	121.8	7.49	56.1
Figure 5.13 red signal, Same as above, but with: 20 kHz and averaging every 1,000 samples	119.6	4.21	17.8

Table 5.3 shows the mean, the SD and the variance of the measurements shown in Figures 5.9 - 5.13. Both the SD and the variance of the last measurement, with averaging, is lower than the previous measurements, which were mostly similar. The decrease in intensity from adding the 0.5 OD ND filter was ∼61% for the bright sample, ∼64% for the dim sample without the coating and ∼69% for the dim sample with the coating.

As no measurement was able to detect any NVs going from NV^- to NV^0, it was concluded that a more sensitive detector and a smaller spot size was required to detect the blinking. Without the NV blinking, STORM could not be performed and is therefore not shown in this Master Thesis. The next parts will therefore focus on the results from the confocal imaging, and ODMR being performed, demonstrating that the remaining parts to perform STORM with ODMR is in place.

5.4 Confocal imaging

The confocal imaging can be used to probe the sample to detect which areas of the sample have increased or decreased fluorescence, and from there, which areas have a higher or lower density of NVs. One of the reasons we performed confocal imaging was in the hopes of finding a spot with fewer NVs, to make observing the blinking easier.

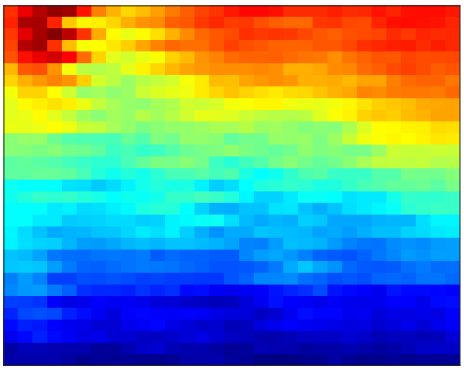

(a)

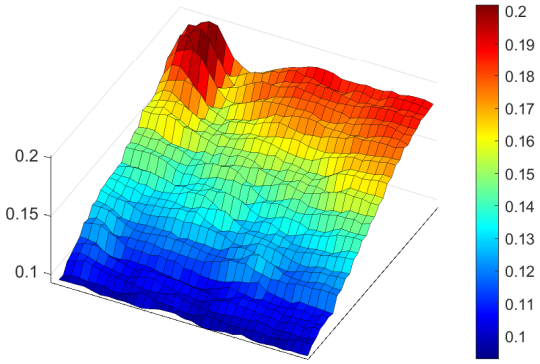

(b)

Figure 5.14: Confocal image of a 2.5x2.5 µm^2 area on the nanodiamond sample. (a) a heat image of the area and (b) a surface image. The intensity is shown in volts.

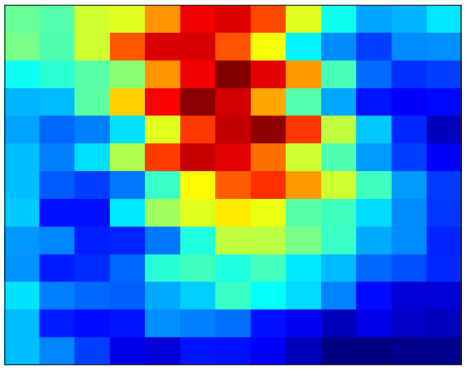

(a)

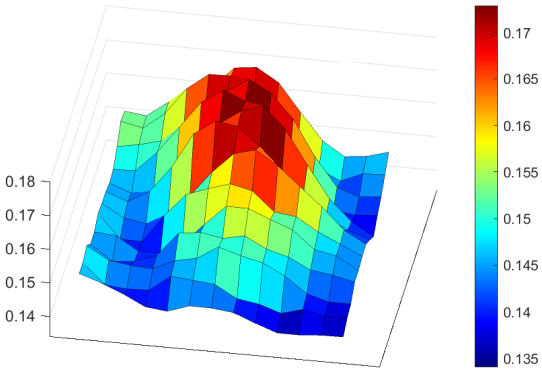

(b)

Figure 5.15: Confocal image of a 1x1 µm^2 area on the nanodiamond sample centered on the peak from Figure 5.14. (a) a heat image of the area and (b) a surface image. The intensity is shown in volts.

An example of a heat image after a confocal scan on a 2.5x2.5 µm^2 area is shown in Figure 5.14a and a 3D surface image of the same image, is shown in Figure 5.14b. This was done on the nanodiamond sample to detect areas with different NV fluorescence. A clear peak in intensity can be seen at the start of Figure 5.14 followed by a decrease around it. The confocal imaging setup is more sensitive to NV fluorescence than the camera. Therefore, if when looking at the camera, going from one area to another area, there is no visual change in the fluorescence intensity, but a change can be seen in the confocal setup, then that indicates

that the area has a higher density of NVs. It is important to check visually with the camera before making a conclusion, as sometimes obstructions, and diffractions from them, can be the reason for the signal change. A close-up of the peak can be seen in Figure 5.15.

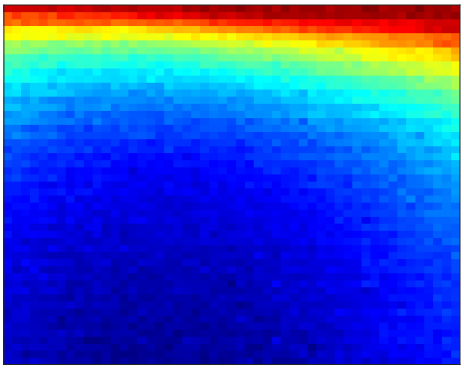

(a)

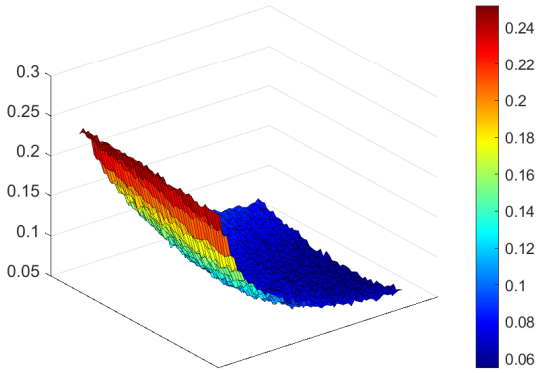

(b)

Figure 5.16: A 5x5 µm^2 confocal image of the intensity of the fluorescence from the Rhodamine sample decreasing over time due to long exposure from the laser. (a) a heat image and (b) a surface image. The intensity is shown in volts.

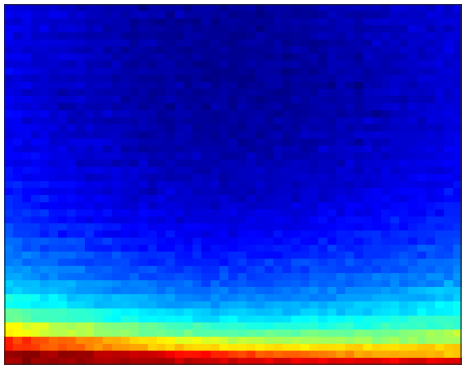

(a)

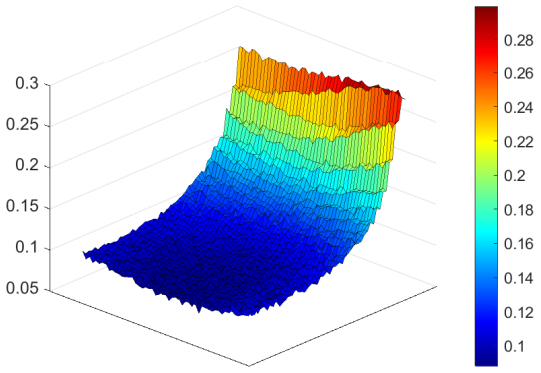

(b)

Figure 5.17: A 5x5 µm^2 confocal image of the intensity of the fluorescence from the Rhodamine sample decreasing over time due to long exposure from the laser, taken in reverse. (a) a heat image and (b) a surface image. The intensity is shown in volts.

There is a clear trend of decreasing intensity from the start to the end of Figure 5.14. This was not caused by the piezo stages moving the sample out of focus, as the initial pixel at 0x0 also had decreased intensity when measured again. The signal decreased over time rather than over distance. This can be seen even clearer from Figures 5.16 and 5.17. The two figures imaged fluorescence from the sample Rhodamine 640 Perchlorate, explained in Subsection 3.1.1, which has fluorescence intensity of several orders of magnitudes higher than NVs. There were two differences between the two figures. One was the position, they measured two different areas, and the second was direction, the second figure, Figure 5.17, was taken in reverse, starting from max voltage, with the piezo stages. The second figure was focused

in the initial pixel of 0x0, where it had an intensity of ~ 0.26 V both proving that the piezo stages were not moving the sample out of focus and that this was not the real shape of the Rhodamine samples. These results were reproducible on any area of the sample.

5.5 Optically detected magnetic resonance of NVs

To demonstrate ODMR, 6 measurements were done using the camera, with different $\boldsymbol{B}$ field strength. The first measurement had no $\boldsymbol{B}$ field, but the subsequent measurements had stronger and stronger $\boldsymbol{B}$ field. The fluorescence spectra of the 6 measurements is shown in Figure 5.18, where each measurement is shifted 0.04 A.U. vertically for visibility. An example of the $\boldsymbol{B}_{\mathrm{NV}}$ calculation using Equation 2.4, is shown:

$$\boldsymbol{B}_{NV} \approx \frac{(2866 \pm 2 - 2874 \pm 2)\ \mathrm{MHz} \cdot h}{2g\mu_B} \approx 0.14 \pm 0.04\mathrm{mT}. \tag{5.7}$$

The frequency peaks, $\nu_{\pm}$, together with the calculated $\boldsymbol{B}_{\mathrm{NV}}$ strength for all 6 measurements is shown in Table 5.4.

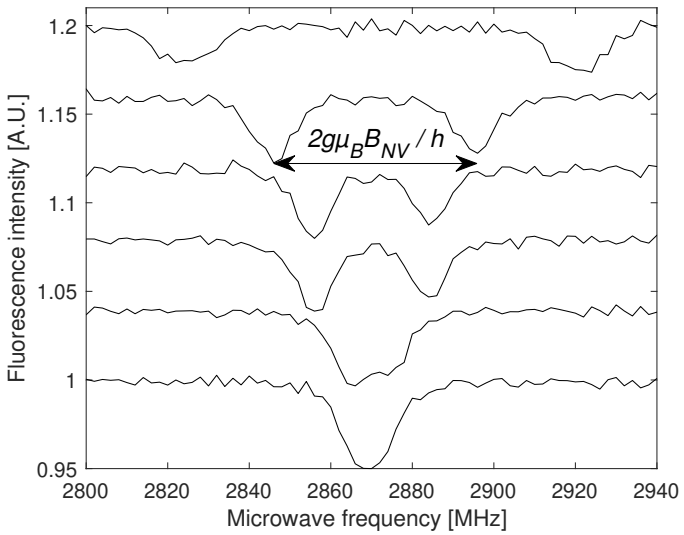

Figure 5.18: 6 measurements of our ODMR setup with different $\boldsymbol{B}$ field strength. Each subsequent measurement's fluorescence has been increased by 0.04 A.U. for visibility.

Table 5.4: The first peak, ν_-, the second peak, ν_+, the interval between them, (ν_+ - ν_-), and the calculated $\boldsymbol{B}_{\mathrm{NV}}$ field from Equation 2.4 from 6 measurements of our ODMR setup with different $\boldsymbol{B}$ field strength, shown in Figure 5.18.

Measurement	ν_- [MHz]	ν_+ [MHz]	(ν_+ - ν_-) [MHz]	Calc. $\boldsymbol{B}_{\mathrm{NV}}$ field [mT]
No field	2870±1	2870±1	0	0
Very weak field	2866±1	2874±1	8±2	0.14±0.04
Weak field	2856±1	2884±1	28±2	0.50±0.04
Medium-weak field	2856±1	2884±1	28±2	0.50±0.04
Medium field	2846±1	2896±1	50±2	0.89±0.04
Strong field	2822 ±1	2920±1	98±2	1.75±0.04

Chapter 6

Discussion of results

This chapter will present the discussion of the results presented in Chapter 5. It will be a discussion on why NV blinking was not detected in this Master Thesis, by comparing our setup to other groups' setups. The chapter will start by discussing the reason for the intensity of the fluorescence from the different samples used in this Master Thesis. Then the results from the camera will be discussed, why the Gaussian fit does not always give an accurate calculation of the spot size, what made the FOV calculations hard to find, and why the camera could not be used to detect NV centers will be explained in detail. Then the difficulties with the laser and the spot will be discussed. The measurements from the PMT and the Si amplified photodetector will be next, explaining why our detectors were not sensitive enough to detect NV blinking. Confocal imaging will be explained as well, the bug in the code will be addressed as well as the decrease in intensity over time and the difficulties of making confocal images. Lastly the ODMR results will be discussed.

6.1 Diamond samples

The bright diamond sample was measured to have a lower voltage with the photodetector compared to the dim sample, even though both had the silver coating above it, shown in Table 5.3. This could be because the bright sample had two different interfaces between the diamond and the coverslip. Only about half of the bright diamond sample was properly glued to the cover slip, while the other half had some air between the diamond and the cover slip. The bright sample also had a spot that was bigger, but slightly dimmer.

The calculated NVs in the spot for the bright and dim sample were $\sim$ 2400 and 12 NVs respectably. To detect a single NV blinking we wanted as few NVs as possible in the spot, so the dim sample was by far the better alternative, as it had an NV density approximately 2000 times lower than the bright diamond. The aluminium coating would not only reflect the NV fluorescence back, but also reflect more of the laser back to the detectors as well, causing the laser to pass through the diamond twice. This could possibly cause the laser to excite more NVs than calculated from the spot or cause the NVs to be radiated by a higher intensity than 2 kW/cm^2, causing their on-time to be lower than 2 s. The calculated spot size both with and without the coating gave similar results, indicating that the coating did not cause more NVs in the image plane to be excited.

6.2 Analysis of camera

6.2.1 The Gaussian fit

To find the diameter of the spot, a Gaussian fit had to be made. This Gaussian fit could either end up being a good fit, or a bad fit, usually dependent on the shape of the spot. For the dim sample, both with and without the coating, the Gaussian fit fit the spot well. For the bright sample, on the other hand, the Gaussian fit only fit well for around the bottom half of the spot, as shown in Figure 6.1. The max of the Gaussian was far below the peak, nearly 30% lower. This would make the $1/e^2$ value of the Gaussian far lower than it should have been, and therefore making the calculated spot size larger than in reality. The dim spot without the coating had a low intensity compared to the bright pixels in the camera, as shown in Figure 6.2. The Gaussian fit is a good fit, but the high single-pixel peaks in the same area as the spot can cause the calculations and the fit to be off. Even so the spot sizes calculated for both with and without the coating for the dim spot were within the uncertainty of each other.

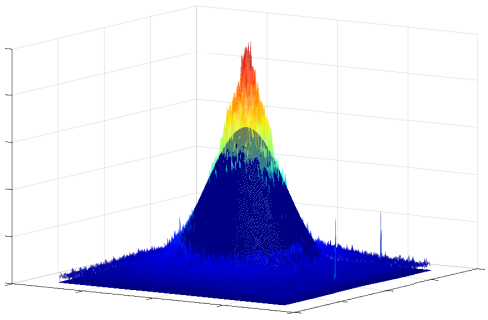

Figure 6.1: A 3D surface image of the bright spot together with the Gaussian fit.

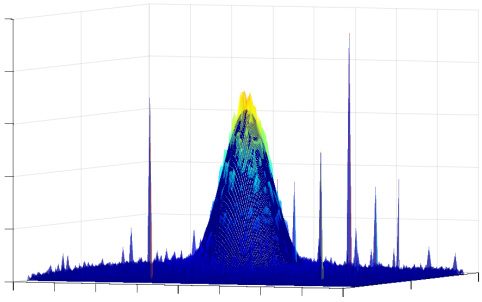

Figure 6.2: A 3D surface image of the dim spot without the coating together with the Gaussian fit.

6.2.2 Camera code

The camera would randomly change its image to be slightly brighter or darker at certain times while taking images, as shown by the straight, averaged lines in Figures 5.6 and 5.7. This slight change in intensity could also be seen when using the camera's application, where the image would go slightly brighter or darker for a short while, often < 1 s, before reverting to normal. All of the camera's settings were chosen manually at that time, with all other automatic settings like gain and exposure, turned off. The cause of this change in intensity is still not known.

The measurements using the camera as shown in Figures 5.6 and 5.7 were done by summing over every pixel in the image, causing the measurements to have high noise. The measurements could have been improved by setting the camera to only take images of the exact position of the spot. The problem with this, however, was that the code would take longer and longer to start the acquisition the smaller the area of the image. When choosing an area that only included the spot, the code would take 10 minutes before it would start

measuring. Together with having to remove the first ∼40 measurements made the camera code spend too much time to do a single measurement that it was simply not feasible to figure out what was causing the change in intensity as explained in the previous paragraph, and so trying to measure NV blinking with the camera was abandoned.

6.3 Analysis of the photodetectors

The sensitivity for both of the detectors used in this Master Thesis were roughly equal, with both detectors having a lowest detectable signal of $\sim$ 30 fW. The PMT had a much higher uncertainty to this value however, with an uncertainty of $\pm$10 fW compared to the Si photodetector with $\pm$0.9 fW. The noise from the Si photodetector was also predictable and would stay close to the mean signal, causing the signal to have a clear change when the detector was detecting a signal. Both the detectors' signals could be averaged, but the PMT's signal was necessary to average to see the signal. Because of this, only the Si photodetector showed a measured signal of "0 V". Because of this, it could be seen when the Si photodetector was measuring a signal lower than its lowest detectable signal, as its lowest measured signal would be higher than 0 V. Whereas this could not be done with the PMT. When measuring the same confocal image with both detectors, it could be seen that the Si photodetector had less noise in its images. These were the reasons why the Si photodetector was chosen over the PMT.

The calculated minimum detectable signal for the Si photodetector was 30.5$\pm$0.9 fW after taking the wavelength from the NVs' emission and the higher measured mV_{RMS} into consideration. Comparing the excitation power of our laser of ∼34 µW to Figure 2.5 [34], gives the NVs a radiant flux of $\sim$ 18$\pm$3 fW, if excited by a 532 nm. This radiant flux is the fluorescence in all directions of the diamond so we can assume that our sensor will see at most 50% of this fluorescence, probably less as this does not take into consideration the fluorescence difference between the NV^0 and NV^-. Our detector therefore needs to have a minimum detectable signal of < 9$\pm$2 fW, which unfortunately is about 3 times lower than for our Si photodetector. This is the main reason why we never saw any NV blinking in this Master Thesis.

Our results could have been better if our photodetector had ∼6.5 mV_{RMS}, as that would give a minimum detectable signal of ∼8.4 fW. Comparing this to < 9$\pm$2 fW, shows that the photodector might have been able to detect NV blinking, though it would have been a challenge. Therefore the detector most likely capable of detecting the difference between NV^- and NV^0 should be a photon counting sensor. Previous research groups [20] also used photon counting sensors and our results could have been better if we had used one instead.

The main advantage the PMT had over the Si photodetector was its sample rate of 200 kHz compared to the Si photodetector's 20 Hz, as they had similar sensitives, as shown in Subsection 3.2.1. With this high sample rate, attempts to do photon counting was done with the PMT. For each measurement, usually 20k samples, the amount of samples that were above a certain threshold, chosen to be slightly above the mean, would be counted and this would be plotted for each measurement. Unfortunately this counting did not lead anywhere as the

PMT's sensitivity was too low and the resulting graph looked nearly identical to the graph averaging the samples. This idea was then also abandoned as a proper photon counting sensor would be required to properly use this technique.

Photon counting was also tried with the photodetector, but unfortunately as the photodetecor's sampling rate was 20 Hz it had far fewer samples to work with, 5 samples at best. This caused the photon counting code to vary wildly between 0 and 5 making it unreliable at showing any kind of result. When doing photon counting at higher samples and sampling rate, the resulting graph was similar to the averaged graph as well, similar to the PMT result.

6.4 Additional challenges for observing NV blinking

There were several smaller, extra challenges involved in observing the NV blinking, that need to be addressed. The next paragraph addresses the ND filters, the second; the uncertainty in the on-time, the third; a possible reflection in our system, and the fourth; the photodetector imaging. All of these made detecting NVs harder and they need to be taken care of before NV blinking can be observed.

Table 5.3 shows a different decrease in signal from the addition of the 0.5 OD, 32% transmittance, ND filter, from the three samples. The bright sample's intensity decreased by $\sim$61% while the dim sample decreased with $\sim$64% without the coating and $\sim$69% with the coating. The ND filters' transmittance is dependent on the incident angle of the light, adding finetuning needed to obtain the appropriate laser power.

Based on calculations, the on-time had an uncertainty of $\pm$0.3 s, or $\pm$15%. This gave a rather high uncertainty on the on-time of the NVs due to how sensitive they are to the intensity of the laser. The laser varying by $\sim \pm$4% at all times even after an hour of heating up causes the on-time to change during the measurements. This made it even harder to find the blinking of the NVs due to the changing on-time.

When expanding the beam using the two mirrors, two spots could be seen in the camera. These two spots could be seen with both diamond samples. After removing all but the necessary objects in the beam path it was clear that the reflection either came from the dichroic mirror or the objective lens. When adding the second lens after the lens used to expand the beam, the two spots could be seen moving towards each other. The two spots ended up being in the exact same position in the camera at the same time as the laser was parallel after the second lens. This became the main way to align the second mirror in the end. Due to this, however, there is a chance that there is a reflection in the setup, reducing the quality of our measurements.

The alignment of the sensor after the pinhole only took the intensity of the signal into consideration. It is therefore not known if the sensor is in fact looking at the spot while it is in focus and not when it is somewhat out of focus. This was brought to attention as the camera and sensor use different heights for the Z-stage for when they are in focus and have the highest signal respectively. The intensity of the fluorescence should be dependent on the amount of

NVs that are illuminated by the laser, and it is therefore a possibility that the detector could be receiving signal from more NVs than estimated from the camera. It seems unlikely, however, that the sensor is not looking at the spot in focus. Unfortunately the camera cannot be used to image this as the entire image is focused onto a spot on the photodetector.

6.5 Confocal imaging discussion

The confocal program in this Mater Thesis functions well, is quite flexible and takes good images, as shown in Figures 5.14a and 5.15a. The only issue with the confocal imaging was that there was a slight problem with the the rows. All the odd-numbered rows had their measured value moved one X-value higher, one pixel to the right, while all the even-numbered rows had their measured value moved one X-value lower, one pixel to the left. This can be seen in Figures 5.14 and 5.15, as the intensity peak from the NVs is going left and right on the X-axis, when it should be a straight line. This problem can be fixed in post-processing, however, with the loss of the values from the leftmost and rightmost columns.

Due to the long averaging time it took over an hour to capture a confocal image of 5x5 μm^2. This causes one image to take over one hour to make. The problem with spending a long time imaging, is that sometimes the intensity of the fluorescence can change over time, or the sample can move out of focus due to drift of temperature variations. As an example illustrating this particularly well, see Figures 5.16 and 5.17. The reason for the change in intensity of the fluorescence over time is not known as it can either be the intensity of the laser reducing over time or the sensitivity of the sensor reducing over time. For the NVs, the decrease in signal could be from heating of the sample from the laser. The NVs are not only sensitive to magnetic fields, but also to temperature [9]. This is however unlikely to be the cause of the massive decrease in signal showed in Figures 5.16 and 5.17. For the those two figures, with the Rhodamine sample, the signal of the Photodetector could be seen decreasing by the second if there were no ND filters between the laser and the sample. By placing higher OD ND filters in front of the laser, the decrease in intensity became slower. The two figures used the highest filter, 2.0 OD, that could be used while still detecting the signal from the Rhodamine. By moving the sample to a new area, the intensity would immediately go back to its initial intensity and then start decreasing again, indicating that the laser is the reason for the decrease in signal over time.

The diamond-crystal samples were hard to get proper confocal images of as they had small particles covering the fluorescent ones, making the confocal images of them look like we were falsely finding clear fluorescent crystals, when in reality, as could be seen by the camera, there was just something in the way stopping the fluorescence. Because of this we decided to change the samples used to prove the confocal imaging worked to test again.

The Rhodamine sample, confocal image shown in Figures 5.16 and 5.17, had an easier structure for performing confocal imaging, but as is clear by the Figures, it had a high decrease in fluorescence over time. This could be because of bleaching of the sample [73]. Whether the Rhodamine sample is being photobleached or not can be checked by imaging the same area again after turning off the laser for some time. On the other hand, Rhodamine's fluorescence

intensity was several orders of magnitude higher than the diamond with the coating with the same laser power, even though neither the laser nor the filters were optimal for Rhodamine, as can be seen from Figure 3.2 [68]. Confocal imaging is therefore possible with this setup, but a trial run should be ran beforehand, to make sure the intensity will not decrease over time.

6.6 Analysis of the ODMR measurements

The results from the ODMR measurements, shown in Table 5.4, show that the $\boldsymbol{B}_{NV}$ field can be estimated from the width between the two intensity minima, as shown in Equation 5.7. The results from the ”Weak field” and the ”Medium-weak field”, shown in Table 5.4 and as the two middle graphs in Figure 5.18, give a similar value of the $\boldsymbol{B}_{NV}$, $\sim$0.50$\pm$0.04 mT. The graphs are also visually right next to one another, but they were done as two separate measurements. The uncertainties could put them as having different $\boldsymbol{B}$ field during the measurement, but it could be that the measurement was done on the same $\boldsymbol{B}$ field. When the $\boldsymbol{B}$ field is extremely low, $\boldsymbol{B}_{NV} \approx 0.14\pm0.04$ mT, the magnetic resonance peaks blends into one another, as shown in the 2nd to bottom graph in Figure 5.18. Due to resolution on the MW radiation however, it is still possible to differentiate the peaks at this $\boldsymbol{B}$ field strength.

Chapter 7

Conclusion

7.1 Conclusion

The objective of this Master Thesis was to build an optical Quantum Diamond Microscope (QDM) capable of taking sub-diffraction-limited confocal images as well as reconstructing a sample's magnetic field. The setup of this QDM has nearly been finished with the camera, the confocal setup, the laser and the sample all being ready. The coding has also been written and is ready, as can be seen by Figures 5.14 and 5.15. ODMR has also been performed, as shown in Figure 5.18.

A lot of options have been investigated to accomplish observing a single NV blinking. The spot has been focused down to a $\sim$1460 nm spot, severely decreasing the amount of NVs in the spot.

Several sensors including the camera, a PMT and a Si amplified photodetector have been implemented and tested to try to detect the NV blinking. Unfortunately all detectors investigated have been proven to not be sensitive enough to be able to detect NV blinking.

All of the programs have been prepared for obtaining sub-diffraction-limited confocal imaging, apart from the post-processing needed for STORM to distinguish single NVs.

7.2 Further work

The first thing that needs further work, is that the laser spot needs to be focused to a diffraction-limited spot, $\sim$ 259 nm, explained in Subsection 3.2.2. This project needs the minimum amount of NVs possible in the spot, to be able to detect a single NV blinking. Matthias Pfender et.al. [20] had a spot of $\sim$ 600 nm, so that size should be aimed for first.

Changing the detector to a photon counting sensor to detect NV blinking is the second thing that has to be done. Buying a photon counter with high sensitivity. Set up the photon counter, change the code to accommodate the photon counter and then make sure the laser intensity is correct for the NVs to have a 2 s on-time. Single NV blinking should then be possible to be measured with the setup.

After a single NV has been measured turning on and then off again, measurements of known samples will be next, to prove the setup is correct and works. After those measurements, the measuring of unknown magnetic samples can begin. 2D nanomagnets' magnetic field can then be imaged and reconstructed.

Appendix A

MATLAB script

The main MATLAB script used in this Master Thesis was the Laser Spot Script from Subsection 4.1.1, modified from ”Fit 1D and 2D gaussian to noisy data” made by Manuel A. Diaz [71]. A block diagram for the code is shown in Figure 4.1. The script is shown starting next page, where the output from the code is two images shown in Figures 5.4 and 5.5 from Experimental Results, Chapter 5.

Contents

- —Fitting Functions—
- ————————
- —Open CMOS image—
- Isolate the spot
- ——Parameters——
- —Build numerical Grids—
- —Fit—
- —Plot Data—


```
clear all; % memory
close all; % windows
```

—Fitting Functions—

Coeficients A convention:

```
% A = [Amplitude, x0, x-Width, y0, y-Width, Angle(in Radians)]
%
% X-data convention:
% X is of size(n,n,2) where
% X(:,:,1) : x-coordinates,
% X(:,:,2) : y-coordinates.
```

```
% 1. 2D Gaussian function ( A requires 5 coefs ).
g = @(A,X) A(1)*exp( -((X(:,:,1)-A(2)).^2/(2*A(3)^2) + (X(:,:,2)-A(4)).^2/(2*A(5)^2)) );

% 2. 2D Rotated Gaussian function ( A requires 6 coefs ).
f = @(A,X) A(1)*exp( -(...
    ( X(:,:,1)*cos(A(6))-X(:,:,2)*sin(A(6)) - A(2)*cos(A(6))+A(4)*sin(A(6)) ).^2/(2*A(3)^2) + ...
    ( X(:,:,1)*sin(A(6))+X(:,:,2)*cos(A(6)) - A(2)*sin(A(6))-A(4)*cos(A(6)) ).^2/(2*A(5)^2) ) );
```

—Open CMOS image—

```
%fileName = '2870.000000.bin';
%fp=fopen(fileName);
%data=fread(fp,2,'int');
fileName = 'img00028.png';
data = importdata(fileName);

% data = double(dataInit) - min(double(dataInit(:)));
% data = data ./ max(data(:));
```

Isolate the spot

```
middle = [940, 805];
% 68 x 70 are the max values for 1180, 960 middle.
% maxWidth = (a lot), minWidth = 1112
% maxHeight = 1030, minHeight = 840
widthVariable = 80;
heightVariable = 80;
indexWidth = (middle(1) - widthVariable : middle(1) + widthVariable);
indexHeight = (middle(2) - heightVariable : middle(2) + heightVariable);

width = length(indexWidth);
height = length(indexHeight);


imageOutInit = data(indexHeight,indexWidth);
imageOut = double(imageOutInit) - min(double(imageOutInit(:)));
imageOut = imageOut ./ max(imageOut(:));
% imageOut = reshape(B,[width, height]);
imageOut = imrotate(imageOut,90);
I = imageOut;
S =  double(I);
```

——Parameters——

```
eta = 0.087;                  % laser eff.
powerDensity = 0.2;           % mW/um2 (10 kW/cm2 -> 0.1, 3 kW/cm2 -> 0.03)
binning = 4;                  % CMOS binning
pxPerum = 1/0.0287;           % pixels/um
n = width-1; m = height-1;    % n x m pixels area/data matrix
A0 = [1,0,12,0,12,0];         % Inital (guess) parameters
InterpMethod='nearest';       % 'nearest','linear','spline','cubic'
FitOrientation='fit';       % 'fit': fit for orientation, 'dont' fit for orientation
```

—Build numerical Grids—

Numerical Grid

```
[x,y]=meshgrid(-n/2:n/2,-m/2:m/2);
X=zeros(m+1,n+1,2);
X(:,:,1)=x; X(:,:,2)=y;
% High Resolution Grid
h=3; [xh,yh]=meshgrid(-n/2:1/h:n/2,-m/2:1/h:m/2);
Xh=zeros(h*m+1,h*n+1,2);
Xh(:,:,1)=xh; Xh(:,:,2)=yh;
```

—Fit—

Define lower and upper bounds [Amp,xo,wx,yo,wy,fi]

```
lb = [0,-n/2,0,-n/2,0,0];
ub = [realmax('double'),n/2,(n/2)^2,n/2,(n/2)^2,pi/4];

switch FitOrientation
    case 'dont', [A,resnorm,res,flag,output] = lsqcurvefit(g,A0(1:5),X,S,lb(1:5),ub(1:5));
    case 'fit',  [A,resnorm,res,flag,output] = lsqcurvefit(f,A0,X,S,lb,ub);
    otherwise, error('invalid entry');
end
disp(output); % display summary of LSQ algorithm

% Calculate laser power requirements
w_x = A(3)/pxPerum;
w_y = A(5)/pxPerum;
S_spot = pi*w_x*w_y*1*1*binning*binning;  % 1sigma radius
tot_laser_power = powerDensity*S_spot/eta;
```

```
Local minimum possible.

lsqcurvefit stopped because the final change in the sum of squares relative to
its initial value is less than the value of the function tolerance.

    firstorderopt: 4.6318
       iterations: 6
        funcCount: 49
     cgiterations: 0
        algorithm: 'trust-region-reflective'
         stepsize: 0.0014
          message: '
Local minimum possible.

lsqcurvefit stopped because the final change in the sum of squares relative to
its initial value is less than the value of the function tolerance.

<stopping criteria details>

Optimization stopped because the relative sum of squares (r) is changing
by less than options.FunctionTolerance = 1.000000e-06.

'
```

—Plot Data—

Plot 3D Data and Fitted curve

```
hf1=figure(1); set(hf1,'Position',[1000 200 700 400]);
switch FitOrientation
    case 'dont', C=del2(g(A,Xh)); mesh(xh,yh,g(A,Xh),C); hold on
    case 'fit',  C=del2(f(A,Xh)); mesh(xh,yh,f(A,Xh),C); hold on
end
surface(x,y,S,'EdgeColor','none'); alpha(0.5);
colormap('jet'); view(-60,20); grid on; hold off

% Plot sample pixels data
hf2=figure(2); set(hf2,'Position',[20 20 800 740]);
subplot(4,4,[5,6,7,9,10,11,13,14,15]); imagesc(x(1,:),y(:,1),S);
colormap('jet');

% Output and compare data and fitted function coefs
text(-n/2-5,m/2+20.0,
    sprintf('\t Amplitude \t X-Coord \t SigmaX \t Y-Coord \t SigmaY \t Angle'),'Color','black');
text(-n/2-5,m/2+25.0,
    sprintf('\t %1.3f \t %1.3f \t %1.3f \t %1.3f \t %1.3f \t %1.3f',A),'Color','red');


% Plot vertical and horizontal axis
vx_h=x(1,:); vy_v=y(:,1);
switch FitOrientation
    case 'fit', M=-tan(A(6));
        % generate points along _horizontal & _vertical axis
        vy_h=M*(vx_h-A(2))+A(4); hPoints = interp2(x,y,S,vx_h,vy_h,InterpMethod);
        vx_v=M*(A(4)-vy_v)+A(2); vPoints = interp2(x,y,S,vx_v,vy_v,InterpMethod);
    case 'dont', A(6)=0;
        % generate points along _horizontal & _vertical axis
        vy_h=A(4)*ones(size(vx_h)); hPoints = interp2(x,y,S,vx_h,vy_h,InterpMethod);
        vx_v=A(2)*ones(size(vy_v)); vPoints = interp2(x,y,S,vx_v,vy_v,InterpMethod);
end

% plot lines
hold on; plot(A(2),A(4),'+b',vx_h,vy_h,'.r',vx_v,vy_v,'.g'); hold off;

% Plot elipse
hold on;
cx = A(2);
cy = A(4);
a= A(3);
b= A(5);
angle = A(6);
%angle=angle/180*pi;
r=0:0.1:2*pi+0.1;
p=[(a*cos(r))' (b*sin(r))'];
alpha=[cos(angle) -sin(angle)
       sin(angle) cos(angle)];
p1=p*alpha;
plot(cx+p1(:,1),cy+p1(:,2));
hold off;

hold on;
cx = A(2);
cy = A(4);
a= 2*A(3);
b= 2*A(5);
angle = A(6);
%angle=angle/180*pi;
r=0:0.1:2*pi+0.1;
p=[(a*cos(r))' (b*sin(r))'];
alpha=[cos(angle) -sin(angle)
       sin(angle) cos(angle)];
p1=p*alpha;
plot(cx+p1(:,1),cy+p1(:,2));
hold off;
```

```
% Plot cross sections
dmin=1.1*min(S(:)); xfit=xh(1,:); hfit=A(1)*exp(-(xfit-A(2)).^2/(2*A(3)^2));
dmax=1.1*max(S(:)); yfit=yh(:,1); vfit=A(1)*exp(-(yfit-A(4)).^2/(2*A(5)^2));
subplot(4,4,[1,2,3]); xposh = (vx_h-A(2))/cos(A(6))+A(2);
plot(xposh,hPoints,'r.',xfit,hfit,'black'); grid on; axis([-n/2,n/2,dmin,dmax]);
subplot(4,4,[8,12,16]); xposv = (vy_v-A(4))/cos(A(6))+A(4);
plot(vPoints,xposv,'g.',vfit,yfit,'black'); grid on; axis([dmin,dmax,-m/2,m/2]);
set(gca,'YDir','reverse');

disp(S_spot);
disp(w_x);
disp(w_y);


    6.2572

    0.3586

    0.3472
```

Appendix B

LabVIEW programs

The Front and Back panels of the main LabVIEW programs used in this Master Thesis are shown in this section. Single Input explained in Subsection 4.2.1 is shown in Section B.1 as Figures B.1 and B.2. Confocal Imaging explained in Subsection 4.2.2 is shown in Section B.2 as Figures B.3 and B.4. The numbered squares on the left in the back panels of Figures B.2 and B.4 show the ”False” cases of the corresponding case structures. The left, or initial, section of the back panel of the Confocal Imaging code is omitted. The *Channel VI* and *Timing VI* were added in for visual reasons in Figure B.4. This is because the beginning through the ”Logging Settings” of the Single Input code is identical to the initial section of the Confocal Imaging code. The initial section of the Confocal Imaging code is therefore shown in Figure B.2.

B.1 Single input panels

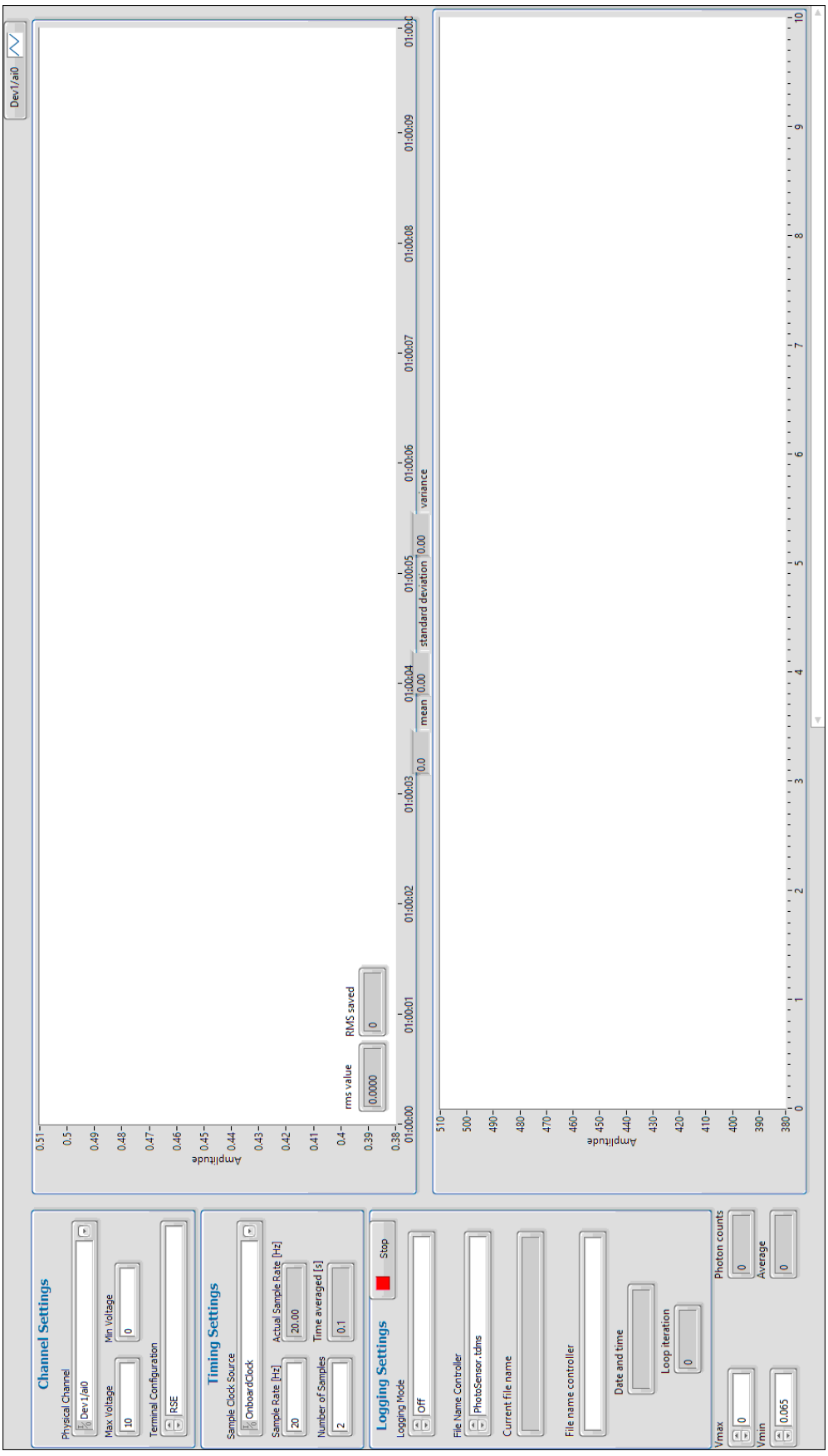

Figure B.1: The front panel of the Single Input LabVIEW code.

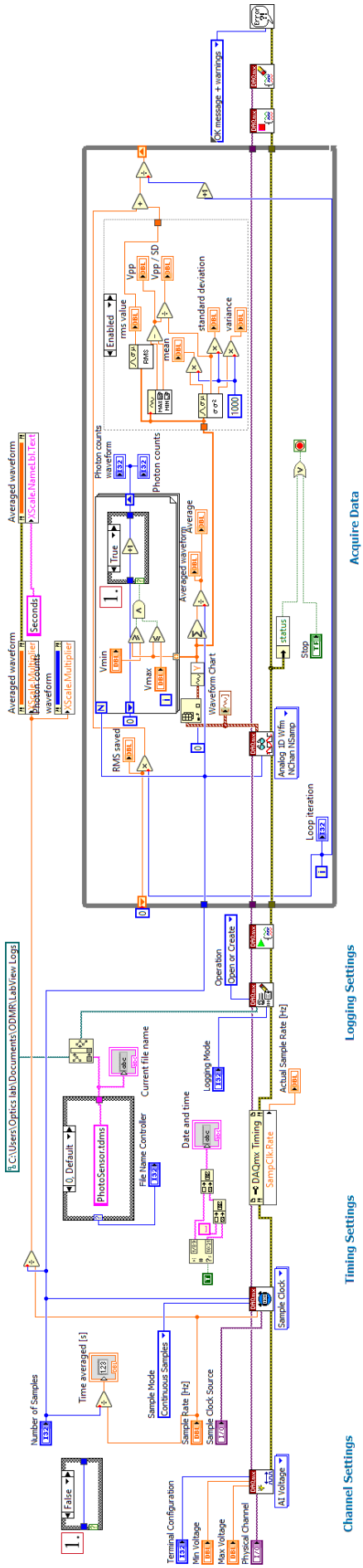

Figure B.2: The back panel of the Single Input LabVIEW code.

B.2 Confocal imaging panels

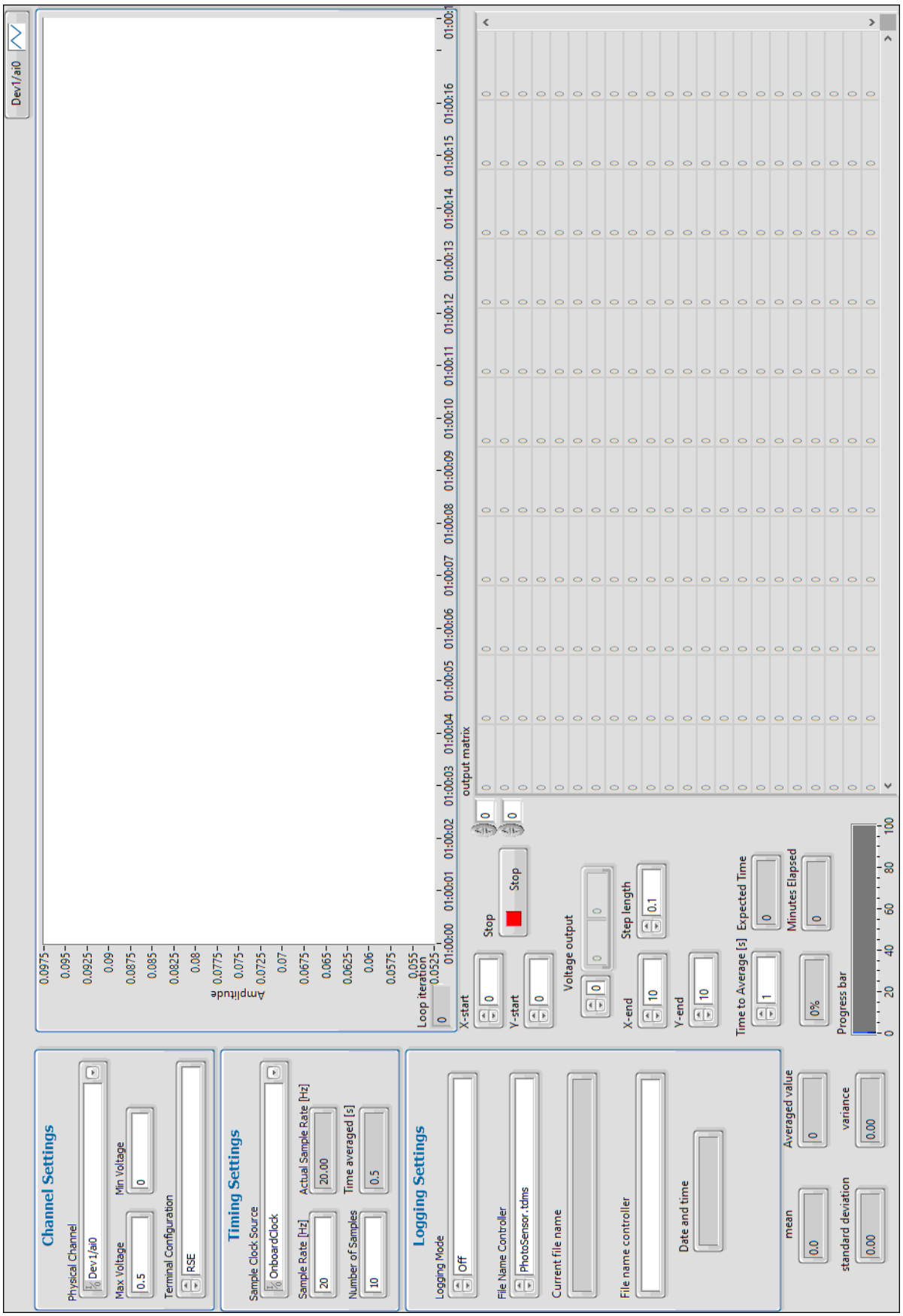

Figure B.3: The front panel of the Confocal Imaging LabVIEW code.

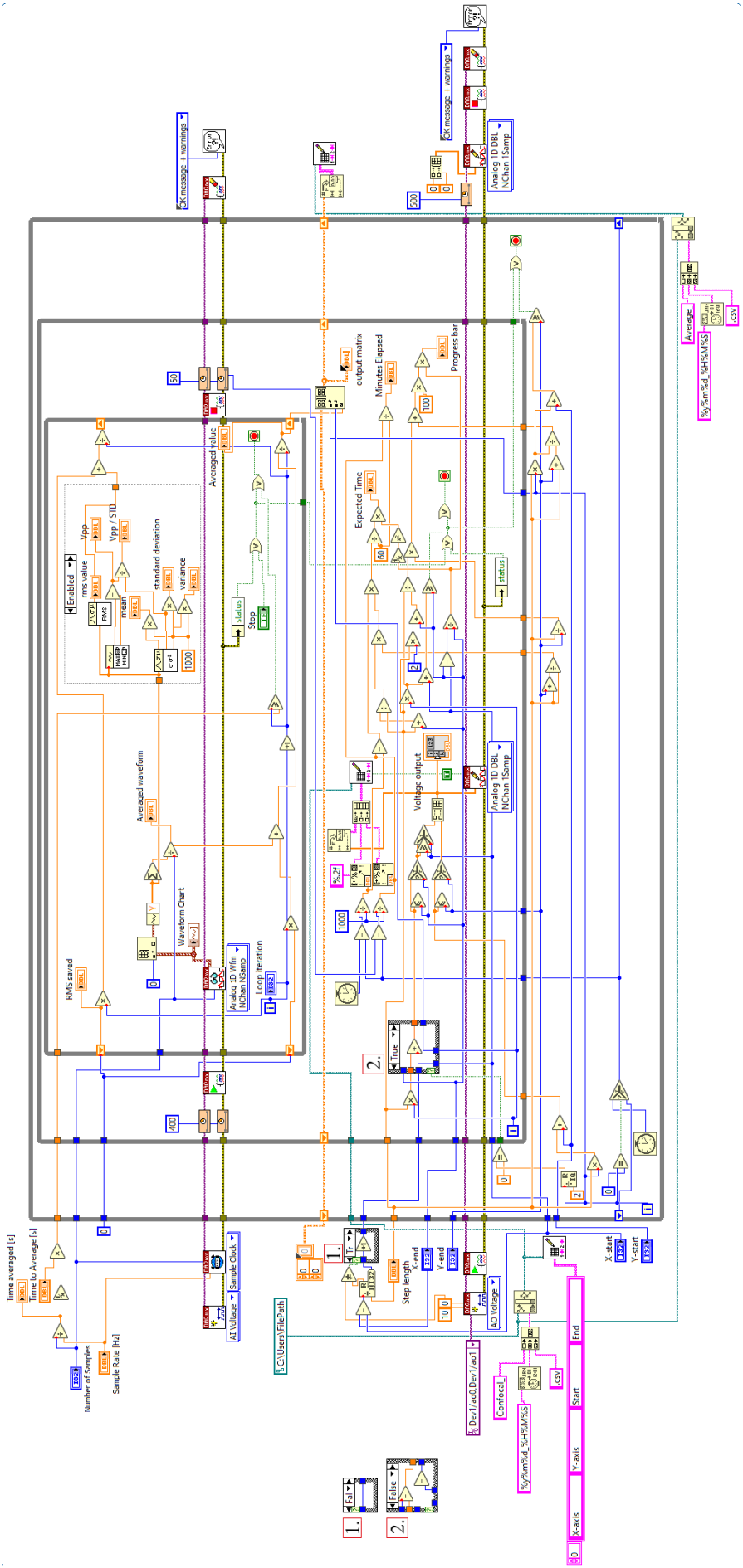

Figure B.4: The back panel of the Confocal Imaging LabVIEW code.

Bibliography

[1] I. R. McFadyen, E. E. Fullerton, and M. J. Carey. State-of-the-art magnetic hard disk drives. *MRS Bulletin*, 31(5), 2006. 1

[2] E. Grochowski and R. D. Halem. Technological impact of magnetic hard disk drives on storage systems. *IBM Systems Journal*, 42(2), 2003. 1

[3] Pragasen Pillay and Ramu Krishnan. Modeling, Simulation, and Analysis of Permanent-Magnet Motor Drives,Part I: The Permanent-Magnet Synchronous Motor Drive. *IEEE Transactions on Industry Applications*, 25(2), 1989. 1

[4] Wenping Cao, Barrie C. Mecrow, Glynn J. Atkinson, John W. Bennett, and David J. Atkinson. Overview of electric motor technologies used for more electric aircraft (MEA). *IEEE Transactions on Industrial Electronics*, 59(9), 2012. 1

[5] S. Ogawa, T. M. Lee, A. R. Kay, and D. W. Tank. Brain magnetic resonance imaging with contrast dependent on blood oxygenation. *Proceedings of the National Academy of Sciences of the United States of America*, 87(24), 1990. 1

[6] M. N. Baibich, J. M. Broto, A. Fert, F. Nguyen Van Dau, F. Petroff, P. Eitenne, G. Creuzet, A. Friederich, and J. Chazelas. Giant magnetoresistance of (001)Fe/(001)Cr magnetic superlattices. *Physical Review Letters*, 61(21):2472–2475, 1988. 1

[7] S. A. Wolf, D. D. Awschalom, R. A. Buhrman, J. M. Daughton, S. Von Molnár, M. L. Roukes, A. Y. Chtchelkanova, and D. M. Treger. Spintronics: A spin-based electronics vision for the future, nov 2001. 1

[8] L. Rondin, J. P. Tetienne, T. Hingant, J. F. Roch, P. Maletinsky, and V. Jacques. Magnetometry with nitrogen-vacancy defects in diamond, 2014. 1, 8, 10, 11

[9] Edlyn V. Levine, Matthew J. Turner, Pauli Kehayias, Connor A. Hart, Nicholas Langellier, Raisa Trubko, David R. Glenn, Roger R. Fu, and Ronald L. Walsworth. Principles and techniques of the quantum diamond microscope, 2019. 1, 2, 3, 11, 61

[10] U. Hartmann. Magnetic force microscopy. *Annual Review of Materials Science*, 29:53–87, 1999. 1

[11] L. E. Fong, J. R. Holzer, K. K. McBride, E. A. Lima, F. Baudenbacher, and M. Radparvar. High-resolution room-temperature sample scanning superconducting quantum interference device microscope configurable for geological and biomagnetic applications. *Review of Scientific Instruments*, 76(5), 2005. 1

[12] D. A. Allwood, Gang Xiong, M. D. Cooke, and R. P. Cowburn. Magneto-optical Kerr effect analysis of magnetic nanostructures. *Journal of Physics D: Applied Physics*, 36(18), 2003. 1

[13] J. J. Davies. Optically-detected magnetic resonance and its applications. *Contemporary Physics*, 17(3), 1976. 2

[14] Mayeul Chipaux, Alexandre Tallaire, Jocelyn Achard, Sébastien Pezzagna, Jan Meijer, Vincent Jacques, Jean François Roch, and Thierry Debuisschert. Magnetic imaging with an ensemble of nitrogen vacancy-centers in diamond. *European Physical Journal D*, 69(7), 2015. 3, 12

[15] Jean Philippe Tetienne, Nikolai Dontschuk, David A. Broadway, Alastair Stacey, David A. Simpson, and Lloyd C.L. Hollenberg. Quantum imaging of current flow in graphene. *Science Advances*, 3(4), 2017. 3

[16] D. Le Sage, K. Arai, D. R. Glenn, S. J. Devience, L. M. Pham, L. Rahn-Lee, M. D. Lukin, A. Yacoby, A. Komeili, and R. L. Walsworth. Optical magnetic imaging of living cells. *Nature*, 496(7446), 2013. 3

[17] Stefan W. Hell and Jan Wichmann. Breaking the diffraction resolution limit by stimulated emission: stimulated-emission-depletion fluorescence microscopy. *Optics Letters*, 19(11), 1994. 3

[18] S. W. Hell and M. Kroug. Ground-state-depletion fluorscence microscopy: A concept for breaking the diffraction resolution limit. *Applied Physics B Lasers and Optics*, 60(5), 1995. 3

[19] Michael J Rust, Mark Bates, and Xiaowei Zhuang. Sub-diffraction-limit imaging by stochastic optical reconstruction microscopy (STORM). *Nature Methods*, 3(10):793–795, aug 2006. 4, 14

[20] Matthias Pfender, Nabeel Aslam, Gerald Waldherr, Philipp Neumann, Jörg Wrachtrup, and Juan Pablo Paz. Single-spin stochastic optical reconstruction microscopy. *Proceedings of the National Academy of Sciences of the United States of America*, 111(41), 2014. 4, 9, 12, 13, 14, 21, 32, 34, 59, 63

[21] F. P. Bundy, H. T. Hall, H. M. Strong, and R. H. Wentorf. Man-Made diamonds. *Nature*, 176(4471):51–55, 1955. 7

[22] H. Sumiya, N. Toda, and S. Satoh. Mechanical properties of synthetic type IIa diamond crystal. *Diamond and Related Materials*, 6(12):1841–1846, dec 1997. 7

[23] Sergio Ferro. Synthesis of diamond, oct 2002. 7

[24] William G Eversole. Synthesis of diamond, April 17 1962. US Patent 3,030,187. 7

[25] N. B. Manson, J. P. Harrison, and M. J. Sellars. Nitrogen-vacancy center in diamond: Model of the electronic structure and associated dynamics. *Physical Review B - Condensed Matter and Materials Physics*, 74(10):104303, sep 2006. 8

[26] Philipp Reineck, Leevan Fremiot Trindade, Jan Havlik, Jan Stursa, Ashleigh Heffernan, Aaron Elbourne, Antony Orth, Marco Capelli, Petr Cigler, David A. Simpson, and Brant C. Gibson. Not All Fluorescent Nanodiamonds Are Created Equal: A Comparative Study. *Particle & Particle Systems Characterization*, 36(3):1900009, mar 2019. 8, 9, 12, 30, 33

[27] M. F. Davies, G.; Hamer. Optical studies of the 1.945 eV vibronic band in diamond. *Proceedings of the Royal Society of London. A. Mathematical and Physical Sciences*, 348(1653):285–298, feb 1976. 8

[28] A. M. Edmonds, U. F.S. D'Haenens-Johansson, R. J. Cruddace, M. E. Newton, K.-M. M.C. Fu, C. Santori, R. G. Beausoleil, D. J. Twitchen, and M. L. Markham. Production of oriented nitrogen-vacancy color centers in synthetic diamond. *Physical Review B - Condensed Matter and Materials Physics*, 86(3):035201, jul 2012. 9, 25

[29] J R Maze, A Gali, E Togan, Y Chu, A Trifonov, E Kaxiras, and M D Lukin. Properties of nitrogen-vacancy centers in diamond: The group theoretic approach. *New Journal of Physics*, 13(2):025025, feb 2011. 10

[30] M W Doherty, N B Manson, P Delaney, and L. C.L. Hollenberg. The negatively charged nitrogen-vacancy centre in diamond: The electronic solution. *New Journal of Physics*, 13(2):025019, feb 2011. 10

[31] JE Lennard-Jones. The determination of molecular orbitals. *Proceedings of the Royal Society of London. Series A. Mathematical and Physical Sciences*, 198(1052):1–13, jul 1949. 10

[32] Idan Meirzada, Sigal A. Wolf, and Nir Bar-Gill. Finding the nitrogen-vacancy singlet manifold energy level using charge conversion pulse sequences. *arXiv preprint arXiv*, nov 2020. 11

[33] N Aslam, G Waldherr, P. Neumann, F. Jelezko, and J. Wrachtrup. Photo-induced ionization dynamics of the nitrogen vacancy defect in diamond investigated by single-shot charge state detection. *New Journal of Physics*, 15, 2013. 12

[34] Beatrice Rodiek, Marco Lopez, Helmuth Hofer, Geiland Porrovecchio, Marek Smid, Xiao-Liu Chu, Stephan Gotzinger, Vahid Sandoghdar, Sarah Lindner, Christoph Becher, and Stefan Kuck. Experimental realization of an absolute single-photon source based on a single nitrogen vacancy center in a nanodiamond. *Optica*, 4(1):71, 2017. 13, 49, 59

[35] Vasilis Ntziachristos. Going deeper than microscopy: The optical imaging frontier in biology, 2010. 15

[36] Yang Leng. *Materials characterization: Introduction to microscopic and spectroscopic methods: Second edition*. wiley, aug 2013. 15, 16

[37] Hugh D Young and Roger A Freedman. *University Physics with Modern Physics 14th Edition*, volume 3. Pearson Education Limited, 2016. 15, 17, 18, 19, 20, 24

[38] Peter O. Bayguinov, Dennis M. Oakley, Chien-Cheng Shih, Daniel J. Geanon, Matthew S. Joens, and James A. J. Fitzpatrick. Modern Laser Scanning Confocal Microscopy. *Current Protocols in Cytometry*, 85(1):e39, jul 2018. 15, 22, 23

[39] Chunhao Liang, Gaofeng Wu, Fei Wang, Wei Li, Yangjian Cai, and Sergey A. Ponomarenko. Overcoming the classical Rayleigh diffraction limit by controlling two-point correlations of partially coherent light sources. *Optics Express*, 25(23):28352, nov 2017. 16

[40] Rayleigh. XXXI. Investigations in optics, with special reference to the spectroscope. *The London, Edinburgh, and Dublin Philosophical Magazine and Journal of Science*, 8(49):261–274, oct 1879. 16

[41] Bonnie O. Leung and Keng C. Chou. Review of super - Resolution fluorescence microscopy for biology, sep 2011. 16, 17

[42] T. Wilson. Resolution and optical sectioning in the confocal microscope, nov 2011. 16, 22

[43] M Minsky. Microscopy Apparatus. *US Patent 3013467*, 3013467(3013467):5, 1957. 16

[44] Jeff W Lichtman and José Angel Conchello. Fluorescence microscopy, nov 2005. 16, 17

[45] H. NYQUIST. Certain Topics in Telegraph Transmission Theory. *Transactions of the American Institute of Electrical Engineers*, 47(2):617–644, 1928. 16

[46] José Angel Conchello and Jeff W Lichtman. Optical sectioning microscopy, nov 2005. 16, 22

[47] E Abbe Archiv für mikroskopische Anatomie and Undefined 1873. Beiträge zur Theorie des Mikroskops und der mikroskopischen Wahrnehmung: II. Die dioptrischen Bedingungen der Leistung des Mikroskops. *Archiv für mikroskopische Anatomie*, 9(1):418–440, 1873. 17

[48] Richard W Cole, Tushare Jinadasa, and Claire M Brown. Measuring and interpreting point spread functions to determine confocal microscope resolution and ensure quality control. *Nature Protocols 2011 6:12*, 6(12):1929–1941, nov 2011. 17, 22, 26

[49] Takao Itoh. Fluorescence and phosphorescence from higher excited states of organic molecules, aug 2012. 17

[50] M Planck. On the Law of Distribution of Energy in the Normal Spectrum. *Annalen der Physik*, 4:533, 1901. 17

[51] A. H. Firester. The thin lens equation for optical parametric image conversion. *Optoelectronics*, 1(3):138–142, aug 1969. 18

[52] Dave Litwiller. Ccd vs. cmos. *Photonics spectra*, 35(1):154–158, 2001. 19

[53] Eric R. Fossum. CMOS image sensors: electronic camera-on-a-chip. *IEEE Transactions on Electron Devices*, 44(10):1689–1698, 1997. 19

[54] Rachel A. Yotter and Denise Michelle Wilson. A review of photodetectors for sensing light-emitting reporters in biological systems, jun 2003. 19, 20

[55] V. K. Zworykin, G. A. Morton, and L. Malter. Technical papers: The secondary emission multiplier—a new electronic device. *Proceedings of the Institute of Radio Engineers*, 24(3):351–375, 1936. 19

[56] Shu Xia Tao, Hong Wah Chan, and Harry Van Der Graaf. Secondary electron emission materials for transmission dynodes in novel photomultipliers: A review, dec 2016. 20

[57] T. H. Maiman. Stimulated optical radiation in Ruby. *Nature*, 187(4736):493–494, 1960. 20

[58] Willis E. Lamb. Theory of an optical maser. *Physical Review*, 134(6A), 1964. 20

[59] H. M. Gibbs, S. L. McCall, and T. N.C. Venkatesan. Differential gain and bistability using a sodium-filled fabry-perot interferometer. *Physical Review Letters*, 36(19):1135–1138, 1976. 20

[60] A. L. Schawlow and C. H. Townes. Infrared and optical masers. *Physical Review*, 112(6):1940–1949, dec 1958. 20

[61] G. D. Boyd and J. P. Gordon. Confocal Multimode Resonator for Millimeter Through Optical Wavelength Masers. *Bell System Technical Journal*, 40(2):489–508, 1961. 21

[62] L. D. Dickson. Characteristics of a Propagating Gaussian Beam. *Applied Optics*, 9(8):1854, 1970. 21

[63] P. Belland and J. P. Crenn. Changes in the characteristics of a Gaussian beam weakly diffracted by a circular aperture. *Applied Optics*, 21(3):522, feb 1982. 21

[64] ISO 11145:2018. Optics and photonics – Lasers and laser-related equipment – Vocabulary and symbols. https://www.iso.org/obp/ui/#iso:std:iso:11145:ed-5:v1:en, 2018. Accessed: 2021-07-27. 22

[65] George Biddell Airy. On the Diffraction of an Object-glass with a Circular Aperture. *Transactions of the Cambridge Philosophical Society*, 5:283–291, 1834. 22

[66] Harold Osterberg and Luther W. Smith. Defocusing images to increase resolution. *Science*, 134(3486):1193–1196, 1961. 22

[67] Kenneth N. Berk Jay L. Devore. *Modern Mathematical Statistics with Applications - 2nd Edition*, volume 64. Springer-Verlag New York Inc., 2012. 23, 24

[68] RHODAMINE 640 PERCHOLRATE. https://www.photonicsolutions.co.uk/upfiles/Rhodamine640Perchlorate.pdf, 2006. Accessed: 2021-08-01. 26, 27, 62

[69] Chanelle C. Jumper, Paul C. Arpin, Daniel B. Turner, Scott D. McClure, Shahnawaz Rafiq, Jacob C. Dean, Jeffrey A. Cina, Philip A. Kovac, Tihana Mirkovic, and Gregory D. Scholes. Broad-Band Pump-Probe Spectroscopy Quantifies Ultrafast Solvation Dynamics of Proteins and Molecules. *Journal of Physical Chemistry Letters*, 7(22):4722–4731, nov 2016. 26, 27

[70] Verena Mackowiak, Jens Peupelmann, Yi Ma, and Anthony Gorges. *NEP-Noise Equivalent Power*. 31

[71] Manuel A. Diaz. Fit 1D and 2D gaussian to noisy data. https://www.mathworks.com/matlabcentral/fileexchange/55033-fit-1d-and-2d-gaussian-to-noisy-data, 2016. MATLAB Central File Exchange. Retrieved July 14, 2021. 37, 38, 65

[72] Chance Elliott, Vipin Vijayakumar, Wesley Zink, and Richard Hansen. National Instruments LabVIEW: A Programming Environment for Laboratory Automation and Measurement. *Journal of Laboratory Automation*, 12(1):17–24, aug 2007. 38

[73] Sindy K.Y. Tang, Claudiu A. Stan, and George M. Whitesides. Dynamically reconfigurable liquid-core liquid-cladding lens in a microfluidic channel. *Lab on a Chip*, 8(3):395–401, feb 2008. 61